Universitat de Girona

# SIGNAL PROCESSING OF MICROSTRUCTURE PROFILES: INTEGRATING TURBULENT SPATIAL SCALES IN AQUATIC ECOLOGICAL MODELING

**Jaume PIERA FERNÁNDEZ**

**ISBN: 84-689-0620-4**
**Dipòsit legal: Gi.1391-2004**
http://hdl.handle.net/10803/7650

Universitat de Girona

# Signal processing of microstructure profiles: Integrating turbulent spatial scales in aquatic ecological modeling

Jaume Piera

Girona, December 2001

Als meus pares

i a l'Arantxa

*In digging for potatoes,*
*it is not so important that you dig like hell*
*as you dig where the potatoes are!*

*CARL HARTLEY*
President of Hartley's Potato Chips

La doctora Elena Roget Armengol, professora titular del Departament de Física de la Universitat de Girona, i el doctor Jordi Catalan Aguilà, professor investigador del Centre d'Estudis Avançats de Blanes (CSIC)

CERTIFIQUEN que la tesi doctoral que aquí es presenta sota el títol de *Signal processing of microstructure profiles: Integrating turbulent spatial scales in aqutical ecological modeling* ha estat realitzada, sota la seva direcció, per en Jaume Piera Fernández.

Girona, 30 de novembre de 2001.

Signat: Elena Roget Armengol

Signat: Jordi Catalan Aguilà

# Aknowledgments (Agraïments)

En el llarg camí realitzat per dur a terme aquest treball de recerca he pogut gaudir de l'ajut, directe o indirecte, d'una gran quantitat de persones a les quals voldria agrair el seu suport.

Els primers, evidentment, l'Elena i el Jordi. Gràcies a la seva inquietud en aquest camp, he tingut l'oportunitat d'endinsar-me en aquest món tan "turbulent".

Als companys del grup de Física Ambiental Teresa, Xavi, Jordi, Marianna, Toni, voldria agrair el seu ajut i molt especialment al Quim, no tan sols pel seu suport, sinó també per la seva amistat. També vull agrair a l'Anna i a en Xicu tot l'ajut que m'han proporcionat.

He tingut la sort de conviure, dins el departament d'Ecologia, amb un munt de persones ben especials. Als membres del grup de recerca d'alta muntanya (i companys de "cubícul" ) Fede, Marc, Sergi, Teresa, Marisol, Lluís, Guillermo i Cristina, voldria agrair-los el seu ajut i la paciència d'aguantar les cabòries de l'"ingenieru".

El dia a dia amb la resta de persones vinculades al departament d'Ecologia m'ha proporcionat moments per gaudir d'un munt de petites coses, que m'han donat els ànims per poder tirar endavant aquest projecte. Bernat, Miquel Àngel, Núria(es), Salva, Pere, Fiona, Xavi, Marta(es), Juan Carlos, Montse(s), Olga, Mireia, Carol, Rosa, Chechu, Quique, David, Jose, Marc, Guillem, Biel, Ester, Andrea, Rafa, Susanna ... el proper sopar "temàtic" el fem a casa, d'acord?

Fora de l'àmbit "professional" (les " " que no faltin , eh Xavi ?) també hi ha hagut moltes persones a les que voldria esmentar per tot el que hem passat plegats: l'Enric, la Mònica, la Martina i el Ferran (¡tot just vingut!), en Toni, l'Eva i el Jofre, el Marcos, la Blanca, l'Andrés, l'Alicia, l'Oscar i la Clara, la Mari, la Núria, l'Eva, la Noemi, l'Anna, i també l'Irma, el Marc, el Xavi, el Marcos, la Mònica, la Maria ... ¡moltes gràcies a tots i a totes!

També voldria recordar la família de l'Arantxa per tot el que han fet per nosaltres. Pedro , Maria José, Pau (gràcies pels truquillos de LaTeX), Raquel Amaya, Santi (¡y como no! a los abuelos Pedro y Pilar)

I am very thankful to Jörg Imberger and the people from the Centre of Water Research, who gave me the initial information (the most important) to set up the first version of microstructure data analysis software. I was able to analyze the microstructure data from Lake Redo thanks also to Jörg Imberger, who provided the field measurements carried out some years ago.

I would like to thank Johnny Wüest for his valuable suggestions. Chapter 2 has improved from his critical reading and comments.

Dieter Imboden and Roland Stull provided me the first information about non-local mixing models, which was essential for the development of chapter 4.

There is a special mention for those people related to open source software. For sure I would have not finished my work without the help of people that believes that shared knowledge is the best way to improve things.

Per acabar, voldria recordar a la gent més propera. Els meus germans: l'Alvar, la Mercè, la Gemma, la Cristina i la Laia i la resta de les seves famílies: la Pati, la Júlia i l'Helena, l'Òscar, la Gisela i l'Òscar (menut), el Dani i el Sergi, i la Carmen.

Els meus pares Josep i Mapy són els responsables directes de que hagi pogut començar aquesta llarga travessa. Per tot el que m'han donat, es mereixen la més especial de les dedicatòries.

Finalment, vull expressar (si en sóc capaç) tot el que ha suposat per mi la persona amb la què he recorregut aquest camí: l'Arantxa. A ella li ha tocat patir els moments més durs i, possiblement, no ha pogut gaudir dels moments més dolços. Si algú es mereix el meu agraïment és ella.

Sortosament, de travesses encara ens en queden moltes per fer. De fet, tot just acabem de començar.

Barcelona, 22 de novembre de 2001

# Contents

# Introduction

## Motivation

Hydrodynamics plays a primary role in aquatic ecosystems, affecting processes at a wide range of temporal and spatial scales. At small scales, turbulence affects the dynamics of aquatic ecosystems by enhancing the transport of nutrients, organisms, heat, sediments, and pollutants within the water column. The establishment of any biological-physical interaction requires the understanding of the environmental changes derived from the transport mechanisms and the response of the organisms in front of these changes. The main aim of dynamic biological oceanography or limnology is to link the environmental changes derived from the transport mechanisms and the response of the organisms in front of these changes on the appropriate spatial and temporal scales.

In the last years, resources in small-scale hydrodynamics research have significantly increased. The development of new instruments and the revolutionary improvements of computer hardware and software have provided the capability to obtain a high amount of data with spatial and temporal resolution that was unimaginable two decades ago. Nowadays it is possible with a personal computer developing numerical modeling and digital processing that, only few years ago, required equipment only available at selected universities and research institutes.

Due to the improvement of instrumental and methodological facilities, the interest of small-scale interactions in the aquatic ecosystems has increased in the last years. This interest has been reflected on the related scientific literature and, as an example, we can mention some of the works that present the effects of turbulence over different aspect of biological processes: the vertical distribution of organisms (Haury *et al.*, 1990), the changes on the prey-pedator encounter rate (Davis *et al.*, 1991), the influence on photosynthetic productivity (Cullen and Lewis, 1988; Ferris and Christian, 1991), or the formation of organic aggregates changing significantly the sedimentation rate of organic material (Mac Intyre *et al.*, 1995). All this type of interac-

tions induces to consider the small-scale hydrodynamics not only one of the main factors for the plankton succession (Margalef, 1983), but also for their evolution (Catalan, 1999).

However, the current knowledge of the physical-biological interactions at small-scale is still in a very early stage of development. To fulfil this lack of knowledge, multidisciplinary approaches are necessary. With this in mind, this thesis was developed in collaboration between the department of Physics at the University of Girona and the department of Ecology at the University of Barcelona. The main objective was the development of a new method for the description of environmental turbulent flows, which were more suitable for investigating and understanding biological-physical interactions at small-scale.

# Measurement and processing techniques

The methodology finally proposed is based on the signal processing of measurements obtained from a very specialized instrumentation, the microstructure profilers. These instruments measure vertical profiles of relevant physical magnitudes with a very high resolution, down to the scale of some millimeters.

Microstructure profilers have been used extensively in physical microscale characterization. Although the current knowledge of the environmental small-scale hydrodynamics is far from complete, there is a general agreement that turbulence is an intermittent phenomena that occurs in turbulent patches. The intermittence of the turbulence and the mismatch in sampling resolution between physical and biological measurements represents the two main difficulties for relating turbulent mixing to different biological processes. There are attempts to measure biological magnitudes, and processes at the same resolution that physical measurements (Oldham, 1993; Desiderio *et al.*, 1993; Wesson *et al.*, 1998). An alternative approach is the temporal upscaling of the physical microscale properties and its comparison with biological measurements. As organisms integrate the environmental factors, the comparison of biological measurements and the "integrated" environmental turbulence can be carried out with confidence of being representative at longer time scales. For this reason, the integration of the microscale measurements in synoptic parameters can be particularly useful in the characterization of physical-biological interactions at small scales.

# Objectives

The main objective of this thesis was the integration of microstructure information in synoptic descriptors of turbulence, that reflects the mixing processes. Turbulent patches are intermittent in space and time, but they represent the dominant process for mixing. In this work, the properties of turbulent patches were considered the potential input for integrating the physical microscale measurements. The development of a method for integrating the properties of the turbulent patches required solving three main questions: *a)* how can we detect the turbulent patches from the microstructure measurements?; *b)* which are the most relevant properties of the turbulent patches?; and *c)* once an interval of time has been selected, what kind of synoptic parameters could better reflect the occurrence and properties of the turbulent patches?

The answers to these questions were the final specific objectives of this thesis.

# Outline

The results obtained in this work are presented in the three main chapters, but two more chapters have been added. First, an introductory chapter for those who are less familiar with the particular field of microstruture measurements and, finally, a chapter where conclusions are discussed in the framework of their potential application to biological questions.

Chapter 1 (*Instrumental and data handling*) introduces the basic concepts of measurement techniques in two different parts. In the first part, there is an exposition of the instrumental characteristics of two different microstructure profilers, which provided the data for the developments made in following chapters. In the second part, the methodology for computing standard parameters from microstructure measurements is introduced, which are not necessarily familiar to anyone involved in turbulence and physical limnology.

In chapter 2 (*Turbulent patch identification*) a new method for turbulent patch identification is presented, which can be applied in a wide range of density gradients. A general shortcoming of the methods for patch identification, which are revised at the beginning of the chapter, is their failure in identifying turbulent patches at low-density gradients. However, biological-physical processes should be characterized in the widest turbulent environmental range as possible, because many biological processes of interest occur at low-density gradients. The new method presented highly reduces that limitation.

In chapter 3 (*Length scale analysis of turbulent patches*) a new method for describing turbulent patch dynamics is introduced. The method is based on length scale analysis, which is a common procedure for computing relevant properties of turbulent patches. The interpretation of the results obtained with this type of analysis have generated some controversy and nowadays it is one of the main debatable issues in environmental turbulence. In a geophysical context, understanding the time evolution of turbulence is a crucial prerequisite for the proper interpretation of the length scale measurements. In this chapter the response to wind burst is presented as a new geophysical process for observing the evolution of the turbulence. Field measurements obtained during a wind burst were used for a length scale analysis of the turbulent patches, which eventually resulted in the proposal of the new hydrodynamic diagram. This diagram is constructed from topological properties of the turbulent patches, which in the analysis turned out to be the most relevant properties for turbulent patch characterization.

In chapter 4 (*Integrating turbulent characterization in mixing ecological models*), a new method of turbulent mixing parameterization, based on data obtained from microstructe profiles, is presented. A common approach for including turbulent mixing effects on ecological processes is through numerical modeling. In general, numerical models are not able to simulate directly the effects of turbulence due to the limits on temporal and spatial resolution, and mixing must be described in terms of empirical or modeled parameters.

In this study a new parameterization is proposed, based on the topological properties of the turbulent patches. The proposed methodology allows estimating different synoptic parameters, which can be used not only for numerical modeling but also as descriptors of the turbulence in ecological analyses.

In chapter 5 (*Synthesis and outlook*) the main results of this study are summarized and discussed in terms of their relevance for biological applications. Some guidelines for future developments and applications are presented.

# Chapter 1

# Instrumental data handling

In this introductory chapter the main instrumental characteristics of two different microstructure profilers used to obtain field data are presented.

The microstructure profilers are usually equipped with sensors to measure the stratification (temperature, electrical conductivity) as well as the velocity fluctuations (current shear) in the microstructure scale range. Modern microstructure measuring systems are equipped with microstructure sensors as well as high precision CTD (Conductivity, Temperature, Depth) sensors. This enables the simultaneous recording of high-resolution microstructure profiles and high precision profiles of standard oceanographic parameters at lower spatial resolution. Some specialized profilers allow measuring other parameter of interest as oxygen concentration (Oldham, 1993) or fluorescence (Cowles *et al.* 1993).

Microstructure investigation requires an undisturbed measuring procedure of the profiling instrument. Effects caused by cable tension (vibrations) and the boat movement are excluded by buoyancy driven free sinking or rising measurements.

Two different microstructure probes have been used to obtain the field data analyzed in this thesis. The first probe was the MP profiler developed by the Centre for Water Research (CWR) which at present is commercialized, with an improved data acquisition system (Carter and Imberger, 1986), by Precision Measurement Engineering as the Self Contained Autonomous MicroProfiler (SCAMP). The second probe was the MSS profiler, developed by ISW Wassermesstechnik and Sea&Sun Technology.

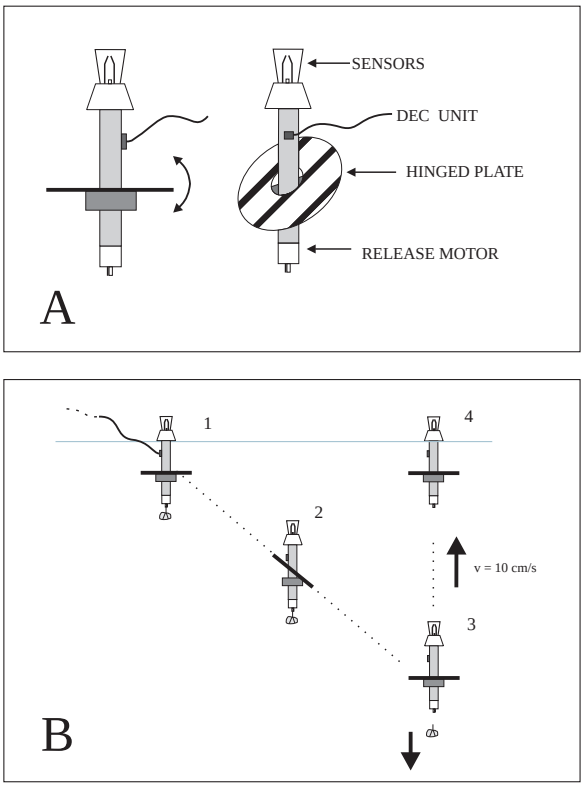


Figure 1.1: *(A) Schematics of the MP profiler. (B) Different steps of measuring a profile in upward mode. (B1) An extra weight forces the profiler to sink sideways (B2) until it reaches the bottom or a pre-determined depth. When the user activates the release motor and drops the expendable weight (B3), the MS profiler floats vertically upward (B4) until the sensors pass through the surface.*

## 1.1 MP profiler

The MP was designed to profile inland and coastal waters, obtaining microstructure profiles up to 100 meters depth.

In the present work the MP has been used in upward mode, sampling undisturbed water up through the surface. Figure 1.1 B shows a schematic of the measurement procedure in several steps.

The first step for upraising measurements is adding an extra weight to the profiler that makes the profiler denser than the water. The extra weight, and the hinged plate, forces the instrument to sink sideways at an angle of approximately 45 degrees until it reaches the bottom or a pre-determined

| **Fast Temperature Sensor** | |
|---|---|
| Model | FP07 (Thermometrics) |
| Resistance at 25 $^o$C | 100 $K\Omega \pm 20$ % or 20 $K\Omega \pm 20$ % |
| Time response | approx. 7 ms air/water plunge |
| Drift | 0.100 $^o$C/month (maximum) |
| **Fast Conductivity Sensor** | |
| Spatial resolution | approximately -3db at 4 $cycles\,cm^{-1}$ |
| | approximately 1 mm diameter sphere |
| Cell-cell variation | $\pm$ 20 % |
| Drift | $\pm$ 1 % of the reading over 8 hours |
| Cell constant | to be determined |
| **Pressure (depth) Sensor** | |
| Model | Keller PSI PAA-10 |
| Range | 50 to 100 meters full scale |
| Accuracy | $\pm$ 0.5 % full scale |
| Repeatability | $\pm$ 0.25 % full scale |
| Stability | $\pm$ 0.25 % / 6 months |

Table 1.1: Specifications of the different sensors provided by Precision Measurement Engineering

depth. Upon reaching this point, the user activates the release motor and drops the expendable weight. The MS profiler then floats vertically upward at 10 $cm\,s^{-1}$, obtaining measurements of the different sensors at 100 Hz sampling rate, which yields a resolution of 1 $sample\,mm^{-1}$ for the different measurements. Samples are transmitted via a conducting data cable to a deck host computer. Sampling continues until the sensors pass through the surface. When the profile is complete, the MP profiler is recovered using the data cable.

Alternatively, the MP can be used in downward mode, sampling undisturbed water beginning somewhat below the surface and continuing all the way to the bottom. These two modes of travel enable the MP to measure both surface mixing and bottom boundary layer mixing.

### 1.1.1 Sensor features

The MP microprofiler measures temperature, conductivity and depth at high spatial resolution.

Table 1.1 summarizes the main features of the different sensors.

### Temperature

The temperature microstructure sensor is based on the glass isolated miniaturized thermistor FP07 (Thermometrics, USA). The thermistor bead has a diameter of 75 $\mu m$, encapsulated in a glass tip with a diameter of 250 $\mu m$. The small dimensions of the bead, in the submillimeter scale range, yields in a fast response of temperature changes, with a time constants in water of some ms. The nominal response time (63.2 % of the total difference between initial and final body temperature) of the FP07 thermistor is 7 ms (Thermometrics, 1988).

The high thermal sensitivity of the microbead thermistors enables a temperature resolution of less than $10^{-5}$ $K$ (Gregg *et al.*, 1978). Although this type of sensors have a high sensitivity to mechanical stress, with a high risk of breaking the fine glass tip, the thermal and electrical properties make microbead thermistors the most suitable sensors for thermal microstructure measurements.

### Conductivity

The conductivity sensor was designed by Precision Measurement Engineering (PME) following Head (1983). The sensor was developed for making very rapid, high resolution measurements of the electrical conductivity of water.

An schematics of the tip of the sensor is shown in the fig 1.2. This sensor consists of 4 electrodes (platinum spheres) supported by fused glass. Each electrode is electroplated with an amorphous platinum coating.

The electronic circuit makes a 4 terminal measurement of the conductance of the water by supplying an A.C. current between the inner electrodes of the sensor and measuring the A.C. voltage that develops across the outer electrodes. The ratio of this current to voltage is computed by the circuit and a representative voltage supplied at the circuit output. When used in this way, the output voltage corresponds to a weighted volume average of the conductivity of the water in the vicinity of the sensor electrodes.

The sensor will respond to conductivity features that are large compared to the separation between the inner electrodes and is increasingly less sensitive to increasingly smaller features. The spatial averaging volume of the sensor can be estimated to be a sphere of radius 1/2 mm centered between the inner electrodes. This is only an approximation, however, of the actual sensitivity described by a complicated weighting function applied to all points around the sensor. The spatial resolution can also be described in wave number space: the sensor attenuates the measurement 3 db at approximately 4 cycles/cm (PME, 2001).

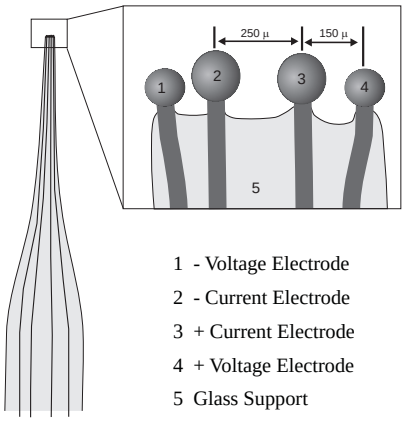


Figure 1.2: *Detail of the microstructure conductimeter. (Adapted from PME, 2001.)*

### 1.1.2 Data acquisition and processing

Initially, the MP profiler was provided only with a data acquisition software. The data processing software was adapted from a source code developed at the Centre of Water Research (CWR), University of Western Australia. The CWR programs were written in Fortran77 language to be compiled in Unix operating system. The first step was the code adaptation to Linux operating system. New functions were developed in C language but the final applications of this thesis were developed with the Matlab software package (V 5.3 © The MathWorks Inc).

## 1.2 MSS profiler

The MSS Profiler is an instrument for simultaneous microstructure and precision measurements of physical parameters in marine (coastal and open waters) and inland waters. The depth limit for this instrument is also 100 m. The profiler can be used for vertical sinking as well as for uprising measurements. In sinking mode the profiler is manually handled while upraising measurements require a remote controlled underwater winch, which it has not available. For this reason, in the present work only sinking measurements have been done. The basic system configuration is shown in fig. 1.3.

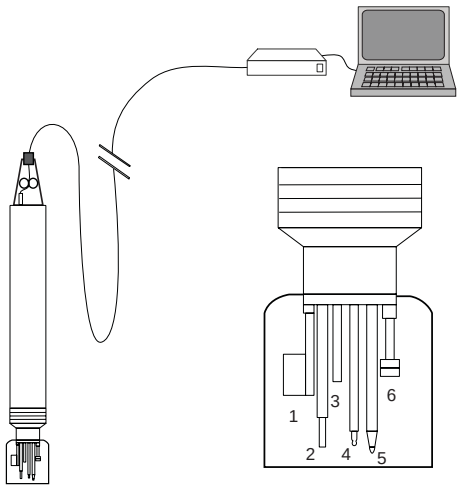


Figure 1.3: *Schematics of the MSS profiler. The detailed figure shows the different type of sensors. (1) Precision conductimeter. (2) Precision temperature sensor. (3) Pseudo-shear (internal vibration) sensor. (4) Fast response temperature. (5) Shear sensor. (6) Pressure sensor. (Adapted from Prandke and Stips, 1966.)*

### 1.2.1 Sensor features

#### Temperature

The temperature microstructure sensor is based on the glass isolated miniaturized thermistor FP07, as in the case of MP profiler. This sensor has become a standard of microstructure temperature masurements because, due to its particular features, it fits the requirements for the fast temperature measurements at high spatial resolution.

#### Conductivity

A microstructure conductivity sensor for the MSS profiler was not available, and the conductivity data was measured with the high precision conductivity sensor. This low response of the high precision conductivity sensor was not very restrictive as all the field measurements were taken in fresh-water, were the effects of changes on salinity over stratification were relativelly small and could be neglected.

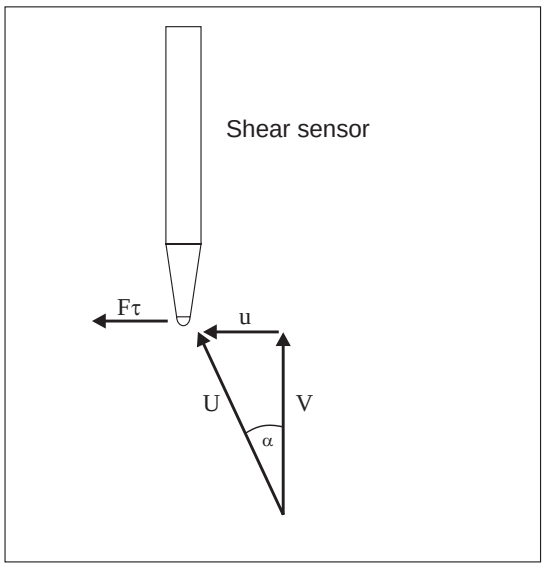


Figure 1.4: *Scheme of the shear sensor operation. (Adapated from Prandke and Stips, 1996)*

### Shear

For measurements of oceanic velocity microstructure, airfoil shear probes are the most established sensors. These probes have been employed for more than 20 years (Osborn, 1974). The behavior and the construction principles of these lift force sensors have been described in detail by Osborn and Crawford (1982), and Prandke and Stips (1996). The MSS Profiler is equipped with a shear probe PNS 93. This probe is based on shear probe developments at the former Institute of Marine Research Warnemuende (Neumann and Prandke, 1992).

The basic scheme of the shear sensor operation is shown in fig. 1.4.

Following Allen and Perkins (1952), the cross force per unit length due to the potential flow $f_p$ for an axially symmetric airfoil in an inviscid flow of speed $U$ and an angle of attack $\alpha$ , can be expressed as

$$f_p = \frac{1}{2}\,\rho\,U^2\,\frac{dA}{dx}\,\sin 2\alpha \tag{1.1}$$

where $\rho$ is the density of the fluid and $\frac{dA}{dx}$ is the rate of change in the airfoil cross section area in axial direction. The total cross force $F\tau$, equation 1.1 can be computed integrating $f_p$ along the axis from the tip to the position where $\frac{dA}{dx} = 0$ :

$$F\tau = \frac{1}{2} \cdot \rho \cdot U^2 \cdot A \cdot \sin 2\alpha \tag{1.2}$$

Using the double angle relation $\sin 2\alpha = \sin\alpha \cdot \cos\alpha$ equation 1.2 can be written as:

$$F\tau = \rho \cdot A \cdot V \cdot u \tag{1.3}$$

This equation shows the linear proportion between cross-stream velocity and cross-force. However, the speed of the probe in water also contributes to the cross-force. The constant axial velocity component $V$ is due to the sinking or rising velocity of the profiler. The vertical component of the turbulent velocity fluctuation is superimposed on the velocity of the profiler. However, the fluctuating velocity is much smaller than the speed of the profiler and is therefore not considered in the flow geometry at the tip of the shear probe.

Equation 1.3 consider only the theoretical response of the sensor. Prandke and Stips (1996) reviewed the limitations of assuming an ideal response and propose some corrections for non ideal cases.

### 1.2.2 Data acquisition and processing

The MSTB is the software package provided with the instrument. It can be used for microstructure data acquisition and evaluation and is specially designed for customers of the MSS profiler. It consists of a management program and many singular executable programs (modules) to carry out data acquisition and various steps of data processing. Although it is possible to combine different modules in a single macro, it is not possible to add new functions of signal processing. An interface program was developed for exchanging the data between the MSTB software and the Matlab package.

## 1.3 Parameter estimation

The first step for analyzing the field data is to compute some standard parameters which will be used as a basic input to obtain the microstructure descriptors.

In this section the standard parameters used in this thesis, and the method of computing them, are presented. The theoretical basis has been compiled mainly from Imboden and Wüest (1995), Wüest *et al.* (1996) and Massel (1999).

### 1.3.1 Density

The principal state parameter of water is density $\rho$. The density of the water controls many fundamental processes in the aquatic systems like the hydrostatic equilibrium, the motion of water particles, the propagation of internal waves or the turbulence and mixing in the water column. Even small alterations in density water result in great changes of water flow and its thermal and chemical status.

Unlike measuring salinity (or conductivity), temperature and pressure, there are no practical methods of measuring the density of water *in situ*. The equations of state provide the empirical equations that allow to express the density as a function of salinity, temprature and pressure.

**Computation procedure**

Density has been computed from temperature, pressure and conductivity profiles following the equations of state proposed by Chen and Millero (1986), which are specific for inland waters. Detailed information of the thermodynamic equations is given in the appendix section A.

### 1.3.2 Potential temperature and potential density

The pressure-dependent temperature (*in situ*) $T$ and density (*in situ*) $\rho$ are comonly replaced by potential temperature $\theta$, which compensates for the adiabatic warming, and potential density $\rho_\theta$,wich is a function of potential temperature at pressure of reference $p_0$. In this case $p_0 = 0$, as in inland waters is usually to take the water surface as the reference.

Potential temperature $\theta(z, z_0)$ of a water parcel at depth $z$ (positive upwards), is defined as the temperature of that water parcel if it were to be displaced isentropically from $z$ to $z_0$:

$$\theta(z, z_0) = T(z) - \int_z^{z_0} \Gamma\left(\theta(z, z'), p(z'), S(z')\right) dz' \tag{1.4}$$

where $\Gamma$ is the adiabatic lapse rate

$$\Gamma(T, p, S) = \frac{g\,\alpha}{c_p}\left(T + 273.15\ K\right) \tag{1.5}$$

where $= 9.8\ m\,s^{-2}$ is the acceleration gravity, $\alpha$ is the thermal expansivity and $c_p$ is the specific heat at constant pressure. The parameters $\alpha$ and $c_p$are functions of $T$, $p$, $S$ and are calculated from Chen and Millero (1986) equations.

Potential density is computed as

$$\rho_\theta = \rho(\theta, S, p_0) \tag{1.6}$$

and usually expressed as

$$\sigma_\theta = \rho_\theta - 1000 \tag{1.7}$$

**Computation procedure**

Potential temperature $\theta$ has been computed following the iterative procedure proposed by Wüest *et al.* (1996)

$$\begin{aligned} \theta^{(0)}(z, z_0) &= T(z), \\ \theta^{(i+1)}(z, z_0) &= T(z) - \int_z^{z_0} \Gamma\left(\theta^{(i)}(z, z'), p(z'), S(z')\right) dz' \end{aligned} \tag{1.8}$$

which converges well enough after 2 iterations ($\left|\theta^{(2)} - \theta^{(2)} < 10^{-4}\ ^oC\right|$, (Wüest *et al.*, 1996)).

### 1.3.3 Buoyancy frequency

This parameter is used to define the background stratification and the stability in the water column. The expression of this term is derived from the hypothetical case in which a fluid particle is displaced from its initial position in a stable density profile ($\partial\rho/\partial z < 0$, $z$ positive upwards). In this case the resulting buoyancy force tends to move the water particle to the original position. The movement of the water element is restrained by an inertial force, and the resulting balance of force can be expressed as

$$\rho \frac{d^2\xi}{dt^2} = g\,\Delta\rho \tag{1.9}$$

In which $\xi$ is the water displacement and $\Delta\rho$ is the resulting change of water density. Ignoring the water compressibility, from a power series of $\rho$, $\Delta\rho$ can be expressed as

$$\Delta\rho = \xi \frac{d\rho}{dz} \tag{1.10}$$

Substituting eq. 1.9 into eq. 1.10, yields

$$\frac{d^2\xi}{dt^2} + \left(-\frac{g}{\rho}\frac{d\rho}{dz}\right)\xi = 0 \tag{1.11}$$

The elementary solution of eq. 1.11 takes the form

$$\xi(t) = \cos(N\,t) \tag{1.12}$$

Where $N$ (which is a function of depth) is known as the Brunt-Väisälä frequency or buoyancy frequency

$$N = \sqrt{-\frac{g}{\rho}\frac{d\rho}{dz}} \tag{1.13}$$

Eq. 1.12 represents a simple harmonic motion of element of the fluid moving up and down. The frequency $N$ is maximum where the density gradient is the greatest. From eq. 1.12, the buoyancy frequency is expressed in $rad\ s^{-1}$ and a factor of $1/2\pi$ should applied in order to express this parameter in $s^{-1}$.

**Computation procedure**

Buoyancy frequency requires to compute the mean density gradient. This value is estimated by linear regression fit for the density profile in a selected depth interval. Once the mean density is obtained the buoyancy frequency is computed from 1.13.

### 1.3.4 Kinematic viscosity

Viscosity is a property which is a measure of a fluid's resistance to "deformation" during motion. Within a fluid, momentum of rapidly moving particles is exchanged with momentum of slower particles. Those exchanges produces shearing stress. At first instance, the shear stress $\tau$ (force per unit surface area) and the vertical shear velocity $du/dz$ is linearly related as

$$\tau = \mu\frac{du}{dz} \tag{1.14}$$

Where $\mu$ is the coefficient of dynamic molecular viscosity. As force on an element of fluid varies like $\mu$ but the mass of that element varies like $\rho$, the acceleration and hence the velocity field is determined by the ratio $\mu/\rho$. This ratio is known as the coefficient of kinematic viscosity $\nu$

$$\nu = \frac{\mu}{\rho} \tag{1.15}$$

The smoothing of the flow by viscosity is the way the energy in turbulence is finally converted to heat and dissipated. For this reason, viscosity plays an important role in turbulent dynamics.

**Computation procedure**

The coefficient of kinematic viscosity is weakly dependent on salinity and pressure but strongly dependent on temperature (see e.g., Siedler and Peters, 1989). The coefficient of kinematic viscosity has been computed from the polynomic approximation (ISW/SST, 1999)

$$\nu = \left(1.79247 - 0.05126103\,T + 0.0005918646\,T^2\right)\,10^{-6} \tag{1.16}$$

wher $T$ is the temperature $[^oC]$ and $\nu$ is the kinematyc viscosity $[m^2\,s^{-1}]$.

### 1.3.5 Turbulent dissipation rate

The dissipation rate of kinetic energy is one of the most used parameters for quantifying the level of turbulence and the resulting mixing processes in natural waters. Based on dissipation rate measurements, some of the turbulent parameters (like vertical diffusion coefficients or flux rates, which will be commented in next chapters) can be estimated (Osborn, 1980; Dewey and Crawford, 1988).

The dissipation rate of kinetic energy is defined from the analysis of the turbulent part of the advective motion. When considering a turbulent flow, the state functions are very complicated due to the wide range of temporal and spatial scales involved. A common procedure is the application of the Reynolds decomposition (Reynolds, 1894) in which every state function $f$ is splited into a mean value $\overline{f}$ and fluctuation $f'$

$$f = \overline{f} + f' \tag{1.17}$$

in which is implicit that $\overline{f'} = 0$.

The turbulent kinetic energy (TKE) is defined from the Reynolds decomposition to the velocity of the flow ($U_i = \overline{U_i} + u_i'$, where $i$ is any of the Cartesian coordinates x, y, z) as

$$TKE = \frac{1}{2}\sum_i \overline{u_i'^2} \tag{1.18}$$

and is the relevant property for describing turbulent mixing. For homogeneous conditions (no spatial gradients of TKE) the temporal change in TKE is due to the balance of TKE production from the mean flow $J_R$ (through the Reynolds' stress), the change of potential energy of the water column (known also as buoyancy flux, $J_b$) and the dissipation rate of kinetic energy $\varepsilon$ by viscous forces. This balance is expressed as (see Stull, 1988 for details)

$$\frac{\partial}{\partial t}(TKE) = \underbrace{-\sum_{ij}\overline{u_i'u_j'}\frac{\partial\,\overline{U_i}}{\partial x_j}}_{J_R} \quad \underbrace{-\overline{\rho' u_3'}\frac{g}{\rho}}_{J_b} \quad \underbrace{-\nu\sum_{ij}\overline{\left(\frac{\partial\,u_i'}{\partial x_j}+\frac{\partial\,u_j'}{\partial x_i}\right)\frac{\partial\,u_i'}{\partial x_j}}}_{\varepsilon} \tag{1.19}$$

From 1.19 it is necessary to estimate 12 terms of turbulence fluctuations in order to determine $\varepsilon$. However, for isotropic turbulence the terms are simply related and only one independent term remains. Under this precondition, the third term of equation 1.19 can be expressed as

$$\varepsilon = 7.5\ \nu\ \overline{\left(\frac{\partial\, u'}{\partial z}\right)^2} \tag{1.20}$$

Isotropic turbulence must be assumed for computing $\varepsilon$ from 1.20. This condiction can be assumed without any restriction in non-stratified flow, except near to walls, but in a stratified flow the stratification modifies the dynamic of turbulence. The effects of stratification can be parameterised by the nondimensional ratio $\frac{\varepsilon}{\nu N^2}$ (Stillinger *et al.*, 1983). Yamazaki and Osborn (1990), investigated the effect of stratification on dissipation rate estimates. They found for a value of $\frac{\varepsilon}{\nu N^2} > 20$ dissipation estimates for anisotropic turbulence comparable to the isotropic formula. For decreasing values of $\frac{\varepsilon}{\nu N^2}$ the errors increased, but were limited to less than 35 %.

**Dissipation rate computation from shear microstructure**

Calculations of dissipation rates following equation 1.20 can be made by integrating the shear spectrum. Integration is usually applied to determine the variance of the shear profile in a given segment. Equation 1.20 implicates that the full relevant wavenumber range of the vertical shear profile is considered. That is, the full spectrum of turbulent kinetic energy has to be resolved by the measuring device and has to be considered into the dissipation rate calculation. A theoretical form of the spectrum of turbulent kinetic energy was hypotesized by Kolmogorov (1941). The spectrum of turbulent kinetic energy covers the range from the wavenumber associated to the turbulent forcing ($k_F$) to the cut-off wavenumber limited by the effect of viscosity (fig. 1.5).

The cut-off wavenumber is known as the Kolmogorov radian wavenumber $k_K$ $[rad\, m^{-1}]$ (Kolmogorov, 1941)

$$k_K \approx \left(\frac{\varepsilon}{\nu^3}\right)^{1/4} \tag{1.21}$$

To obtain the dissipation range from the measured vertical shear profile, the variance of the shear has to be determined in the wavenumber range between $k_F$ and $k_K$. While the upper bound is clearly defined by the Kolmogorov wavenumber, the lower bound is not defined in a similar manner. In fact, there is no sharp separation between high frequency non-turbulent motions and low-frequent turbulent motions. Both processes interact and the

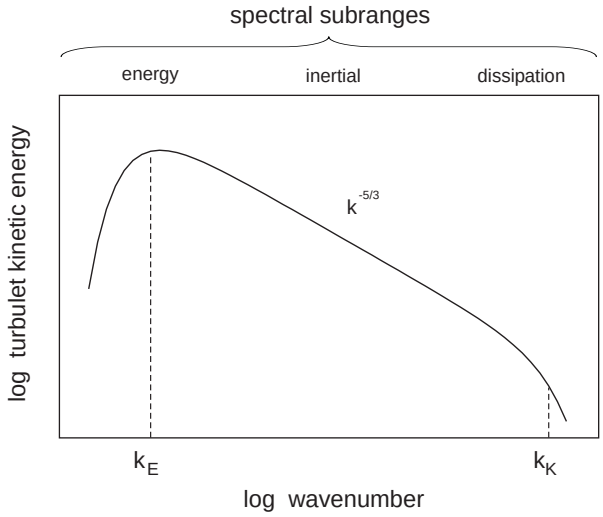


Figure 1.5: *kinetic energy for stationary, homogeneous, isotropic turbulence forced at wavenumber $k_F$ . Approximate locations of the energy containing, inertial, and dissipation subranges are indicated, along with the Kolmogorov wavenumber $k_K$. (Adapted from Smyth and Moum 2000.)*

scales partly overlap. Thus, the lower bound of the spectra for the dissipation rate calculation has to be set empirically (Pranke and Stips, 1996).

**Computation procedure**

The MSTB toolbox provides a function for computing $\varepsilon$ from the shear profile. Figure 1.6 shows an example of the final result of this procedure.

As an input parameters for this function it is necessary to set the initial bound values of the ciclic wavenumber spectra, $(\kappa_{\lim 1}, \kappa_{\lim 2})$. Empirical spectra data is usually expressed in ciclic wave numbers $\kappa$ $[m^{-1}]$, which can be related to radiant wavenumbers by $k = 2\pi\kappa$. The third input parameter for this function is the number of shear data values used for computing the spectrum, which determines the final vertical resolution of the turbulent dissipation rate profile.

Pranke and Stips (1996) proposed a cyclic wavenumber of 2 $m^{-1}$ for the lower bound of integration $\kappa_{\lim 1}$. While the lower bound is maintained as constant value, the upper bound changes iteratively according to the level of turbulence. This method has been developed in order to avoid an overestimation of the dissipation rate by high frequency noise of the shear sensor, especially at low turbulence.

As a first step the upper bound $\kappa_2$ is set to 22 $m^{-1}$ and the first estimation

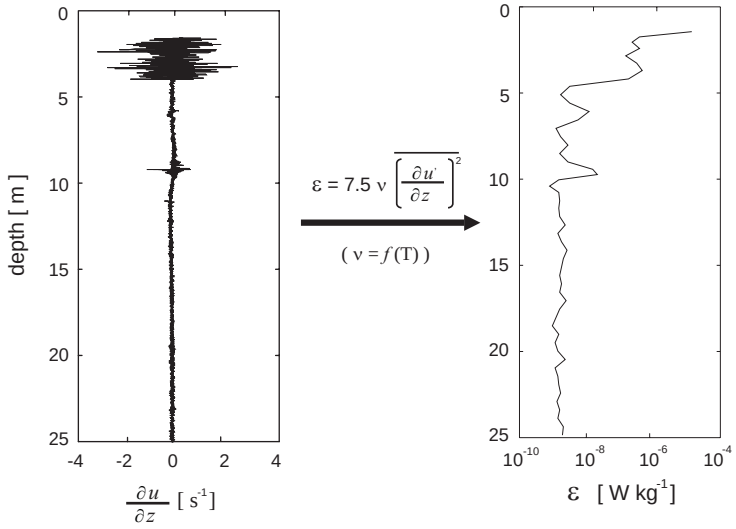


Figure 1.6: *Example of turbulent kinetic energy profile computed from shear profile using the MSTB function.*

of $\varepsilon'$ is computed according to eq. 1.20. Next, the cut-off wavenumber $\kappa_c$ is calculated from $\varepsilon'$ using eq. 1.21. The upper bound is increased iteratively until $|\kappa_2 - \kappa_c| < 2\ m^{-1}$ or $\kappa_2 > \kappa_{\lim 2}$.

### Dissipation rate computation from scalar microstructure

An alternate approach for the determination of the dissipation rate is based on scalar (usually temperature or salinity) microstructure measurements. A conservative scalar property (salt, temperature, etc.) mixed by a turbulent flow also produces a fluctuation (variance) spectrum. The spectrum of scalar variance covers the range from the wavenumber associated to the turbulent forcing ($k_F$) to the cut-off wavenumber limited by molecular properties. In this case the cut-off wavenumber not only depends on $\varepsilon$ and $\nu$ but also on the molecular difusivity $D_\theta$ of the scalar $\theta$. Batchelor (1959) developed the form of the scalar gradient wavenumber spectrum for isotropic, homogeneous turbulence (fig. 1.7).

The cut-off wavenumber $k_B$ is the Batchelor radiant wavenumber, defined as

$$k_B = \left(\frac{\varepsilon}{D_\theta^2\,\nu}\right)^{1/4} \tag{1.22}$$

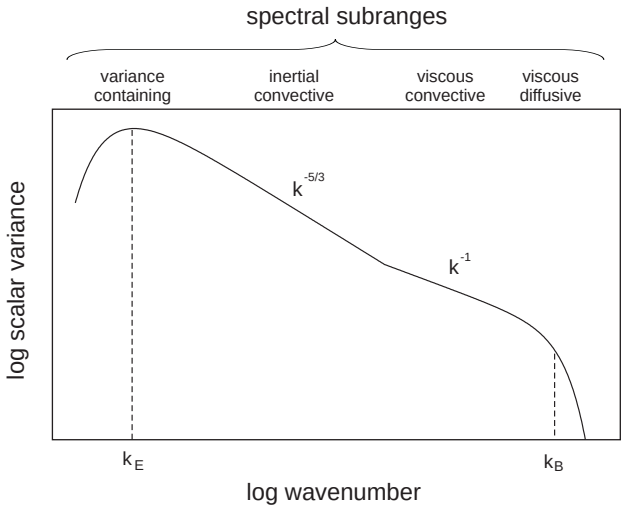


Figure 1.7: *Theoretical wavenumber spectra of scalar variance and dissipation for stationary, homogeneous, isotropic turbulence forced at wavenumber $k_F$. Approximate locations of the variance containing, inertial convective, viscous convective and viscous diffusive subranges are indicated, along with the Batchelor wavenumber $k_B$. (Adapted from Smyth and Moum 2000.)*

Gibson and Schwartz (1963) used Batchelor's results to derive the one-dimensional Batchelor spectrum $S(k)$ of the scalar gradient

$$S(k) = \frac{\chi_\theta}{2\,D_\theta}\frac{\sqrt{2q}}{k_B}S_N(\alpha) \tag{1.23}$$

where $\chi_\theta$ is the dissipation of scalar variance due to turbulence and is defined for the case of isotropic turbulence as (Monin and Yaglom, 1975):

$$\chi_\theta = 6D_\theta\int_0^\infty S(k)\,dk = 6D_\theta\overline{\left(\frac{\partial\,\theta'}{\partial\,z}\right)^2} \tag{1.24}$$

$k$ is the radiant wavenumber and $q$ is a universal constant.The dimensionless wavenumber $\alpha$ is a computed as $\sqrt{2q}\,k\,k_B^{-1}$ and the normalised spectrum $S_N(\alpha)$ is given by

$$S_N(\alpha) = \alpha\left[e^{-\frac{\alpha}{2}} - \alpha\int_\alpha^\infty e^{-\frac{x^2}{2}}dx\right] \tag{1.25}$$

The one-dimensional form $S(k)$ has been confirmed in laboratory experiments involving turbulence generated behind a grid (Gibson and Schwartz

1963), in the upper ocean (Dillon and Caldwell, 1980; Oakey, 1982) and in lakes (Imberger, 1985; Gloor, 1995).

The value of the universal constant $q$ was estimated to be $\sqrt{3} < q < 2\sqrt{3}$ from theoretical arguments advanced by Gibson (1968a, b). Grant *et al.* (1968) estimated $q = 3.9 \pm 1.5$ and Dillon and Caldwell (1980) used $q = 2\sqrt{3}$. Oakey (1982) determined $q = 3.67 \pm 1.52$ by comparing direct measurements of dissipation with those obtained from temperature gradient spectra. In this thesis a value of $q = 2\sqrt{3}$ has been assumed.

Using 1.24 it is possible to determine $\chi_\theta$ from the experimental data. In this case, the Batchelor wavenumber $k_B$ can be determined by fitting the experimental gradient scpectra to the theoretical from by applying eq. 1.23 and using $k_B$ as a free parameter. Once the Batchelor wavenumber is determined, the turbulent dissipation rate can be computed from eq.1.22 as

$$\varepsilon = k_B^4 \, D_\theta^2 \, \nu \tag{1.26}$$

A comparison of dissipation rates determined from shear and temperature microstructure measurements was done by Oakey (1982) showing an agreement within a factor of 2 on average at dissipation rates ranging from $\varepsilon \in [8 \cdot 10^{-9} - 5 \cdot 10^{-7}] \; W\,kg^{-1}$.

However, it is not always possible to fit the scalar gradient spectra to the theoretical form due to diverse instrumental or environmental restrictions. Examples of these limitations are the instrument noise at the high wavenumber end of the spectra (Gregg *et al.* 1986), the internal wave and finestructure 'masking' at the low wavenumber end of the spectra (Gregg 1977a, b), and the lack of a clearly defined viscous-convective subrange (Sherman and Davis, 1995). In these cases, the final value of $\varepsilon$ is unresolved. For these reasons turbulent scalar spectra fitting is still a field of research and several methods are recently proposed to improve the fitting method (Ruddick *et al.*, 1999; Luketina and Imberger, 1999).

**Computation procedure**

The turbulent dissipation rate computed from the temperature gradient profile has been obtained following Imberger and Ivey (1991). The temperature gradient spectrum is computed from the Fourier analysis of the temperature profile. To overcome the difficulty of the nonstationary nature of the temperature gradient signal a segmentation algorithm has been applied. Figure 1.8 shows an example of the different computed profiles for estimating the turbulent dissipation rate.

Briefly, the method consists of fitting an autoregressive (AR) model of order $p$ separately to two adjacent windows of the data corresponding to the temperature gradient. The resulting AR coefficients from both windows are

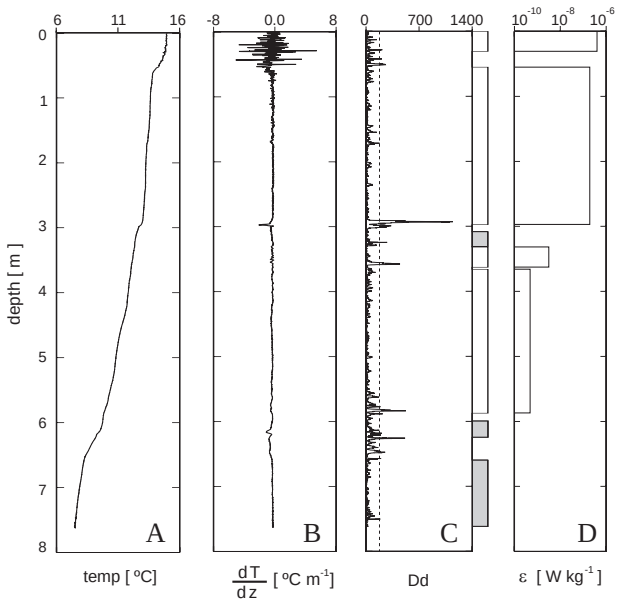


Figure 1.8: *Schematics of the different steps involved to computed the rate of the turbulent dissiaption rate from the temperature gradient profile. (A) Temperature profile. (B) Temperature gradient profile. (C) The norm distance computed using autoregressive models of order 4 and windows with a total of 64 points (see text). The selected threshold (dotted line) yields a total of 7 segments (rectangles on the left). (D) Dissipation of turbulent kinetic energy computed from the segments. In some cases it was not possible to fit the Batchelor spectrum to the data and the segment was labeled as gray rectangles in (C).*

used to estimate the distance between the two data sets. The distance is evaluated with a norm and provides a parameter of stationarity. For large values of the norm the time series within the two windows are assumed to be different to each other and the series deemed nonstationary. The regions of stationary behavior are determined by sliding the two adjacent windows point by point through the record and detecting where the norm exceeded a certain threshold (fig. 1.8 C). Once the stationary segments have been determined, standard fast Fourier transform analysis is applied to each segment from which the dissipation of turbulent kinetic energy is computed (fig. 1.8 D). Example of unresolvable segments are labeled in fig. 1.8 C as gray rectangles.

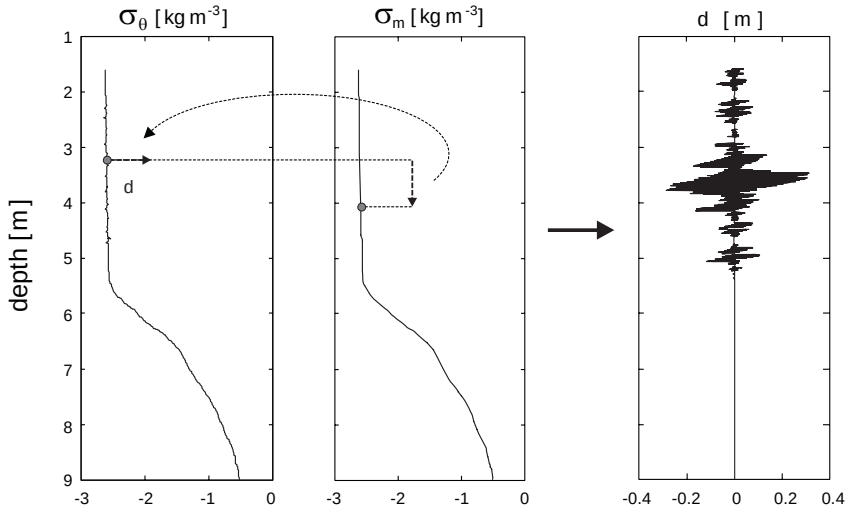


Figure 1.9: *Schematic procedure for computing the Thorpe displacement profile* $d_T(z)$. *The first step is computing a reference density profile* $\sigma_m(z) = \rho_m(z) - 1000$ *by sorting the original density profile* $\sigma_\theta(z) = \rho_\theta(z) - 1000$. *The* $d_T(z)$ *is computed by comparing the relative position of each water parcel in both density profiles* $\sigma_\theta(z)$ *and* $\sigma_m(z)$.

### 1.3.6 Thorpe displacement

In stratified fluids, turbulent mixing generates instabilities on the density profile that can be used to obtain some properties of the dynamics of turbulence. Thorpe (1977) proposed an algorithm for characterizing the instability structures generated by turbulence in a density profile. In this algorithm a reference density profile $\rho_m(z)$ is computed by sorting the original density profile $\rho_\theta(z)$. Two different values can be computed from these density profiles: the density fluctuation, defined as $\rho'(z) = \rho_\theta(z) - \rho_m(z)$ and a Thorpe displacement $d_T\ (z)$. Thorpe displacement is the vertical distance that an individual fluid particle (*i.e.*, a single density value of the original profile $\rho_\theta(z)$ has to be moved in order to generate the stable density profile $\rho_m(z)$). Figure 1.9 represents an schematic example the different steps for computing a $d_T$ profile.

Thorpe displacement $d_T$ is a key parameter in turbulent patch characterization. As it will be shown in the following chapters, the most relevant properties of the turbulent patches are mainly derived from this parameter.

# Chapter 2

# Turbulent patch identification

## 2.1 Introduction

One of the objectives in analyzing microstructure density profiles, is to identify turbulent patches and computing its characteristic vertical length ($L_p$). Patch identification is an important issue in turbulence characterization, as mixing occurs in patches produced by multiple mechanisms over a wide range of space and time scales.

Some turbulent physical characterization can be focused on the energetic parts of the vertical microstructure records, avoiding problems related with instrumental noise (*e.g.*, Gregg, 1987; Moum, 1996a), but biological-physical processes should be characterized in a wider turbulent environmental range. Vertical differences in population dynamics and selective processes among planktonic algae (Reynolds, 1992) or zooplankton distribution (Haury *et al.*, 1990) can be related to differences in turbulent regimes. For this reason, a new method for turbulent patch identification is proposed. The method has been implemented in order to be applicable in a wide range of density gradients

## 2.2 Methods of turbulent patch identification. A brew review

Several algorithms and tests have been proposed for turbulent patch identification based on density (or associated scalars, *i.e.* salinity or temperature) profiles. Statistical properties of $\rho'_{(z)}$ or $d_T\ (z)$ profiles obtained from Thorpe's method (Thorpe, 1977) are usually the main input for the algorithms of turbulent patch identification.

Nowadays, there is no accepted statistical model of overturning that can be used as a reference for validating the computed density fluctuation or Thorpe displacements profiles. The lack of any theoretical model has forced to find methods for turbulent patch identification based on heuristic reasoning and empirical parameters.

Dillon (1982), defined a complete overturn (*i.e.*, a mixing patch) as the region where no heavier or lighter fluid particle in $\rho_{(z)}$ relative to $\rho_m(z)$ are found outside the patch, and no heavier or lighter fluid particles relative to $\rho_m(z)$ outside the patch are found inside. The method relies on the ability to resolve density fluctuations on scales much less than the typical particle displacement necessary to create theconsecutive zero crossing density fluctuations are smaller than a certain threshold. In order to avoid the potential artifacts caused by instrumental noise, only strongly pronounced patches (that implies a relative high background density gradient) are usually considered (Prandke and Stips, 1992).

Moum (1996a, 1996b) proposed two conditions for validating a turbulent patch: (1) Turbulent patches should contain only data with all fluctuation signals significantly different from their respective noise levels. (2) Turbulent patches must have well defined upper and lower boundaries which yields in two specific requirements: $L_{Tmax} < L_p$, where $L_{Tmax}$ denotes the maximum Thorpe displacement throughout the patch; and $\int d_T(z)\ dz$ over the range depth of the patch should be equal to 0. The first condition requires a relatively high stratification background level in order to obtain high values of fluctuation.

Galbraith and Kelley (1996) proposed an alternative test, which was initially developed for CTD profiles, but it can be used with microstructure data as well. The test is implemented in two parts. In the first part the test is focused on the artifacts derived from random noise. Density fluctuations are examined for "runs" of adjacent positive or negative values, defining the run-length as the number samples contained in each run. The probability density function (PDF) of the run-length is compared with the PDF expected from random noise series. As a diagnostic of the typical run length within a patch, the authors choose the root mean square (*rms*) value. With the addition of increasing amount of random uncorrelated noise to the observed profile the *rms* value decreased. This yields a threshold value for rms run-length within an individual turbulent patch that must be exceeded for validating it. Patches with rms run-length below the threshold are considered artifacts generated from random noise. The second part of the test rejects the artifacts derived from systematic errors such as salinity spikes, caused by time-response mismatches in temperature and conductivity sensors. Temperature and salinity covariations with respect to density are screened within

the turbulent patch, and only the patches with tight relationships between $\rho$, $T$ and $S$ are validated. Calibration with examples from coastal and deep-sea environments indicates that it is possible with this test turbulent patch validation in environments with large stratification, but that noise will prevent patch validation in a weakly stratified environment.

The common feature of all the methods listed above is a general lack in identifying turbulent patches at low-density gradient. Here we proposed a new method that significantly improves patch detection at low-density gradients. The method is designed to reject patches caused by random noise, it does not replace the need for careful data acquisition practices and post-processing techniques to minimize the effects of systematic errors as salinity spiking.

## 2.3 Constraints on turbulent patch identification

Instrumental limitations derived from resolution and noise imposes basic constraints on turbulent patch detection. Assuming that turbulent patches can be identified from non-null values of Thorpe displacements, the limit for patch identification resides on the capacity to distinguish between displacements caused by instrument noise and displacements generated by turbulent processes.

It is not necessary to know the numerical value of $d_T$ for displacement validation, only two conditions are required: (1) the displacements are different than 0 and (2) the error associated to each displacements ($E_{d_T}$) should be smaller than the displacement itself.

In order to evaluate $E_{d_T}$ an error analysis has been developed based on the solidbody rotation model (Itswire *et al.*, 1986; Imberger and Boashash, 1986), where a cylindrical overturning eddy in a linear density profile yields a Z-shaped $\rho_{(z)}$ segment(fig. 2.1).

In this model, it is possible to express the length of the theoretical displacement $d_T$ as a function of the stable density gradient (*i.e.*, the local gradient computed from the monotonic profile), and the magnitude of the density fluctuation $\rho'$:

$$\frac{d\rho_m}{dz} = \tan(\alpha) = \frac{\frac{\rho'}{2}}{\frac{d_T}{2}} \rightarrow d_T = \frac{\rho'}{\frac{d\rho_m}{dz}} \tag{2.1}$$

From (2.1) is possible to derive the relative error of $d_T$ as

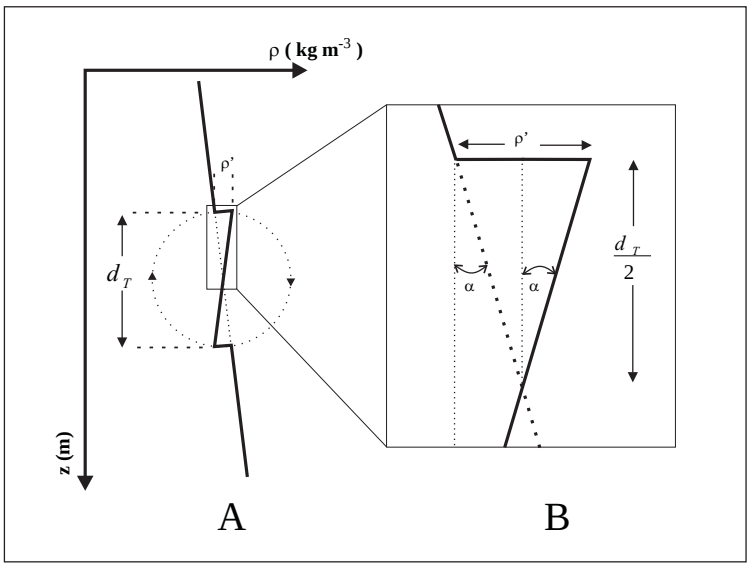


Figure 2.1: *A. Model of solidbody overturn. B Detail showing the relevant magnitudes.*

$$\frac{E_{d_T}}{d_T} \approx \frac{E_{\rho'}}{\rho'} + \frac{E_{\frac{d\rho_m}{dz}}}{\frac{d\rho_m}{dz}} \tag{2.2}$$

Since the local density gradient computation is based on a greater number of measurements than the density fluctuation, we can neglect the contribution of the relative error of the monotonic density gradient. Then, from (2.1) and (2.2)

$$E_{d_T} \approx \frac{E_{\rho'}}{\frac{d\rho_m}{dz}} \tag{2.3}$$

The error of Thorpe displacements $E_{d_T}$ is derived as a function of 2 parameters: the density gradient (which will be imposed as a background condition) and the error on density fluctuation $E_{\rho'}$. Improving turbulent patch detection requires minimizing $E_{d_T}$, which is only possible by reducing $E_{\rho'}$. In this case it is necessary to find a method for optimal density recovering, that should minimize the noise from the density profile without loosing the small density perturbations derived from the overturn motions at low-density gradients.

## 2.4 A wavelet analysis approach to noise reduction

In the last few years, there has been considerable interest in the use of wavelet transforms for removing noise from data. When data are intermittent in nature, as is the case of density fluctuations, wavelet analysis is highly advantageous over either Fourier or real-space analysis (Pen, 1999).

The wavelet transform of a function $f(x)$ with finite energy is defined as the integral transform with a family of functions $\Psi_{\lambda,\tau}(u) \equiv \frac{1}{\sqrt{\lambda}}\Psi\left(\frac{u-\tau}{\lambda}\right)$and is given as

$$W\ f(u) = \int_{-\infty}^{\infty} f(u)\ \Psi_{\lambda,\tau}(u)\ du = \int_{-\infty}^{\infty} f(u)\ \frac{1}{\sqrt{\lambda}}\Psi\left(\frac{u-\tau}{\lambda}\right)\ du \quad (2.4)$$

Where $\lambda$ is a scale parameter, $\tau$ a location parameter, and $\Psi_{\lambda,\tau}(u)$ are called wavelets. In the Continuous Wavelet Transform (CWT) the wavelet transform can be computed for every value of $\lambda$ and $\tau$. For empirical measurements, discrete wavelet transform (DWT) are preferable since $f(x)$ is known at discrete points ($x = n_j$). This requires de discretization of 2.4 in the scale and space domain. The discretization of the domain of 2.4 is not arbitrary since conservation of the amount of information in the signal is necessary. The simplest and most efficient case for practical computation is the dyadic arrangement (Daubechies, 1992; Mallat, 1989) where $\lambda = 2^m$ and $\tau = j\,2^m$ resulting

$$DW\ f(m,j) = \sum_{n=-\infty}^{\infty} f(n)\ \Psi_{m,j}(n)\ = \sum_{n=-\infty}^{\infty} f(n)\ \frac{1}{\sqrt{2^m}}\Psi\left(\frac{u-j\,2^m}{\lambda}\right) \quad (2.5)$$

Mallat (1989) produced a fast wavelet ($FWT$) algorithm that computes the $DWT$ very efficiently. The Mallat algorithm is a classical scheme in signal processing known as a two channel subband coder using quadrature mirror filters (QMF). The original signal is first decomposed into low and high frequency components by the convolution-subsampling operations with the pair consisting of a "lowpass" filter and a "highpass" filter directly on the discrete domain. The low frequency components (approximation coefficients) keep the global features of the signal and the high frequency components (detail coefficients) retain the local features. The decomposition process can be iterated recursively on the approximation coefficients while the detail coefficients are retained intact. At the last iteration, both approximation and

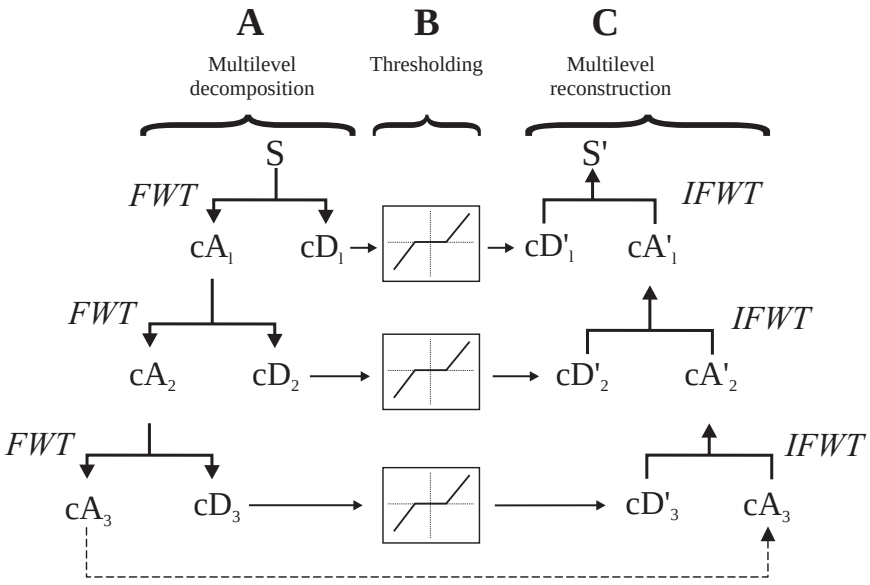


Figure 2.2: *Schematic diagram of the three steps of the denoising method: Multilevel decomposition, thresholding and multilevel reconstruction.*

detail coefficients are kept. By applying such decomposition to the measured data (Cohen *et al.*, 1993), it is possible to obtain empirical wavelet coefficients associated to different levels of local characterization.

The method for noise reduction here proposed is derived from a wavelet-thresholding algorithm based on Mallat's scheme (Donoho and Johnstone, 1994; Donoho, 1995), and it comprises three main steps as exposed in figure 2.2:

– Multilevel decomposition. Fast wavelet transform, $FWT$, (Mallat, 1989) is applied for decomposing the signal in different levels of local characterization. Figure 2.2 A graphically represents an example of this hierarchical decomposition. In this example, the level of decomposition has set to 3, yielding one series of approximation coefficients ($cA3$) and a set of three different detail coefficient signals ($cD1, 2, 3$).

– Thresholding. The method assumes that the noise can be modeled as a random Gaussian signal so the major part of the noise is finally stored in the detail coefficients. In order to reduce the noise contribution, a threshold function is applied to the detail coefficients, thereby suppressing those coefficients smaller than certain amplitude (fig. 2.2 B).

– Multilevel reconstruction. A denoised profile can be recovered from the transformed coefficients, applying recursively the Inverse Fast Wavelet

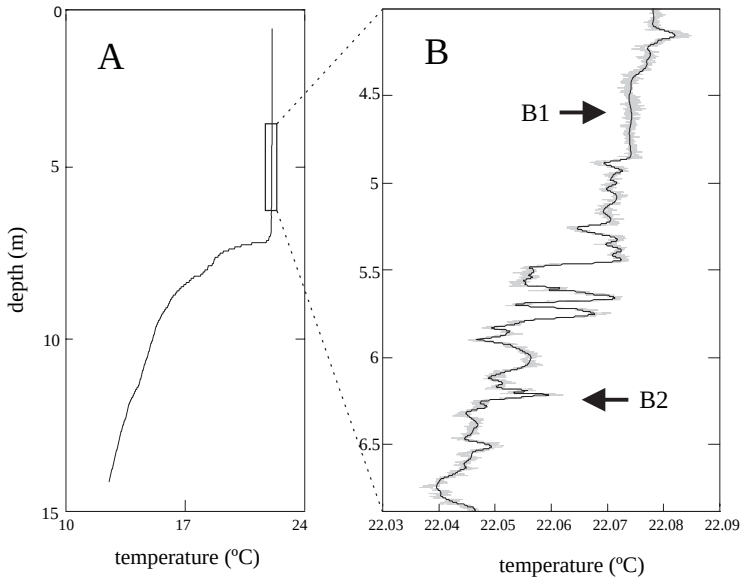


Figure 2.3: *Example of the denoising method applied to a real temperature profile. (B) Detail of the profile showing that the method smoothens the segments in which there are no significant changes (B1) but keeps the small perturbations generated at low-density gradients (B2).*

Transform ($IFWT$) over each level of decomposition (fig. 2.2 C).

This method, as many statistical techniques for noise reduction, optimizes the mean square differences between the original and the denoised signal. One of the most important advantages of this method is that it not only optimizes the mean squared error but also assures, with high probability, that the denoised signal is at least as smooth as the original (Donoho, 1995). Alternative techniques that simply optimize the mean squared differences can generate, in some cases, undesirable noise-induced structures ("ripples", "blips" and oscillations). Such noise-induced structures may generate interpretative artifacts on density fluctuations and Thorpe displacements. Figure 2.3 shows an example of the advantages of the multiscale approach of this method. Unlike the classic low-pass filtering applications,it is possible to smooth the segments where there are no significant changes (fig. 2.3 B1) while keeping the small perturbations generated at low-density gradients (fig. 2.3 B2).

### 2.4.1 Noise sensitivity analysis. Theoretical test

With no accepted statistical model of overturning, there is little guidance to confirm from field data whether density fluctuations are caused by over-

| **Segment depth** | | | **overturn** | |
|---|---|---|---|---|
| Num | Interval | $N^2$ | depth | length |
| | depth $(m)$ | $(s^{-2})$ | $(m)$ | $(m)$ |
| 1 | 0.0 - 1.5 | $6.25\,10^{-6}$ | 0.75 | 0.2 |
| 2 | 1.5 - 2.0 | $4.00\,10^{-6}$ | 1.75 | 0.2 |
| 3 | 2.0 - 2.75 | $2.25\,10^{-6}$ | 2.35 | 0.2 |
| 4 | 2.75 - 4.25 | $1.00\,10^{-6}$ | 3.50 | 0.3 |
| 5 | 4.25 - 7.25 | $2.50\,10^{-7}$ | 5.00 | 0.4 |
| | | | 6.50 | 0.3 |

Table 2.1: *Features of the five segments of the theoretical profile used for testing the numerical limitations of the denoising method.*

turning motions or are artifacts from instrumental noise or numerical post processing. For this reason a set of theoretical profile has been designed for quantifying the potential error of $d_T$ in the proposed denoising method. The theoretical profiles are based on the solid-body rotation model. Although this model is an oversimplification of real structures, it is easy to check the error contribution comparing the theoretical Z-shaped structures with the final result. With this test, it is not possible to guarantee the optimal recovering on real data, but gives some clues about the limitations of the numerical method. The test has been designed by considering the worst field conditions that can be found, low buoyancy frequencies and small overturn sizes, in order to determine the resolution limits for patch detection. The first test profile comprises five segments, each with a different associated buoyancy frequency. Hypothetical overturns were simulated in each segment. In the fifth segment (the most critical), two overturns of different length were simulated. Complete descriptive details are shown in table 2.1.

The rest of the theoretical profiles were constructed adding to the initial profile increasing levels of zero mean Gaussian white noise. The first noisy profile was obtained adding a noise signal with variance $N_\sigma$ equal to $6.25 \cdot 10^{-8}\, kg^2 \cdot m^{-6}$, value derived from the density error variance equation (Gregg, 1979) calculated from laboratory test measurements . To consider added uncertainties in field measurements, a factor of 50 % and 100 % increase in noise was also computed, yielding two new density profiles with noise variance $N_\sigma$ of $1.40 \cdot 10^{-7}$ and $5 \cdot 10^{-7} kg^2 \cdot m^{-6}$ respectively. The procedure for noise estimation is detailed in the appendix, section B.

The test has been developed in two steps. In the first step the denoising method has been applied over the noisy theoretical density profiles. Multilevel wavelet transform has been based on Daubechies wavelet

(Daubechies, 1992) and the level of decomposition has been set to 9.

The detail coefficients were transformed applying a soft threshold function (Donoho, 1995):

$$cD' = \begin{cases} sgn\,(cD) \cdot (cD - thr) & cD > thr \\ 0 & cD < thr \end{cases} \tag{2.6}$$

With this function, the coefficients smaller than the threshold $thr$ are suppressed while the rest of the coefficients are shrunk an equivalent of the threshold value. The threshold value has been selected as

$$thr = \sigma\sqrt{2\,\log\,(n)} \tag{2.7}$$

where $n$ is the number of samples and $\sigma$ is a rescaling factor estimated from the noise level present in the signal (Donoho and Johnstone, 1994). The estimation of the noise level has based on first level of detail coefficients ($cD_1$) well suited for zero mean gaussian white noise in the denoising 1-D model (Misiti *et al.*, 1996).

$$\sigma = \frac{median\,(|cD_1|)}{0.6745} \tag{2.8}$$

Once the synthetic density profiles were denoised, the Thorpe displacements have been computed comparing the result calculated from the original theoretical profile (without noise) to the Thorpe displacements calculated from the denoised density profiles.

Figure 2.4 shows the graphical results of this test. Comparing the denoised results (2.4 C-E) with the expected profile (2.4 B) it is shown that overturns were clearly resolved in the first four segments. In the last segment, the most critical because it has the lowest density gradient, noise was reduced considerably but its effects yielded a significant error in the estimation of the displacements, and some spurious overturns appeared.

## 2.5 Local gradient classification method for patch identification

In order to overcome the artifacts from the remaining noise, a complementary method was implemented, based on a semiquantitative analysis of $d_T$.

The method was based on the comparison between the displacement $d_T$ and its error $E_{d_T}$. The error $E_{d_T}$ was computed from (2.3). $E_{\rho'}$ was estimated from the error associated to the sensors of temperature, conductivity and pressure, following Gregg (1979) and Luketina (1986). The local density

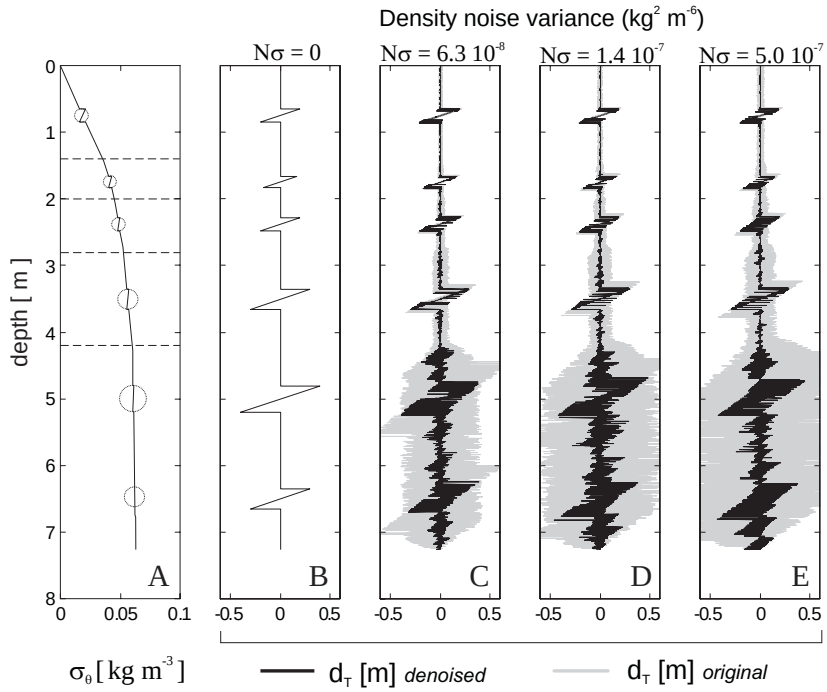


Figure 2.4: *Noise sensitivity test applied to $d_T$ computation. (A) Theoretical density profile used for the test. The circles indicate the depth and size of the theoretical overturns. (B) $d_T$ profile computed from (A). (C-E) $d_T$ profiles computed from A adding increasing levels of noise ($N\sigma$). The $d_T$ profiles obtained with (black) and without (gray) applying the denoising method. See text for further details.*

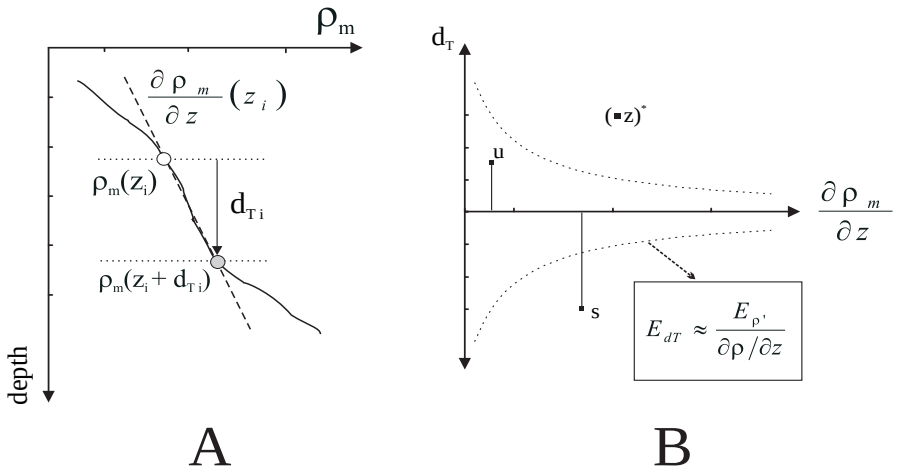


Figure 2.5: *Diagram of the of local gradient classification method. (A) Scheme of the local density gradient computation. (B) Comparing displacement values with their potential error allows the classification of each displacement into one of the following categories: Zero (*Z*), Uncertain (*U*) and Signal (*S*).*

gradient (that can change significatively depending on the scale considered) has been computed over the depth range defined by the depth of the particle in the original profile and the depth associated to the monotonic profile (fig. 2.5 A).

The comparison between the displacement and its potential error were categorized in three possible states (fig. 2.5 B). The sample is labeled as Zero (Z) when it has the same associated depth in the original and the monotonic density profiles (*i.e.* $d_T = 0$). The label Uncertain (U) was assigned when Thorpe displacement was smaller than the associated error. Finally, the label Signal (S), was assigned when the value of the displacement was bigger than the associated error. In this case it was possible to assure that the sample had non-null Thorpe displacement.

Two statistical indexes were defined considering the percentage of each data category in a depth range. The displacement index ($I_D$) was computed as the quotient between the number of S values and the number of averaging points. It indicates the percentage of samples that unambiguously have displacements different than zero. The uncertainty index ($I_U$) was computed as the quotient between the number of points on state U and the number of averaging points. It provides an estimation of the measurement uncertainty.

The displacement index ($I_D$) was used as the parameter for turbulent

patch identification. Segments with $I_D$ equal to zero were assumed to delimit the turbulent patches, and thus turbulent patches were identified as segments with strict positive $I_D$ values.

### 2.5.1 Noise sensitivity analysis. Theoretical test

Following the same approach of the denoising procedure test, the set of theoretical profiles with different noise levels (fig. 2.4) was used for evaluating the limits of the method. $I_D$ and $I_U$ were computed over 50 points, which is reasonable for statistical robustness and spatial resolution (50 samples corresponds approximately to 5 cm for spatial resolution of 1 mm, a common value in microstructure profiles). Figure 2.6 shows the results of the indexes computed from the sensitivity test profiles. $I_D$ values are represented as solid dark-gray areas, while $I_U$ values are in light-gray. The theoretical $I_D$ profile (fig. 2.6 B) shows how turbulent patches can be delimited as segments of strict positive $I_D$ values, although in the fifth segment, each overturn were split in two different patches due to the low displacements in the central part of the overturns. The ID profiles computed from the increasing noise profiles (fig. 2.6 C-E) were solved in a very similar way but several false patches of small size appeared. One example of these false patches was pointed with an arrow in fig. 5E. However, even for the noisiest profile (fig. 2.6 E) it was possible to reject the false patches from the rest computing the mean $I_D$ associated to the patch (fig. 2.6 F). All the false turbulent patches were characterized by small values of $\langle I_D \rangle$. As an example, the mean value of the false patch pointed in fig. 2.6 E was also pointed in fig. 2.6 F. Computing the mean value for every patch it is possible to define a threshold of $\langle I_D \rangle$ to reject the false patches generated by noise. In this test the threshold was determined as $Thres_{\langle I_D(50) \rangle} = 0.1$ (dotted line in fig. 2.6 F).

The index $I_U$ was computed to show how the level of uncertainty increases with some noise added to the original profile. The high level of uncertainty is the main reason to explain why many algorithms fail in turbulent patch detection at low-density gradients. However, the results obtained in the test suggest that $I_D$ is a robust parameter for turbulent patch identification, as it is computed only from validated displacements.

## 2.6 Application to field data

Four series of microstructure profiles were used to test the proposed method. The data was obtained from sensors mounted on the MSS and MP profilers. MP profiles were obtained rising the profiler at nominal rate of 0.1 m/s and

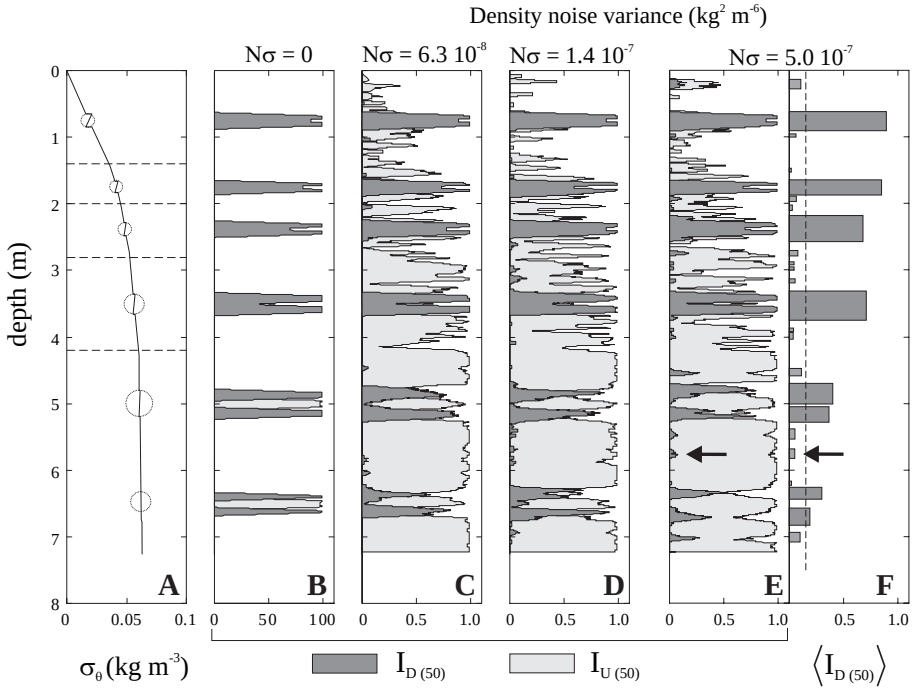


Figure 2.6: *Noise sensitivity test applied to $I_D$ index computation (in dark grey). (A) Theoretical density profile used for the test. Circles indicate the depth and size of the theoretical overturns. (B) Displacement index ($I_D$) in dark gray and uncertainty index ($I_U$) in light gray computed from A. (C-E) $I_D$ and $I_U$ computed from A with increasing levels of noise added ($N\sigma$). An example of false patches is indicated by an arrow in (E). (F) Mean displacement index computed from every patch detected in E; a threshold $Thres_{ID(50)}$ = 0.1 has been represented (in dotted line) showing that all the false turbulent patches are below this value. See text for further details.*

| **Reference** | **Profiler** | **Depth mean (max)** $(m)$ | **Total area** $(m^2)$ | **Volume** $(m^3)$ |
|---|---|---|---|---|
| Boadella Reservoir | MSS | 17.0 (54.0) | $3.6\,10^6$ | $62\,10^6$ |
| Sau Reservoir | MP | 26.3 (55.0) | $5.8\,10^6$ | $124\,10^6$ |
| Lake Banyoles | MSS | 15.7 (45.0) | $1.1\,10^6$ | $17\,10^6$ |

Table 2.2: *Characteristics of the reservoirs and lake from where the field data surveys were conducted.*

sampling data at 100 Hz, while MSS profiles were obtained falling the profiler at nominal rate of 0.6 m/s and sampling data at 1024 Hz. In both cases, the spatial resolution is close to 1 sample/mm.

The profile series were obtained in three different field surveys. In each series a fixed depth range was selected to illustrate different background density gradient. The surveys were performed at Sau Reservoir, Boadella Reservoir and Lake Banyoles, situated in the north of Catalonia, Spain. The table 2.2 summarizes the morphometric features of these three fresh-water systems. In these fresh-water systems, with low salinity and low salinity stratification, it is possible to neglect the contribution of salinity variations to density changes. Therefore, the main problem in detecting turbulent patches was exclusively derived from noise instrumentation in temperature measurements, avoiding problems from mismatches of the sensors in time response.

### Data processing

The profiles were processed following the proposed methodology. First, a denoised temperature, and pressure profiles were obtained following the algorithm mentioned in a previous section.

Turbulent patches were identified applying the semiquantitative analysis of the Thorpe displacements, which were computed from the potential density profiles. The indexes of displacement and uncertainty were computed over 50 points, and the patches were identified from the segments with strictly positive $I_{D(50)}$ values. Figure 2.7 shows an example of the computed $d_T$, $I_{D(50)}$ and $I_{U(50)}$ profiles for one of the profile analyzed in Boadella reservoir.

The turbulent patches were characterized by computing its vertical length Lp, and the maximum Thorpe displacement throughout the patch $L_{Tmax}$.

### Results

The test proposed by Moum (1996 a,b) was used for validating the turbulent patches obtained from the profiles. That is: $L_{Tmax} < L_p$, and $\int_{L_p} d_T\, dz = 0$.

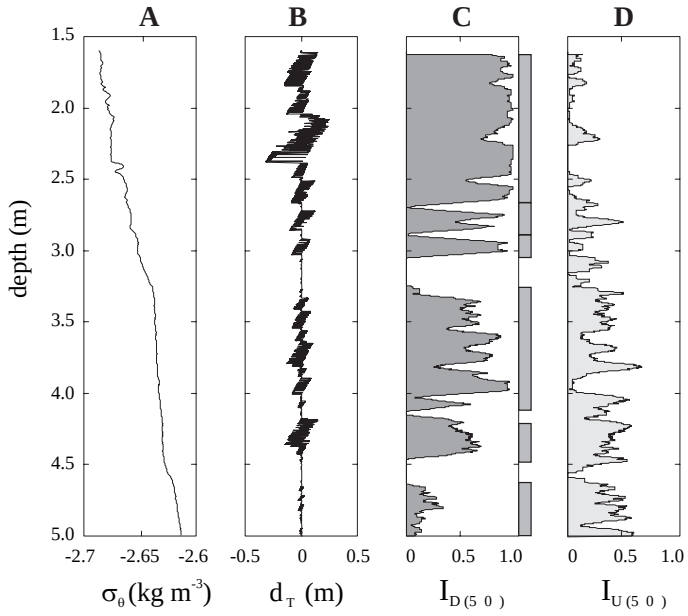


Figure 2.7: *Example of $I_D$ and $I_U$ computation with field data, corresponding to one of the profiles obtained in the Lake Banyoles. (A) Potential density. (B) Thorpe displacement. (C) $I_D$ index. Rectangles indicate the range depth of the patches identified. (D) $I_U$ index.*

| **Reference** | **Depth range** $(m)$ | $\mathbf{N^2}$ $(\mathrm{x}10^{-5})$ $(s^{-2})$ | **Total profiles** | **Patch detected** | **Patch rejected** |
|---|---|---|---|---|---|
| Boadella | $7.0 - 9.0$ | $12.5 - 20.2$ | 27 | 41 | $5 - 0$ |
| Banyoles | $7.0 - 9.0$ | $4.99 - 13.93$ | 82 | 90 | $3 - 0$ |
| Sau | $10.0 - 16.0$ | $2.59 - 5.73$ | 42 | 46 | $8 - 8$ |
| Banyoles | $0.0 - 4.5$ | $0.12 - 1.06$ | 83 | 181 | $9 - 16$ |

Table 2.3: *Results of the turbulent patches obtained from the series of profiles. The first column indicates the range depth considered in each series. The buoyancy frequency computed from the range depth has been included and shows the differences in background density gradient. Patches were rejected following two criteria: (First value) The mean ID was below the threshold (ThresID(50) = 0.1) or (second value ) the patches failed Moum's test.*

In order to consider the error in computing the Thorpe displacement, the second condition was relaxed to $\int_{L_p} d_T \, dz < 0.05 \, L_p$.

Table 2.3 summarizes the results for the different profiles series. The series has been tabulated from the highest ($N^2 = O(10^{-4})$) to the lowest ($N^2 = O(10^{-6})$) background density gradients.

A total of 358 patches were identified but 25 were rejected considering that the mean $I_D$ were below the threshold ($Thres_{I_{D(50)}} = 0.1$). The final result yields a total of 333 turbulent patches identified with 309 (92.3 %) validated following Moum test and only 24 (6.7 %) rejected. This high percentage of validated patches shows the robustness of the method for detecting turbulent patches in a wide range of density gradients.

Figure 2.8 shows the plot of patch length ($L_p$) and maximum Thorpe displacement ($L_{Tmax}$) associated to the turbulent patches detected. The rejected turbulent patches have been represented as solid circle, showing that all the rejected turbulent patches have a very small patch length value.

## 2.7 Summary and conclusions

A new algorithm for identifying turbulent patches and computing its vertical scale ($L_p$), based on wavelet denoising and semiquantitative analysis of Thorpe displacement ($d_T$) was presented. The denoising algorithm has demonstrated to be very effective in reducing the noise level in the measured data, which is especially important for increasing the resolution of the patch identification method.

A set of theoretical profiles has been designed for testing the limits of the denoising and patch identification methods. The results from this test shown

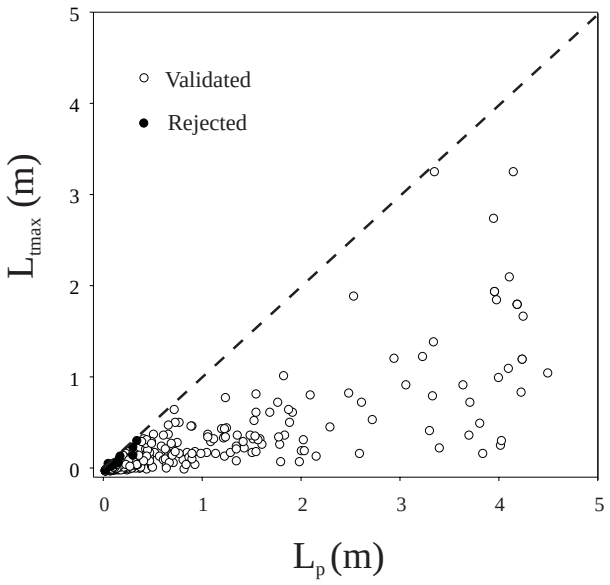


Figure 2.8: *Patch length ($L_p$) versus maximum Thorpe displacement within the patch ($L_{Tmax}$). Rejected turbulent patches according to Moum's method(1996 a,b) are indicated as solid circles.*

that it could be possible to identify small patches even in the most critical conditions of extreme low-density gradients. The final results obtained from different series of field data where validated following Moum (1996) test, obtaining a high percentage of validated patches (92.3%).

The main features of this new method are:

1. *General applicability.* The method can detect the turbulent patches in very low-density gradients. This feature is especially important in the case of turbulent boundary layer characterization, where the gradient is usually low. It is important in the studies of the interaction between turbulence and biological processes as well, as in these cases it is necessary to characterize the turbulent patches in a wide range of density gradients.

2. *Robustness.* The uncertainties derived from noise should not change significantly the final identification. The results obtained with the tests demonstrate that the method is very robust, as the global features of the detected patches do not change with different noise levels.

# Chapter 3

# Turbulent patch descriptors

In this chapter the method for describing the relevant properties of turbulent patches are presented. It was considered that the turbulent descriptors should be based mainly on length scale analysis, as this type of analysis has been widely used for describing some properties of mixing (*e.g.*, Gibson, 1980; Dillon, 1982; Caldwell, 1983; Gregg, 1987; Imberger and Ivey, 1991; Wijesekera *et al.*, 1993; Moum, 1996 a,b).

However, the interpretation of the results obtained with length scale analysis have generated some controversy and nowadays it is one of the main debatable issues in environmental turbulence. The origin of the debate resides mainly in the different views of the possible mixing scenarios.

Gibson (1980) proposed that most oceanic microstructures consist of remnants of powerful, but rare, mixing events. In this mixing scenario it is assumed that the largest turbulent dissipation rates occur at the initial stage of instability and patches persist for a time much longer than the natural timescale of the stratification (corresponding to the inverse of the buoyancy frequency). In that case, most measurements can be considered different "fossil" stages of the initial mixing process, and turbulence statistics derived from sparse microstructure observations may severely underestimate the level of mixing in the interior water masses.

Other authors (*e.g.*, Caldwell, 1983; Gregg, 1987) have argued that, in the absence of energy source, decay times associated to the turbulent patches are comparable to the natural timescale of stratification, which in most cases is the order of a few minutes. From this point of view, the problem of mixing underestimates is not severe because microstructure observations actually contain a fair sampling of energetic events.

The correct interpretation of turbulence measurements depends upon which view is taken. In the geophysical context, an understanding of the evolution of the turbulent processes is a crucial prerequisite for the proper inter-

pretation of the length scale measurements related to the turbulent patches.

Field observations of turbulence from vertically profiling, horizontally towed or moored instruments, with sensors in direct contact with the local fluid, are only "snapshots" of some particular state. The field measurement then gives only a single measurement of the turbulent patch and therefore, a direct interpretation of the evolution is not possible.

A "direct" measure of the turbulence evolution requires observation of processes in which different temporal stages are well defined. An example of this type of processes is the decay of turbulence following the removal of the external forcing. Laboratory experiments are one source of relevant information for measurements of the decay of turbulence, but direct extrapolation of the results are not possible due to the differences between laboratory and environmental observations. As noted by Gregg (1987), most of the information about the decay of stratified turbulence comes from grid wakes or turbulent jets and these measurements actually investigate spatial decay away from the source, rather than temporal decay following removal of a source. Another important difference resides in the finite dimensions of laboratory tanks, which implies that Reynolds number is small compared with geophysical values. Finally, the mechanisms properties that generate wakes and jets in the laboratory experiments may be different from those that generate turbulence in the field. In particular, the properties of the external forcing are maintained stationary in laboratory experiments, while most of the natural processes that generate turbulence are variable on time. In environmental observations, the properties of the turbulent flow may be directly related to the temporal variability of the external forcing and, therefore, the rules inferred from laboratory may be inadequate.

Few specific geophysical observations offer alternative views of the turbulence evolution. Only two examples were obtained from the revised literature. Brainerd and Gregg (1993) examined the temporal changes of the diurnal stratification, which occurs following the reversal of the surface buoyancy flux at sunrise. In this case, however, the change in surface forcing is slow, complicating the interpretation of the observed turbulence decay. Smyth *et al.* (1997) observed a faster decay process in the upper ocean of the Western Pacific following squalls events during westerly wind burst. Although the time scale for this process is much smaller than the previous observation and the decay process is much clear, the time at which the disruption starts is not well defined, and complicates the interpretation of the turbulent patch properties.

In this chapter, a new process has been reported that could be used as a geophysical example of the evolution of turbulence. This process corresponds to the temporal changes near the water surface layer during the initial stages

of a wind burst. The wind burst allows setting a reference of time in the field observations that can be used to link the results obtained with the evolution of mixing. However, the dynamics of this process is not well known and two possible mechanisms have been proposed for explaining the initial field observations of the turbulence related parameters. Although the dynamical properties of the proposed mechanisms are very different, the turbulent "signatures" in both cases may be similar. It is necessary then, to obtain detailed information of the turbulent patch properties for validating one of the proposed hypotheses.

The hypothesis contrast has been used as a framework for determining the best method of turbulent patch characterization. Several methods of description have been applied and, from the results obtained, a new method has been proposed. The method is based on the topological properties of the turbulent patches, which are integrated in a new hydrodynamic diagram.

In this chapter, the new method for characterizing turbulent patches, based on length scale analysis, is presented. The chapter has been divided in three sections:

The first section introduces the most common turbulent descriptors used in field data analysis, which have been obtained from the reviewed literature.

In the second section, some basic theoretical concepts of wind driven turbulence and related experimental results have been exposed. This short review has been done in order to explain the two different hypotheses proposed for the evolution of turbulence during the initial stages of a wind burst.

In the third section, data from Banyoles 99 campaign have been analyzed. These particular field observations correspond mainly to the evolution of mixing in a low stratified layer after a wind burst. Different methods of description, based mainly on length scale analysis, have been applied for testing the proposed mechanisms of turbulence generation. The results obtained with the new proposed method have shown the advantages of this type of description. The information obtained with this method allows inferring some dynamical properties of the observed process, and helps in understanding the mechanism that generates the turbulence.

## 3.1 Methods of patch characterization

### 3.1.1 Turbulent length scales

Some properties of mixing in a turbulent flow can be described using length scales arguments. In the previous chapter, two length scales were already defined: the vertical length of the patch $L_p$ and the maximum Thorpe dis-

placement within the patch $L_{Tmax}$.

In this section several length scales are presented. Most of the turbulent patch analysis will be based in different ratios of this type of length scales.

### Kolmogorov scale $L_K$

Turbulent flow produces a fluctuation velocity spectrum that covers the range from energy-bearing eddies to the smallest scales limited by viscosity. The scale $L_K$ was proposed by Kolmogorov (1941) as the scale in which viscous forces equals the inertial forces and represents the lower end of turbulent kinetic energy and dissipation spectra. Velocity fluctuations disappear for scales smaller than $L_K$. The scale corresponds to the inverse of the Kolmogorov wavenumber (eq. 1.21)

$$L_K = \left(\frac{\nu^3}{\varepsilon}\right)^{1/4} \tag{3.1}$$

### Batchelor scale $L_B$

The Batchelor scale is the analog to $L_K$ for scalar fields. Scalar fluctuations disappear for scales smaller than $L_B$. The Batchelor scale is computed as the inverse of the Batchelor wavenumber (eq. 1.22):

$$L_B = \left(\frac{D_\theta^2 \cdot \nu}{\varepsilon}\right)^{1/4} \tag{3.2}$$

Because molecular diffusibilities are usually smaller than $\nu$, Batchelor scale is smaller than Kolmogorov scale. Figure 3.1 shows a comparison between $L_K$ and $L_B$ at different values of $\varepsilon$.

### Ozmidov scale $L_O$

Ozmidov (1965) considered that buoyancy must limit the maximum vertical scale for overturns in turbulent stratified fluids. The Ozmidov scale $L_O$ is defined as the scale in which buoyancy forces equals inertial forces and it is computed as

$$L_O \approx \left(\frac{\varepsilon}{N^3}\right)^{1/2} \tag{3.3}$$

A typical range for the Ozmidov scale is $10^{-2}$ to 1 m (Imboden and Wüest, 1995).

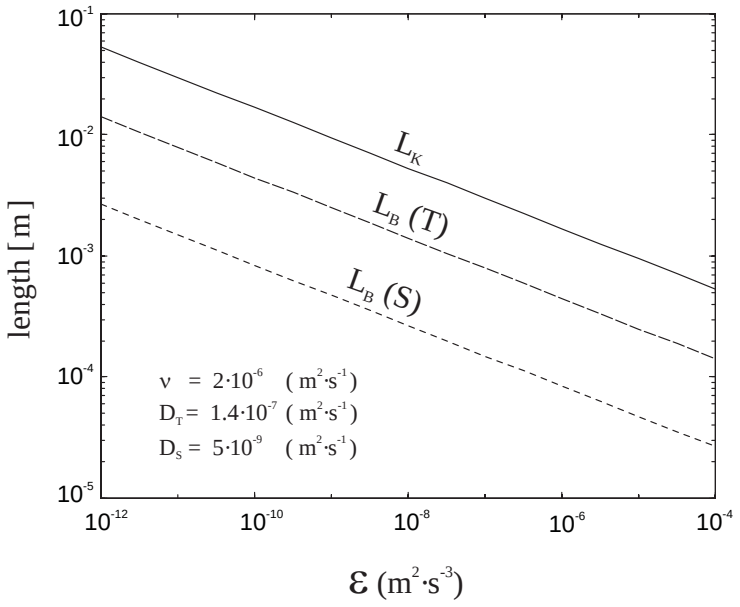


Figure 3.1: *Comparison between Kolmogorov length scale $L_K$ and Batchelor length scale $L_B$ at different values of $\varepsilon$. Batchelor scale has been computed for temperature and salinity (molecular diffusion coefficient of these scalars has been included in the graphic).*

### Corrsin scale $L_C$

Corrsin (1958) suggested that the smallest scale at which eddies are strongly deformed by the mean shear may be estimated as

$$L_C \approx \left(\frac{\varepsilon}{S^3}\right)^{1/2} \tag{3.4}$$

where $S = \frac{dU}{dz}$ is the background shear .

This length is entirely analogous to the Ozmidov scale defined above, and represents the upper limit of eddy sizes whenever background shear is more restrictive than background stratification. Smyth *et al.* (2001) simulated the evolution of mixing in uniform shear and stratification and concluded that, in the case that limits of shear and stratification were the same, the expected $L_C$ would be smaller than $L_O$ by a factor of 2.

### Ellison scale $L_E$

Ellison (1957) proposed the first length scale based on statistics from empirical measurements. The Ellison scale was defined as

$$L_E = \frac{\rho'}{\partial\overline{\rho}/\partial z} \tag{3.5}$$

and was considered the typical vertical distance traveled by fluid particles before either returning towards their equilibrium level or mixing. This scale can be directly measured from stationary or horizontally towed temperature and conductivity probes, and it is a common computed statistical length scale in laboratory experiments.

Several authors have proposed $L_E$ as a proportional scale to the largest turbulent scale as long the internal wave field remained small. Stillinger *et al.* (1983), based on a solid-body rotation model for overturns, proposed that $L_E$ multiplied by a factor of 2 could be considered a good estimate of the largest turbulent eddy size. Rohr *et al.* (1984) and Gargett *et al.*(1984) considered that $2\sqrt{2}$ would be a scaling factor more consistent with the solid-body rotation model, while Gibson (1982) proposed a factor of $2\sqrt{3}$. Itswire *et al.* (1986) suggested that the scaling factor would depend not only on the choice of the eddy model but also on the nature of the generating mechanism for the turbulence.

### Thorpe scale $L_T$

In field studies using vertical profilers, the Thorpe scale $L_T$ (Thorpe 1977; Dillon 1982) is often measured. The Thorpe scale is the root mean square of Thorpe displacements $d_T$ within a range depth of the water column. In natural stratified flows, it is virtually impossible to determine $L_E$ because internal wave contributions usually dominate $\rho'$. Itswire *et al.* (1986), computed both scales in laboratory experiments and found $L_T \approx 1.2\, L_E$. Direct numerical simulations analyzed by Itswire *et al.* (1993) show $L_T \approx 0.8\, L_E$, and many authors have assumed in their analysis the equality $L_T \approx L_E$ (Luketina and Imberger, 1989; Baumert and Peters, 2000). Since the analysis of Dillon (1982) and Stillinger *et al.* (1983), it has become commonplace to use $L_T$ as the statistical measure for the vertical size of overturning eddies (*e.g.*, Imboden and Wüest, 1995; Baumert and Peters, 2000).

### Centered displacement scale $L_c$

The centered displacement scale (Imberger and Boashash, 1986) has been proposed as a better statistical measure of the vertical size of the overturning eddies. It is also computed from the Thorpe displacements $d_T$. Each value of $d_T$ is displaced half of its value to correspond to the center of the overturn. The displaced values of $d_T$ are finally smoothed using a low pass filter.

### 3.1.2 The length scale ratio $R_{OT}$ ($L_O/L_T$)

A quantity that has often been computed is the length scale ratio $R_{OT}$ ($L_O/L_T$) for inferring some properties of the turbulent events. The lack of consensus on the properties of $R_{OT}$ is a major obstacle to the interpretation of geophysical turbulence measurements (DeSilva *et al.* 1996).

Caldwell (1983) proposed to infer dynamical properties of the process from the probability distribution of ratio $R_{OT}$. The author suggested that turbulence in the thermocline could be considered a statistical steady state process. In this scenario $L_T$ and $L_O$ should be more or less equal and the mean value of the ratio must be close to 1. There is some oceanic evidence to support that the average value of $R_{OT}$ is close to the expected value, (Dillon, 1982; Crawford, 1986; Peters, *et al.*, 1988; Imberger and Ivey, 1991; Wijesekera, *et al.*, 1993; Moum, 1996).

In those cases in which the ratio $R_{OT}$ is not constant, it has often been proposed as a convenient indicator of the age of a geophysical turbulent event (Dillon, 1982; Dillon, 1984; Gibson, 1987; Wijesekera and Dillon, 1997). However, there is no agreement about the relationship between this index and the age of the turbulent event. Gibson (1987) suggested that, for turbulent events in the ocean, $R_{OT}$ decreases in time from values much bigger than 1 to values much smaller than 1. Studies of $R_{OT}$ properties based on grid-generated turbulence support some aspects of Gibson's theory (Stillinger *et al.*, 1983). In these experiments, fluctuations are created by the flow of a stably stratified fluid through a grid. Turbulence arises from the growing wake of each individual grid element. In this case, it is clear that $\varepsilon$ and $L_O$ are maximal just behind the grid while $L_T$ will be locally minimal at the grid, consequently, $R_{OT}$ must be maximal very near the grid. Downstream, $\varepsilon$ and $L_O$ must decrease, because the source of energy driving the turbulence is not present. At some point behind the grid, $L_O$ and $L_T$ must both eventually become arbitrarily small because of molecular viscosity and diffusive smoothing. The time scale for decay of $L_O$ is determined by viscosity, while the time scale for decay of $L_T$ is determined by a scalar diffusivity that usually is less than the viscosity. Therefore, there must exist some times during the decay when $R_{OT} < 1$. This scenario has been supported by extensive observations (fig. 3.2 A).

However, other authors consider that environmental turbulence can not be always considered analogous to grid-generated turbulence. Wijesekera and Dillon (1997) have proposed an alternative scenario in which the time evolution of $R_{OT}$ proceeds in the opposite sense. Numerical simulations generated by Smyth and Moum (2000) support this hypothesis. Their results suggest that "young" turbulent events may be identified by values of $R_{OT}$

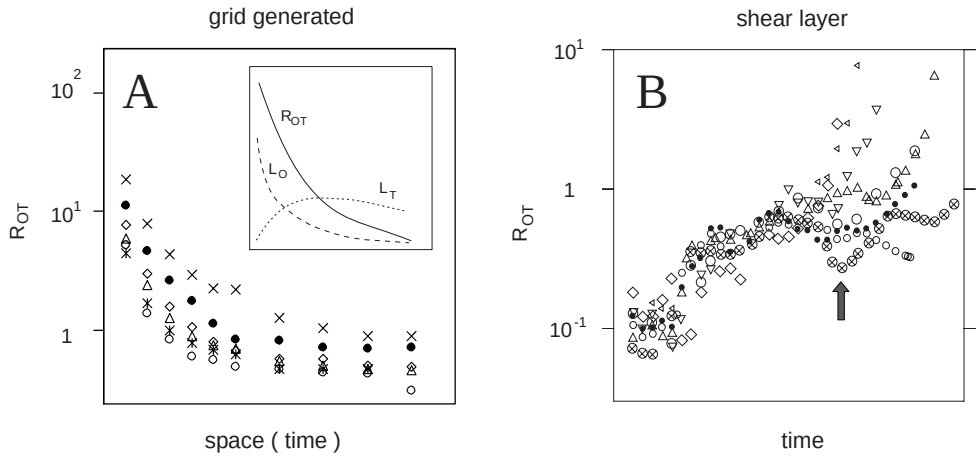


Figure 3.2: *Different scenarios of $R_{OT}$ evolution. A) Observations from grid generated turbulence. The small graphic shows the schematic evolution of $L_O$, $L_T$ and hence $R_{OT}$. Plot data corresponds to laboratory experiment (Itswire et al., 1987). B) Numerical simulations (Smyth and Moum, 2000) of shear layer induced turbulence, in which different instabilities can be developed.*

less than unity and mature events by values greater than unity. (fig. 3.2 B).

It should be noticed that both scenarios correspond to a decaying turbulent process. That means that the arrow of time that it is assumed can be associated also to an arrow of decreasing levels of dissipation. From this point of view, in Gibson's scenario high values of $R_{OT}$ would be associated to high values of $\varepsilon$ and low values of $R_{OT}$ with low values of $\varepsilon$. On the contrary, the $R_{OT}$ should be negative correlated with $\varepsilon$ in the scenario proposed by Wijesekera and Dillon (1997), and Smyth and Moum (2000). The later proposal was reflected in a particular simulation of Smyth and Moum (2000), pointed in fig. 3.2 B with an arrow, in which a secondary instability (that increased the dissipation level) generates a significant decreasing of $R_{OT}$. The correlation between levels of dissipation and values of $R_{OT}$ will be commented further in the analysis of field data.

### 3.1.3 Shannon Entropy

Some alternative descriptors of the mixing properties has been proposed based on the topological structure of the flows. The topological structure can be defined using some statistical measurements, such as entropy or fractal dimension (Sreenivasan, 1991; Wijesekera, 1996). When a flow changes from laminar to turbulent regime, these topological measurements of complexity initially increase very rapidly.

In this work, Shannon entropy $S$ was used as the topological descriptor of the turbulent patches. The Shannon entropy $S$ (Shannon, 1948) can be computed from a discrete probability distribution $p_i$ of $N$ possible states (i.e. $i = 1, 2, ...N$ )as

$$S = -\sum_{i=1}^{N} p_i \, log(p_i) \tag{3.6}$$

The probabilities $p_i$ are non-negative, additive and normalized:

$$p_i \geqslant 0$$

$$\sum_{i=1}^{N} (p_i) = 1 \tag{3.7}$$

$$p_i \cup p_j \cup p_k = p_i + p_j + p_k + ...$$

The definition of entropy characterizes the shape of the probability distribution, which was computed from the distribution of $d_T$ within the turbulent patch. The distribution depends on the number of the different intervals of displacements considered ($N$). In this work, distributions are constructed with fixed intervals of displacements ($\Delta d = 1\ cm$)and, therefore, different sized patches, have distributions with different number of intervals. It would be convenient to be able to compare different sized patches, which may arise from widely diverse initial and background conditions. It is necessary then to normalize the Shannon entropy. There are only two easily defined stable entropic states common to all patches $S = 0$, or $S = S_{max}$. If $S = 0$, the system is completely ordered which in terms of Thorpe displacement profile corresponds to a constant profile of null values. If $S = S_{max}$ the system is completely disordered. In this case the $N$ intervals of displacements have the same probability and $S_{max}$ can be computed as

$$S_{max} = -\sum_{i=1}^{N} N^{-1}\, log(N^{-1}) = log\,(N) \tag{3.8}$$

Normalizing the Shannon entropy $S_n = S/log\,(N)$ we obtained a constant range of possible values $0 < S_n \leqslant 1$.

Alternative methods, based on the discrete power spectra, have been proposed for computing Shannon entropy (Skilling and Gull, 1985; Wijesekera, 1997). These alternative methods will be commented further in the analysis of field data.

Wijesekera (1997) proposed that the changes of the topological structure within the patch provide information about the patch "age". In this work, however, it has been considered that as $S_n$ provides some information about the complexity of the structure, entropy is simply an indirect measure of the level of disorder (i.e. mixing).

### 3.1.4 Hydrodynamic diagrams

Hydrodynamic diagrams has been developed in order to evaluate the "state" of the turbulence. In a stratified fluid, energy extracted from the mean flow will be partitioned between dissipation, buoyancy flux, and internal wave motions. Hydrodynamic diagrams represents the balance between the energy fluxes, and are often presented in the form of turbulent Froude number $Fr_T$ versus turbulent Reynolds number $Re_T$ plots.

The turbulent Froude number is the ratio of inertial forcing to buoyant forcing in the energy-bearing eddies and is computed as

$$Fr_T = \frac{u'}{L \cdot N} \tag{3.9}$$

where $u'$ is the velocity scale of the energy-bearing fluctuations, $N$ the buoyancy frequency and $L$ is the overturn length scale.

The turbulent Reynolds number is the ratio of inertial forces to viscous forces in the energy-bearing eddies, and can be computed as

$$Re_T = \frac{u' \cdot L}{\nu} \tag{3.10}$$

#### Gibson diagram

Gibson (1980) has implied that $Fr_T - Re_T$ diagrams may be interpreted as an activity diagram and can be used as a tool for describing the evolution of the turbulent patches. The results obtained with the diagram applied to

different laboratory experiments and field data (Gibson 1980; 1982; 1987; 1991; 1996; 1998; 1999) has been used as empirical evidence for validating the theory of fossil turbulence.

In the fossil turbulence theory it is assumed that turbulent processes starts at the smallest possible scale and grows to the largest possible scale in which background forces limits the development of the turbulence. In the case of stratified fluids, buoyancy forces limits the development of turbulence in the vertical. When the turbulent process has reached the maximum length, the turbulent dissipation rate is equal to $\varepsilon_0$ the characteristic value at the beginning of fossilization,

$$\varepsilon_0 = 13 \cdot D \cdot C_X \cdot N^2 \tag{3.11}$$

Where $D$ is the molecular diffusivity of the scalar field, and $Cx \approx C/3$ is the streamwise Cox number, which in the case of the scalar field of temperature ($T$) is defined as

$$C = \frac{\left\langle (\partial T'/\partial z)^2 \right\rangle}{\left\langle (\partial T/\partial z)^2 \right\rangle} \tag{3.12}$$

where $\langle\rangle$ denotes vertical spatial averaging.

At the beginning of fossilization, the largest possible scale in stratified fluids can be computed as

$$L_{O_0} = \left(\frac{\varepsilon_0}{N^3}\right)^{1/2} \tag{3.13}$$

Once the fossil process has been started the dissipation rate diminishes progressively up to the complete fossilization stage, in which the dissipation rate can be computed as

$$\varepsilon_F = 30 \cdot \nu \cdot N^2 \tag{3.14}$$

Initially, the hydrodynamic diagram was based on the Cox number $C$ and the index of activity $A_T$ computed as

$$A_T = \sqrt{\frac{\varepsilon}{\varepsilon_0}} \tag{3.15}$$

$A_T$ versus $C$ diagrams had the advantage that the hydrodynamic stage of a microstructure patch could be determined using only temperature measurements. However, including the ambient stratification frequency $N$ for the patch in the diagram provided a more complete representation of the stratified hydrodynamics of the turbulent event. In subsequent diagrams

(Gibson 1986, 1996, 1998, 1999) $A_T$ was expressed in terms of the Froude number of the patch normalized by $Fr_0$ at the beginning of fossilization $Fr/Fr_0 = (\varepsilon/\varepsilon_0)^{1/3} = A_T^{2/3}$, and Cox number was replaced by the Reynolds number ratio $Re/Re_F = \varepsilon/\varepsilon_F$ (fig. 3.3).

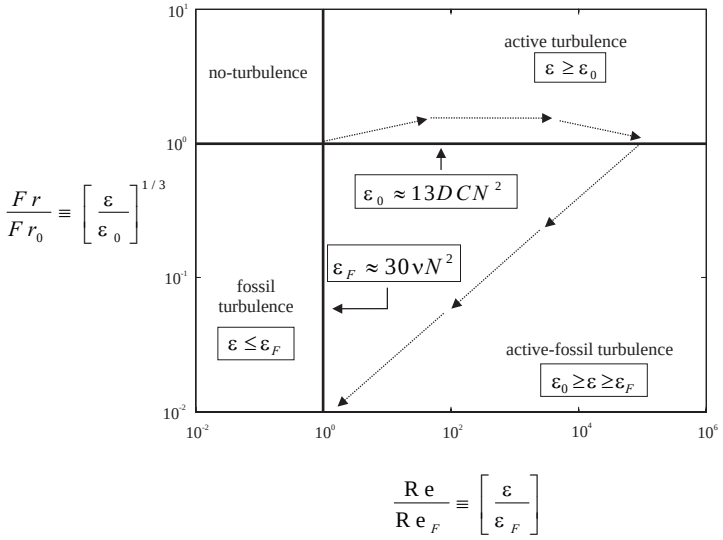


Figure 3.3: *Hydrodynamic phase diagram proposed by Gibson for classifying turbulent patches according to their hydrodynamic state in a stratified fluid. The dissipation rate $\varepsilon$ is measured for the patch, and the normalized Froude and Reynolds numbers computed from the expression $\varepsilon_0$ and $\varepsilon_F$ given on the diagram. Trajectories for the evolution of dominant oceanic turbulent events are indicated by arrows and dashed lines.*

Applying this hydrodynamic diagram over many experimental data, Gibson concluded that most of the field measurements corresponded to active-fossil stage as the values of estimated $\varepsilon$ were in the range limited by the value at the beginning of the fossilization ($\varepsilon_0$) and the value at the total fossilization ($\varepsilon_F$). Gibson (1996) argued that turbulence statistics derived from sparse microstructure observations, in which most patches are in active-fossil stage, may severely underestimate the level of mixing in the interior water masses. Supposing that the average dissipation rate for the strongly stratified upper layers of the ocean were less than $\varepsilon_F$ , as reported by Peters *et al.* (1994, 1995), a single turbulent patch of 30 m with $\varepsilon_0 = 3\,10^6\,\varepsilon_F$ would more than double the measured average in $10^8$ m of water sampled. However, at

the typical sampling speed of microstructure profilers ($\sim 1\ m\,s^{-1}$) this would require about 3 years of continuous sampling in the layer to encounter such a patch.

### Imberger and collaborators diagram

Imberger and different collaborators ( Imberger and Boashash 1986, Luketina and Imberger 1989; Ivey and Imberger ,1991) proposed a new hydrodynamic diagram considering that Gibson arguments could be valid in certain circumstances, but in general, $Fr_T - Re_T$ diagrams were really only a reflection of the status of the current energy budget of the turbulence.

The diagram was constructed considering a third adimensional number, the small-scale Froude number $Fr_\gamma$, which is the ratio of the buoyant forcing to inertial forcing at the dissipative scale of motion. The small-scale Froude number $Fr_\gamma$ can be computed substituting the strain rate of the large scale fluctuations $\Gamma = u/L_c$ to the strain rate of the small scale fluctuations $\gamma = (\varepsilon/\nu)^{1/2}$obtaining

$$Fr_\gamma = \left(\frac{\varepsilon}{\nu \cdot N^2}\right)^{1/2} \tag{3.16}$$

It should be noted that the inclusion of a third component does not affect the dimension of the hydrodynamic diagram, as there are only two independent adimensional numbers; anyone of $Fr_T$, $Re_T$ or $Fr_\gamma$ can be defined in terms of the other two.

Luketina and Imberger (1989) scaled $u'$ as $(\varepsilon\ L_T)^{1/3}$ considering that Thorpe scale is the overturn length scale. In subsequent works (Ivey and Imberger, 1991) it was considered $L_c$ a more appropriate term for the scale of the motion, scaling $u'$ as $(\varepsilon\ L_c)^{1/3}$. Substituting the last expression into eqs 3.9, 3.9 and 3.16 give

$$Fr_T = \left(\frac{L_O}{L_c}\right)^{2/3} \tag{3.17}$$

$$Re_T = \left(\frac{L_c}{L_K}\right)^{4/3} \tag{3.18}$$

$$Fr_\gamma = \left(\frac{L_O}{L_K}\right)^{2/3} \tag{3.19}$$

expressing all the adimensional values in terms of length scale ratios.

A schematic of this hydrodynamic diagram is shown in figure 3.4. In this diagram, there are three principle boundaries, namely the onset of buoyancy

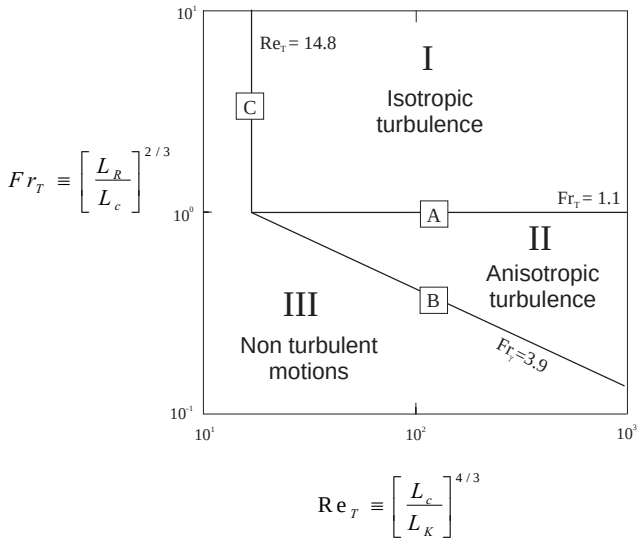


Figure 3.4: *A schematic of hydrodynamic diagram proposed by Imberger and collaborators. The diagram classifies turbulence at energy-bearing scales according to the relative effects of the buoyancy and viscosity. Boundary A represents the onset of buoyancy effects, boundary B the onset of zero buoyancy flux ($u'\rho'$ vanishing) and boundary C the smallest scale of turbulent motion. Three principal regions are indicated, namely isotropic turbulence (region I), buoyancy-affected turbulence (region II) and non-turbulent motion (region III). These are explained in the text.*

effects (anisotropy of turbulent field and length scales) (A), the onset of zero buoyancy flux ($\rho' u' = 0$) (B), and the smallest scale of turbulent motion (C).

All three boundaries can be determined from scaling arguments. The range of turbulent length scales is limited by the Ozmidov scale, where buoyancy affects the motion, and Kolmogorov scale, where viscosity suppresses the motion (Gibson, 1980). That is

$$\alpha \cdot L_O > L_c > \beta \cdot L_K \tag{3.20}$$

where $\alpha$ and $\beta$ are undetermined constants

Buoyancy will first affect the turbulence when the turbulent scale equals the maximum range value $L_c = \alpha \cdot L_O$. The critical Froude number can be

computed as

$$Fr_T^C = \left(\frac{L_O}{L_c}\right)^{2/3} = \alpha^{-2/3} \tag{3.21}$$

Similarly, viscosity will suppress the turbulent motion when $L_c = \beta \cdot L_K$. In this case, the critical Reynolds number can be expressed as

$$Re_T^C = \left(\frac{L_c}{L_K}\right)^{4/3} = \beta^{4/3} \tag{3.22}$$

Finally, the requirement for overturn motion forces a minimum allowable bandwidth for turbulence, that means

$$\alpha \cdot L_O > \beta \cdot L_K \Rightarrow Fr_\gamma^C > \left(\frac{\beta}{\alpha}\right)^{2/3} \tag{3.23}$$

Values of $\alpha$ and $\beta$ were determined in Ivey and Imberger (1991) based on laboratory results reported by Stillinger *et al.* (1983); Itswire *et al.* (1986); Rohr *et al.* (1988) and Ivey and Nokes (1989). The values of the constants determined a critical values of $Fr_T^C = 1.11$ $Re_T^C = 14.8$ and $Fr_\gamma^C = 3.9$ for boundaries A, B, and C respectively.

## 3.2 Wind driven turbulence

In this section some basic theoretical concepts of wind driven turbulence and related experimental results have been exposed. This short review has been done in order to explain the two possible mechanisms proposed for the evolution of turbulence during the initial stages of a wind burst.

### 3.2.1 Boundary layer: the law of the wall and the "wall layer"

In the absence of convection, in the upper few meters of the surface water the main source of energy is wind. Wind induces a transfer of momentum from air to surface waves and to the waters layer below. Momentum transferred from wind induces wave acceleration, wave breaking and shear flow, which in turn generates small-scale turbulence.

Measurements of the momentum transfer in the water column are more difficult to obtain than measurements in the atmospheric boundary layer. In the case of atmospheric boundary layer, the flow in the vicinity of the solid surface can be divided into three sublayers: the laminar sublayer (a term

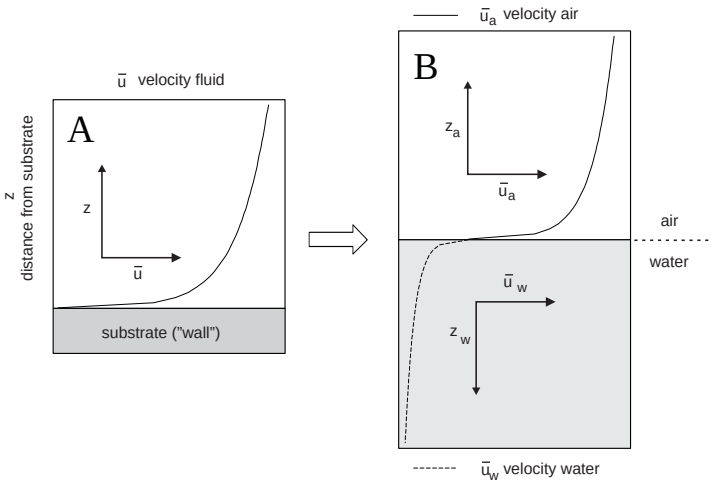


Figure 3.5: *Schematics of the boundary layer in a fluid-solid interface (A) and in the air-water interface (B). In the second case two different boundary layers are considered the atmospheric and aquatic boundary layers. The expected velocity profile has been plotted in each case. Notice that different coordinate system used in air and water (see text for details).*

'viscous sublayer' is also used), the turbulent boundary layer and the free stream. There are no sharp boundaries between each layer, so the description of the flow in each particular layer should be treated to some extent as qualitative only. In the case of air-water interface it is necessary to consider two different boundary layers, the atmospheric and aquatic boundary layers (figure 3.5).

Within the laminar sublayers, in the air-water interface, the velocity is controlled by the viscous stress $\tau$

$$\tau = \mu_i \frac{d\,u}{d\,z_i} = \rho_i\,\nu_i \frac{d\,u}{d\,z_i} \qquad i = a, w \tag{3.24}$$

where $\rho_i$ and $\nu_i$ are density and cinematic viscosity, of air or water, depending on the side of the boundary-layer under consideration.

For a very thin laminar sublayer, stress $\tau$ is approximately constant and equal to its value at the wall $\tau_0$. Then an integration of eq 3.24 gives:

$$u_i(z_i) = \frac{u_{*i}^2}{\nu_i} z_i \qquad i = a, w \tag{3.25}$$

where $u_i$ is the horizontal velocity (in air or water) and $u_{*i}$ is the friction velocity, computed as

$$u_{*i} = \sqrt{\tau_0/\rho_i} \qquad i = a, w$$

In field observations, the parameter $\tau_0$ is operationally inferred from the bulk aerodynamic flux formula:

$$\tau_0 = \rho_a \, C_D(u_{ah}) \; u_{ah}^2 \tag{3.26}$$

where $\rho_a$ is the density of air and $C_D(u_{ah})$ is the drag coefficient which depends on the wind speed $u_{ah}$ measured at given reference height $h$ above the water surface.

Far away from the viscous sublayer, the intensity and scale of the turbulent motion is determined solely by the surface stress and the depth. Dimensional reasoning leads to ( Imboden and Wüest, 1995):

$$\frac{\partial \overline{u}_i}{\partial z_i} = \frac{u_{*i}}{\kappa \; z_i} \tag{3.27}$$

where $\overline{u}_i$ is the horizontal velocity (in air or water); $z_i$ is the height in air or depth in water (defined positive downward, figure 3.5) and $\kappa$ is the von Kármán constant which is set equal to 0.41 (Csanady 1983). Integrating eq. 3.27 yields:

$$\overline{u}_i = \frac{u_{*i}}{\kappa \; z_i} \ln\left(\frac{z}{z_0}\right) \tag{3.28}$$

where $z_0$ is known as the roughness length. The turbulent layer is the region characterized by logarithmic velocity profile, and is also referred as a *wall layer*.

Based on dimensional arguments, the dissipation $\varepsilon$ scales as the cube of the turbulent velocity divided by a length scale. In the boundary layer the characteristic turbulent velocity is assumed to scale with the friction velocity $u_*$. Thus, in a constant stress layer, $\varepsilon$ decreases inversely with distance from the surface ( Imboden and Wüest, 1995):

$$\varepsilon = \frac{u_{*i}^3}{\kappa \, z_i} \tag{3.29}$$

The *law of the wall* (eq. 3.28) is the most commonly used model to predict rates of vertical momentum exchange, as well as the production and dissipation of turbulent kinetic energy. Measurements of the dissipation showing inverse proportionality with depth and logarithmic velocity profiles are regarded as evidence of the *law of the wall*.

### 3.2.2 Experimental observations of the wall layer. A review

The first measurements to estimate dissipation near wind-forced water surface were made by Stewart and Grant (1962). They reported nine estimates of $\varepsilon$ taken over depths of $0-15\ m$ in the wind speed range of $0-10\ m\,s^{-1}$, and noted a rather weak dependence on depth near surface and the expected increase of $\varepsilon$ with wave high. When the data was expressed in wall coordinates, the results scatter from about 0.4 to 7 times the expected wall layer value, $u_*^3/kz$. Because their estimate of the energy flux from the wind exceeded the depth-integrated dissipation by an order of magnitude, they concluded that almost all wave dissipation is concentrated very near the surface, essentially above the trough line.

Subsequent work (Arsenyev *et al.* 1975; Dillon *et al.* 1981; Oakey and Elliot 1982; Jones 1985; Imberger, 1985; Soloviev *et al.* 1988;Lombardo and Gregg 1989) found rates of mechanical energy dissipation that were generally consistent with the wall layer. Only few observations reported substantially higher levels of dissipation (Kitaigorodskii *et al.* 1983; Gregg 1987, Gargett 1989). Logarithmic mean current profiles in lakes (Churchill and Csanaday, 1983; Csanaday, 1984) and oceans (Ritchman *et al.*, 1987) were also been reported as additional evidence to support the model of wall layer. Although the observations referenced above tend to support the law of the wall prediction, the measurements were taken under light wind conditions or depths away from the surface.

During the last years specific studies were designed to explore the very near surface region. In these studies a variety of measurement techniques were used, including tower-based and shipborne current meters of various kinds (Agrawal *et al.* 1992; Drennan *et al.* 1996; Terray *et al.* 1996); acoustic reflections from bubbles (Thorpe 1992) and microstructure shear probes mounted both on vertical profilers (Annis and Moum 1992, 1995; Soloviev, 1999) and submarine (Osborn *et al.* 1992). The main conclusion from the measurements obtained in these experiments was the general agreement on the existence of a region adjacent to the surface (the wave affected layer) in which the dissipation rate substantially exceeds the law of the wall expected values.

The first attempt to model the wave-enhanced turbulence was done by Craig and Banner (1995), who used a level 2 $\frac{1}{2}$ turbulence closure scheme (Mellor and Yamada, 1982) to calculate the vertical structure of both currents and turbulence close to the surface. This closure scheme is highly empirical, requiring the specification of six numerical constants and the assumption of the roughness length $z_0$. The constants were determined principally from

observations of scenarios in which shear production of turbulence balances dissipation. Although no prescription was given for choosing $z_0$, by adjusting this scale over the range $0.1 - 8\ m$, Craig and Banner found order of magnitude agreement between their model and the dissipation measurements of Agrawal *et al.* (1992), Anis and Moum (1992) and Osborn *et al.* (1992).

In a posterior work, Terray *et al.* (1996) obtained measurements of dissipation close to the surface in Lake Ontario under conditions of strong wind forcing. The authors proposed a scaling for the rate of dissipation based on wind and wave parameters. One of their conclusions was that the total energy flux into the water column depends strongly of the wave age ($W_A$).

Wave age is a parameter for describing the state of the development of the waves, and is computed as the ratio (Simon, 1997):

$$W_A = c_p/U_{10} \tag{3.30}$$

Where $U_{10}$ is the standard measurement of wind velocity at 10 m from the water surface and $c_p$ is the phase velocity of the waves, computed as

$$c_p = \sqrt{g\,\lambda_p/2\pi} \tag{3.31}$$

The significant wave-length $\lambda_p$ is defined as function of the significant wave peak $f_p$

$$\lambda_p = g/\left(2\pi f_p^2\right) \tag{3.32}$$

where $f_p$ corresponds to the frequency of the maximum spectral energy density in the energy spectrum of the surface waves.

Simon (1997) also considers that wave age is a key parameter in turbulent dissipation near the surface. The author points out that one of the complications that generate deviations from the law of the wall is the time needed for waves to develop. The time (and the energy) used for increasing the wave field produces a disequilibrium between the mean wind and the current stress under changing wind conditions.

### 3.2.3 Dynamic response to wind changes

In the previous review, it has been shown the high complexity dynamics of the wind driven turbulence.

A field example of the complex dynamics of the surface boundary layer can be observed in the data reported by Stips *et al.* (1996) obtained in a survey in Lago Maggiore (fig.3.6). Three main wind events where reported during the microstructure field measurements, in which there was a disequilibrium

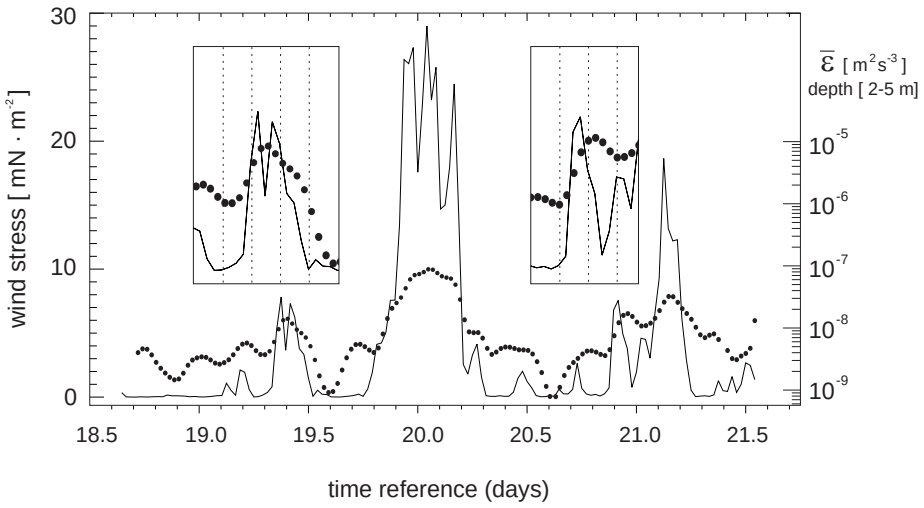


Figure 3.6: *Wind stress measured at December 18 to 21 1995 in Lake Maggiore (data from Stips et al. 1996). Three periods of increased local wind events were reported. The disequilibrium between wind flux and turbulent dissipation rates (dots) can be observed.*

between wind flux and turbulent dissipation. The authors reported a delay between the wind peak and the increase of the dissipation rate near the surface was $\sim<$ 30 minutes.

Two possible mechanisms, from the qualitative point of view, were proposed to explain this delay. The first hypothesis considered that the dynamics of the turbulence in the near surface layer responds slowly to the wind changes. The system inertia needs certain time of input energy before mixing starts effectively.

However, some preliminary results obtained from microprofiler measurements (data not shown) suggested that the levels of shear increased significantly just after small increments of wind energy. In this case, it could not be reasonable to expect a great delay between the wind peak and the maximum of turbulent dissipation. An alternative hypothesis for the observed delay required a more complex mechanism. In this alternative scenario, the higher wind energy input induces a rapid increase of mixing during the initial interval. The wind stress induced significant changes on the water surface, and the surface wave field started to develop. As it was mentioned in the previous section, Terray (1996) reported that wave development strongly modifies

the energy flux into the water column. It is assumed in this case, that wave development represents the main sink of wind energy flux during this period. The energy available for the mixing into the water column is reduced considerably during the growing period of the surface wave field, and there is the consequent decrease of mixing activity. Once the waves have reached a certain stage of development, wind stress and wave breaking provides energy to the water column which yields in a increase of turbulent mixing.

Figure 3.7 shows a diagram of the proposed mechanisms, namely "slow response dynamics" hypothesis and "fast response dynamics" hypothesis.

In the first case, any measurement associated to mixing should respond with similar pattern that is proposed on fig 3.7A. Any descriptor associated to turbulence level must increase (more or less slowly) up to at certain point in which there is a significant increase of turbulence levels.

In the second case, the evolution of the measured mixing parameter must be more complex and the temporal pattern should be similar to the proposed on fig 3.7B. During the raising period of wind, that it is referred as period II on fig. 3.7, the turbulence level should increase significantly. Period III would represent the interval in which the changes on the water surface represents the main sink of the wind energy flux, and the energy flux must decrease dramatically in the water column. Consequently, the turbulence level should decrease during this period and, depending of the energy balance, it could reached levels below the reference of turbulence level measured at the period I. Period IV would represent the interval in which the waves had reached the "full development". At this time waves could not accumulate more energy and they would dissipate the energy by wave breaking. Wave breaking would enhance the turbulent dissipation rate under the water surface, and the final increase of turbulence level could be observed.

Although the dynamics proposed in both hypotheses are very different, the temporal pattern of the parameters associated to mixing could be similar in many cases. Two main features, from any descriptor related to the level of turbulence, may validate the hypothesis of "fast response dynamics": 1) a significant peak during the rising wind velocity -period II- and 2) the turbulence levels recorded during period III are below those recorded during period I. However, the levels recorded during period III depends on the fraction of energy flux that feeds the wave field, and even in the case that the hypothesis was valid, it may be possible to record higher levels of turbulence during period III than those recorded during period I. The key difference on the temporal pattern, then, would be the peak associated to period II.

In a general case, validating (or rejecting) the hypothesis of "fast response dynamics" would require a method of description that was able to assure that there is (or not) a significant peak during the transitional stage. This is not

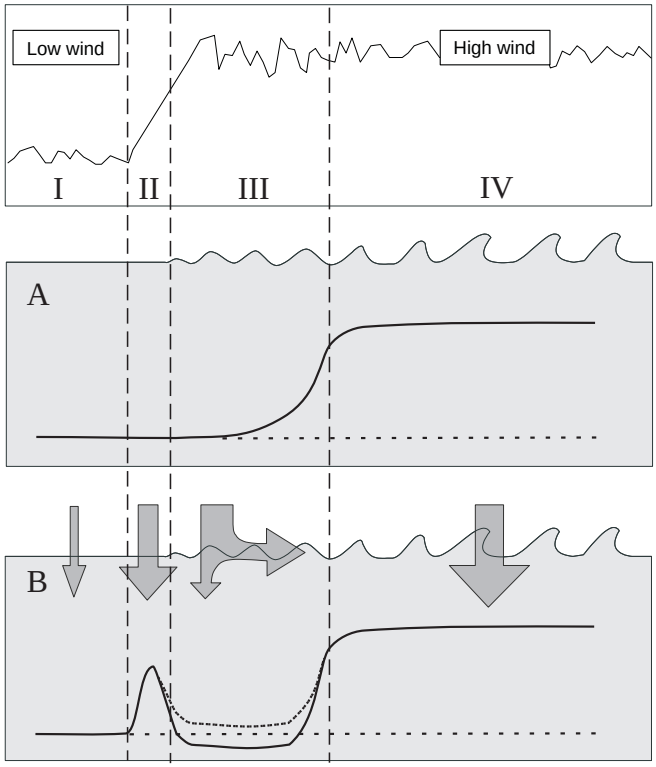


Figure 3.7: *Schematic views of the disequilibrium between the mean wind and the current stress under changing wind conditions. (A-B) The diagrams represent any hypothetical descriptor of the level of turbulence. A) Evolution of the turbulence descriptor following the "Slow response dynamics" hypothesis B) Evolution of the turbulence descriptor following the "Fast response dynamics" hypothesis. In this case, the evolution is more complex (see text)*

a simple task, taking into account the interval of sampling between different profiles.

A definitive description of the near-surface dynamic processes was beyond the scope of the present analysis. However, the hypotheses contrast can be used as a framework for determining the best method of turbulent patch characterization. If there is any method of description that is able to discriminate between both hypotheses, this method may provide the relevant information for describing a wide range of processes, some of them, with less complex dynamics. With this in mind, field data corresponding to the initial period of a wind burst was analyzed. The results are presented in the next section.

## 3.3 Field experiment

The data obtained in Lake Banyoles during July 13 in 1999 was used for the detailed length scale analysis.

At this time of the year, there is a well defined thermocline, and the water column can be considered a two layer system. The length scale analysis was focused on the epilimnion at the range of 2-5 m depth, because is the layer directly influenced by surface wind stress. (fig 3.8).

### 3.3.1 Meteorological conditions

During the field campaign, a high temporal resolution of meteorological data was measured, obtaining 1 sample of air temperature and wind velocity every minute. Figure 3.9 shows the temporal series of the meteorological data. The rectangles indicate the two periods in which microstructure profiles were recorded. Two different regimes were observed during the periods of microstructure measurements. The most interesting was observed during the period II, with a characteristic wind burst originated from the summer sea breeze. Most of the length analysis was focused in this period because, it corresponded to the initial period of a wind burst. Data from period I has been included in some general analysis in order to obtain a more robust statistical results.

### 3.3.2 Evolution of the turbulent dissipation rate

The near surface response to the wind burst can be evaluated by analyzing the evolution of the turbulent dissipation rate. Figure 3.10 shows the computed values of $\varepsilon$ between the range depth considered in the analysis of the

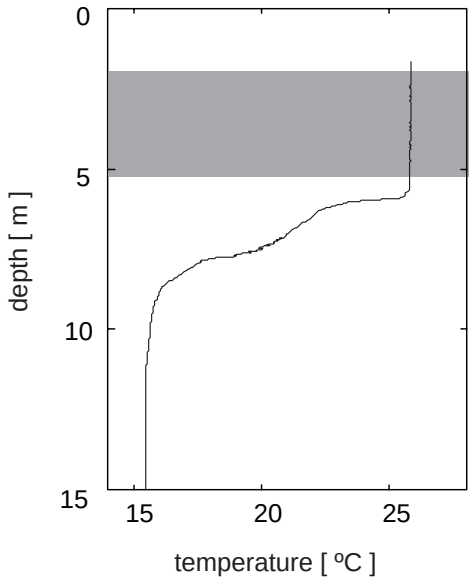


Figure 3.8: *Characteristic temperature profile recorded during the field campaign. A pronounced thermocline below 5 m was observed. The gray band indicates the depth range considered for the microstructure analysis.*

response to the wind burst. The temporal changes of $\varepsilon$ are according with the experimental results exposed in the previous section.

Just after the first significant transition of wind velocity (WT1) the turbulent dissipation rate drops dramatically. Although there was not any sensor for characterizing the surface wave field, it was observed during the field measurements a significant development of surface waves during this initial period.

The highest wind velocities ($\sim 8\ m\,s^{-1}$) were recorded between 13:50 and 14:40 solar time. After this interval the second significant transition of wind velocity (WT2) was recorded. In this transition the wind velocity decreased down to $\sim 5\ m\,s^{-1}$ and the highest values of $\varepsilon$ were measured. The increase of $\varepsilon$ could be explained by the release of energy stored in the wave field (the surface waves were progressively disappearing once the wind velocity started to decrease). Bourassa (2000) also suggested that the ratio between the shear-related stress in the aqueous boundary layer and the wind stress could increase up to a 100% (compared with the 20% observed in the near local wind equilibrium) for decaying wave fields.

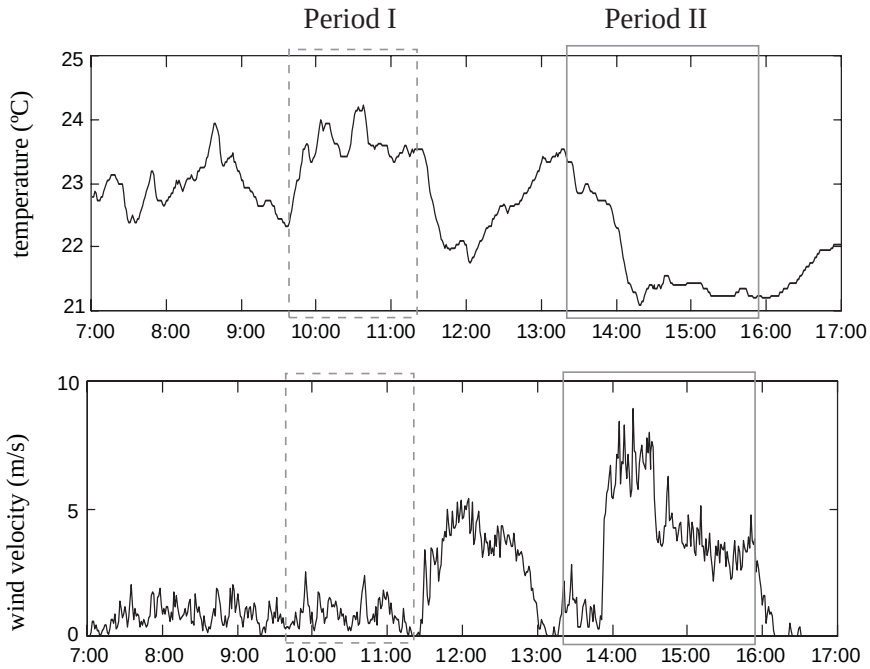


Figure 3.9: *Meteorological data measured during the field camping. The rectangles indicate the two periods in which microstructure profiles were recorded.*

However, care should be taken in characterizing the evolution of turbulent dissipation exclusively from the dissipation contour plot. Agrawal *et al.* (1992) measured the time-dependent dissipation estimates based on intervals of 13 s, and show important variations (by a factor of 10) over this very short interval of time. In this survey, the time interval between profiles measured were 5 min approximately. That means that it was possible that important information related to temporal changes on dissipation were not measured. Therefore, some of the properties of the temporal changes on $\varepsilon$, inferred from the contour plot, may be simple artifacts of missing data interpolations.

In order to increase the temporal resolution of the dissipation estimates, a method for inferring values of turbulent dissipation, was developed. The method is based on the wind records. The first step was computing the turbulent kinetic energy balance, following the idea proposed by Wüest *et al.* (2000).

The turbulent kinetic energy input of reference was computed from wind

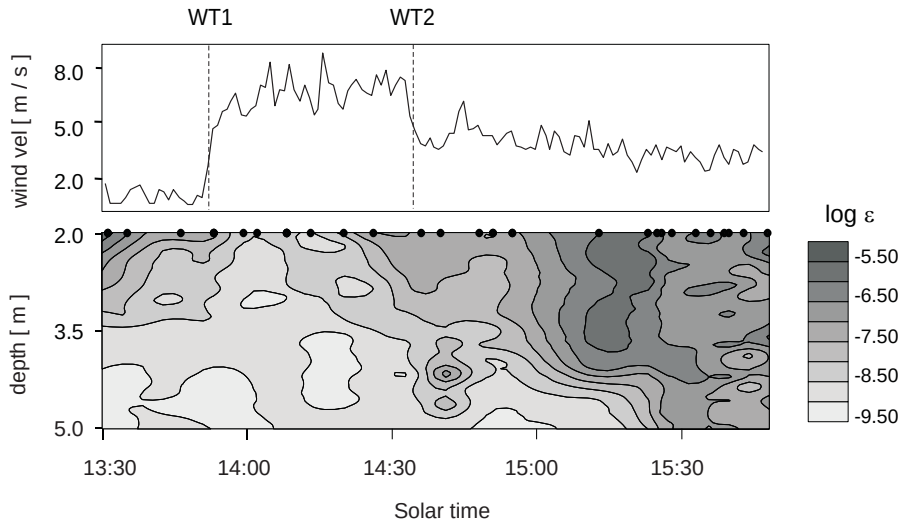


Figure 3.10: *(Top) Detail of the wind velocity during the period II. The most significant changes of wind velocity (WT1 and WT2) are indicated with dashed lines. (Down) Computed values of the turbulent dissipation rate in the range depth of microstructure analysis (2-5 m). The temporal reference of the different profiles is indicated with black dots*

turbulent energy flux 10 m above the lake surface, following (Lombardo and Gregg, 1989) and Wüest *et al.* (2000)

$$P_{10} = \rho_a \, C_{10} \, W_{10}^3 \tag{3.33}$$

The integrated turbulent dissipation within the layer of interest (2-5 m) was computed as

$$P_{S_{25}} = \int_2^5 \varepsilon \, (z) \;\; dz \tag{3.34}$$

and the turbulent kinetic energy balance ($TKEB_{25}$) as the quotient between both values $P_{S_{25}}/P_{10}$.

Figure 3.11 shows a logarithmic plot of the $TKEB_{25}$ versus the wind $W_{10}$, measured during each profile.

It can be observed a significant decrease of $TKEB_{25}$ once the wind speed reaches a threshold value. The transfer function between $TKEB_{25}$ and $W_{10}$

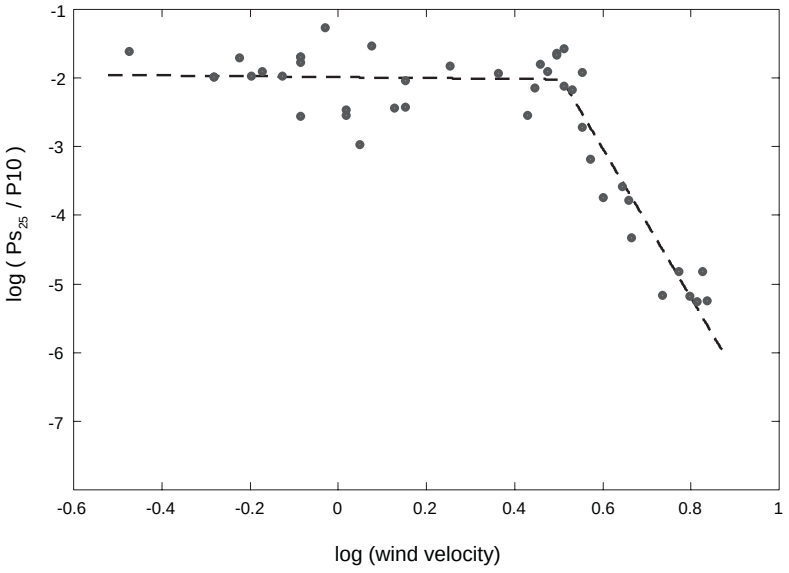


Figure 3.11: *Logarithmic plot of the* $TKEB_{25}$ ($P_{S_{25}}/P_{10}$) *versus* $W_{10}$. *The result of bilinear regression fitting is represented as dotted line.*

has been computed using a bilinear regression

$$\begin{cases} TKEB_{25} = A_0\ (W_{10})^{A_1} & W_{10} < W_{thr} \\ TKEB_{25} = B_0\ (W_{10})^{B_1} & W_{10} > W_{thr} \end{cases} \tag{3.35}$$

obtaining the following result (bootstrap N=1000, interval of confidence 90%): $A_0$= 0.0103 [0.0077 0.0137]; $A_1$ = -0.0635 [-0.3587 0.2498]; $B_0$ = 3127.5 [2034.2 4020.7]; $B_1$ = -10.8773 [-12.2146 -9.5705] and the wind threshold $W_{thr}$ = 3.21 [3.04 3.36] $m\,s^{-1}$.

The integrated turbulent dissipation $P_{S_{25}}$ can be computed as the product between $TKEB_{25}$ and $P_{10}$. As both parameters can be estimated exclusively from wind data (eq. 3.33 and 3.35), and $W_{10}$ has been measured each minute, it is possible to reconstruct the evolution of $P_{S_{25}}$ with this temporal resolution.

Figure 3.12 shows the series of $P_{S_{25}}$ reconstructed following this method. The three most energetic values of $P_{S_{25}}$ (with values of 0.8 $mW\,m^{-2}$, approximately) were clearly underestimated, but there was a general agreement between the interpolated pattern and the measured data.

The reconstructed profile suggests a transitional dissipation peak during WT1, which it could validate the hypothesis of "fast response dynamics".

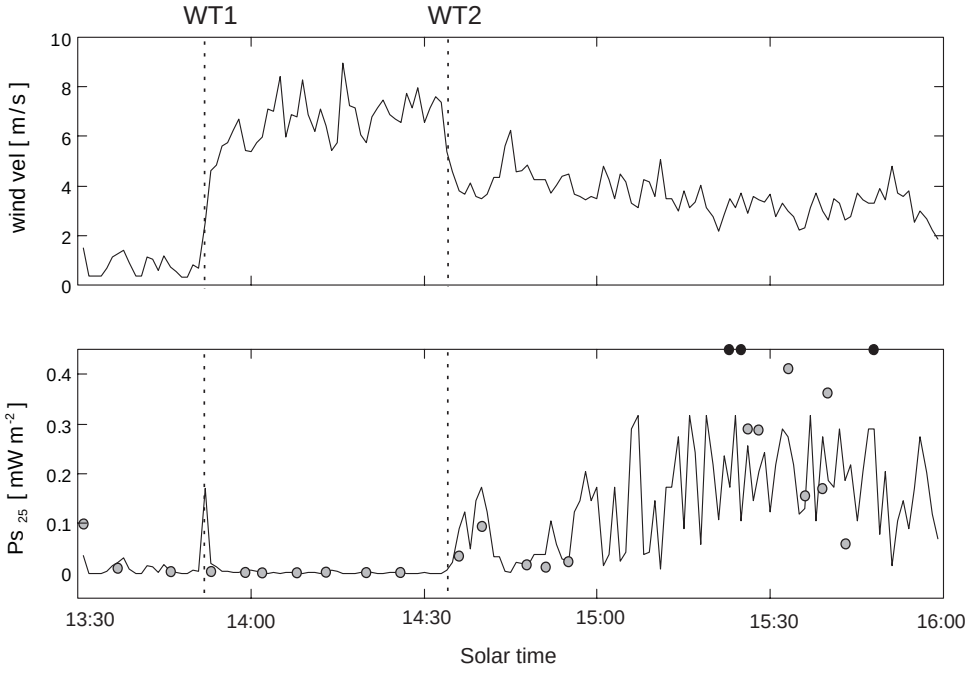


Figure 3.12: *Series of $P_{S_{25}}$ reconstructed following the method of turbulent kinetic energy balance.*

However, measured data can be explained also with the alternative hypothesis of "slow response dynamics".

Although it was not possible to contrast the proposed hypotheses with this method, it opens new possibilities of data interpolation. Length scale analysis was required to obtain more information of the turbulent process in order to discard one of the proposed mechanisms.

In further analysis wind transitions $WT1$ and $WT2$ were taken as a reference of potential changes.

## 3.4 Length scale analysis

Length scale analysis was developed for each turbulent patch. The first step was then the turbulent patch identification. This process was developed following the method explained in the previous chapter. The turbulent patches were characterized by computing their vertical length $L_p$, the maximum Thorpe displacement throughout the patch $L_{Tmax}$, the Thorpe scale

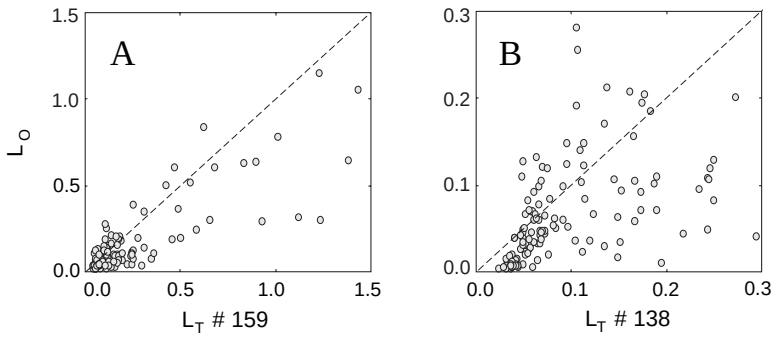


Figure 3.13: *(A) Thorpe scale $L_T$ plotted versus Ozmidov scale $L_O$. (B) A detail plot restricting the $L_T$ range from 0 to 0.3, where most of the patches were observed (138 from a total of 159). In this second plot the lack of correlation between this parameters is evident.*

$L_T$, the normalized Shannon entropy $S_n$, the mean dissipation rate and the background buoyancy frequency, which allowed to compute the associate Ozmidov scale $L_O$.

### 3.4.1 Analysis based on the length scale ratio $R_{OT}$

Several properties of $R_{OT}$ were analyzed, trying to compare with the interpretations proposed by different authors on section 3.1.2

The ratio $R_{OT}$ computed from the turbulent patches was not constant (figure 3.13) and its variability could be described by a lognormal probability distribution (figure 3.14), which is according to the result obtained by Wijesekera *et al.* (1993). As it could be expected, the high variability of the ratio indicated the non-stationarity of the turbulent process.

A time series corresponding to the evolution of $L_T$, $L_O$ and $R_{OT}$ during the wind burst were computed (figure 3.15).

As it could be expected, there was general trend for $L_T$ and $L_O$ to increase after the second transition of the wind, where the highest values of dissipation rate were recorded. The values of $R_{OT}$ show a considerable scattering. Part of this scatter may be due to the fact that both $L_O$ and $L_T$ become very small during the transition WT1-WT2, so that their ratio is difficult to compute accurately. Nevertheless, there was a general trend on the evolution of length scale ratio $R_{OT}$ to decrease when the highest measurements of dissipation rates.

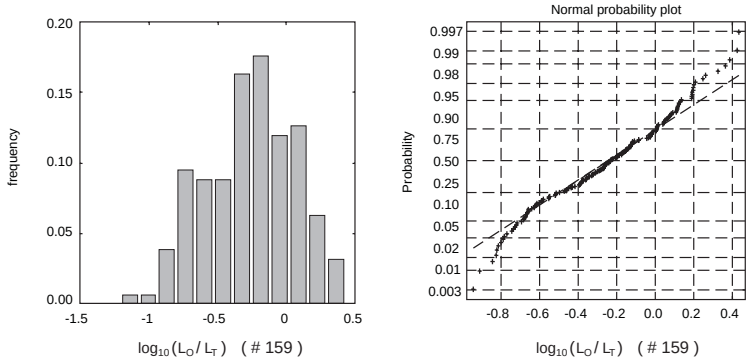


Figure 3.14: *(Right). Histogram of the logarithm of the ratio $L_O/L_T$. (Left) The linear shape of the normal probability plot computed from $log_{10}(L_O/L_T)$ indicates that the length scale ratio can be adjusted by a lognormal probability.*

The evolution of $R_{OT}$ can be compared with the hypotheses proposed in section 3.1.2. However, empirical measurements or numerical simulations for validating those hypotheses were developed in a decaying turbulent process while, in the present data, the dissipation rate evolved from low values to high values. Taking into account this important difference, the data should be analyzed comparing the changes of $R_{OT}$ with the changes on $\varepsilon$, rather than time. In this case the final result seemed to be more agree with the scenario proposed by Wijesekera and Dillon (1997) and Smyth and Moum (2000), as the smallest values of the ratio $R_{OT}$ were associated with the highest measurements of dissipation rates.

Although this result provides relevant information about the mixing process, it is not possible to reject any of the hypotheses of the dynamics during the first interval of the wind burst. It was necessary to develop alternative descriptions for this purpose.

### 3.4.2 Patch size and $d_T$ distributions

The objective of this analysis was the establishment of a potential relationship between patch size and the distribution of $d_T$ within the patches.

In order to obtain a robust statistical result, patches were grouped in interval classes of 40 cm, in the range of $[0.0 - 4.4]$ m. Different percentiles of $d_T$ were computed for each interval of $L_p$ sizes. The percentile of 50 was considered as the central value of the distribution, and the dispersion was obtained by computing the percentiles of 75, 95 and 100. Notice that

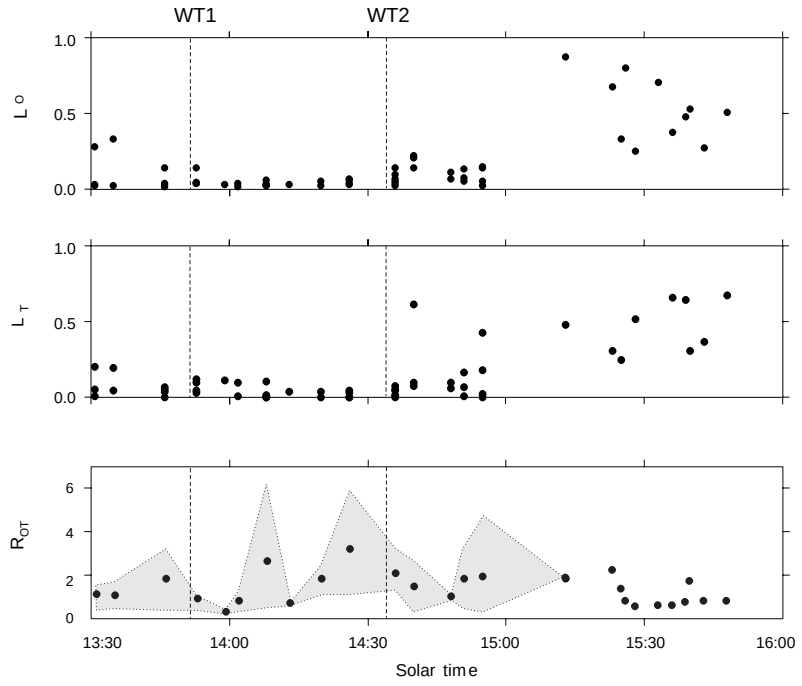


Figure 3.15: *Evolution of Torpe scale $L_T$, Ozmidov scale $L_O$ and the length scale ratio $R_{OT}$ during the period II of microstructure measurements.*

percentile 100 correspond to the maximum $L_{Tmax}$ of each interval classes. The kurtosis for each distribution was also computed as a complementary descriptor.

Figure 3.16 shows the characteristics of the distributions associated to the different patch sizes for the two periods of measurements. Three general trends can be summarized for the distributions of $d_T$ within the patches

1. The distributions are leptokurtic and the central value is 0

2. Maximum values are limited by the patch size $L_p$ (as it was expected) but only in the maximum dispersion distributions $L_{Tmax}$ is close to $L_p$.

3. The relative displacements within the patch are not correlated variables. The lack of correlation is specially remarkable in the data from period one, where the maximum displacements were found in the patch size interval $[2.4 - 2.8]$ m while the maximum $L_p$ was obtained in the $[4.0 - 4.4]$ m interval.

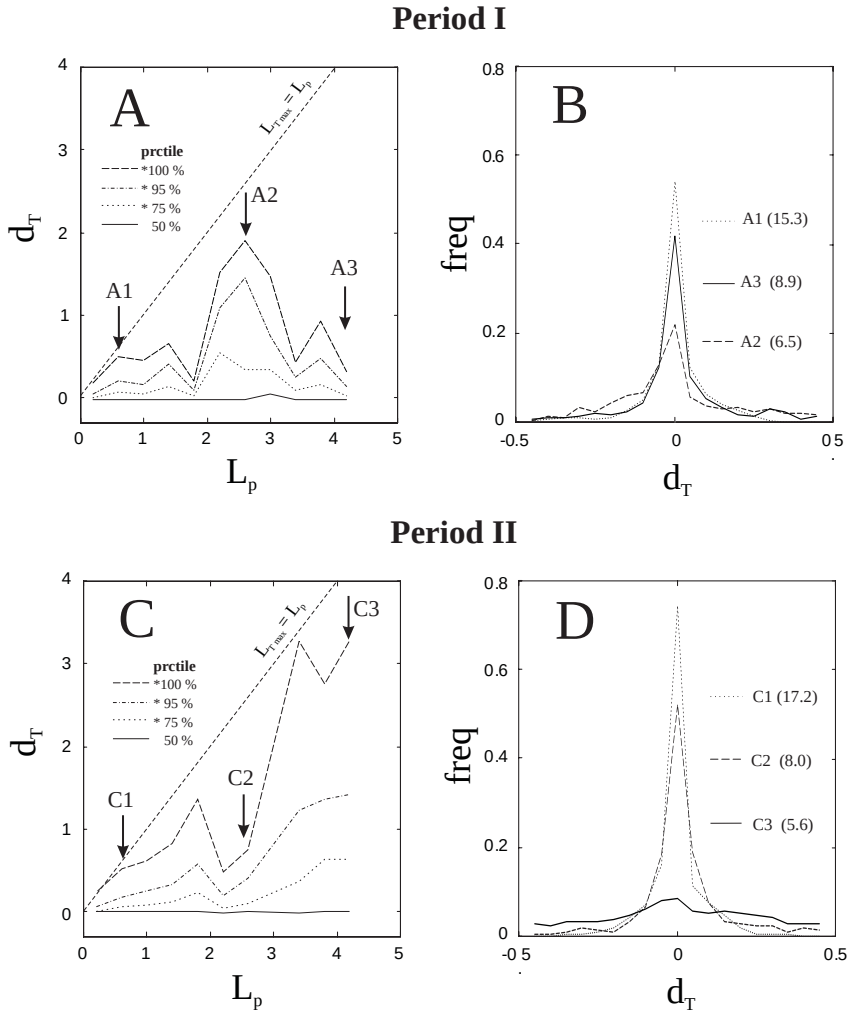


Figure 3.16: *Thorpe displacement distributions versus patch size. (A) $d_T$ distributions corresponding to the period I. Dotted diagonal line represents the threshold of maximum displacement $L_{Tmax} = L_p$. (B) Detail of the distributions around the central value in three particular Lp ranges (A1, A2, AC3; pointed with arrows in plot A). The value of the kurtosis is also included in each case. (C) Distributions corresponding to the period II. (D) Detail of the distributions around the central value for three particular Lp ranges C1, C2, C3.*

The lack of correlation between the patch size and the properties of the displacement distribution pointed out that $L_p$ and descriptors computed from $d_T$ distributions are independent sources of information, and could be combined to improve the turbulent patch characterization.

### 3.4.3 Patch size and Shannon entropy

The relationship between patch size and the properties of the $d_T$ distributions were analyzed more particularly for each patch, considering the evolution of mixing after the wind burst. The analysis was focused then on the period II, and the normalized Shannon entropy $S_n$ was computed as a synthetic parameter of the $d_T$ distribution properties of the turbulent patches detected in each cast. As mentioned in the previous section, $S_n$ was computed from $d_T$ distributions and it has been considered an indicator of the level of mixing.

Figure 3.17 shows the temporal changes of patch size and $S_n$ computed for each microstructure profile. There was not a clear pattern in patch sizes, as an example, big patches could be found along the period, independently of the wind velocity regime. However, during the interval of the maximum dissipation rates all the patches detected achieved the maximum $L_p$, as it could be expected.

$\langle S_n \rangle$ presented a much clearer temporal pattern. Two main features according to the hypothesis of "fast response dynamics" was observed on the evolution of $\langle S_n \rangle$: 1) There was a significant peak of $\langle S_n \rangle$ just after the rising period of the wind burst, which could reflect the fast enhanced mixing process proposed in this hypothesis. 2) The values of $\langle S_n \rangle$ decreased dramatically after the peak and reached even lower values than those observed before the wind burst. These very low values of $\langle S_n \rangle$ could not be explained with the scenario proposed in the hypothesis of "low response".

#### Shannon entropy. Computing considerations

The previous analysis has shown that normalized Shannon entropy provides relevant information about the dynamics of the observed phenomenon. As it has mentioned in section 3.1.3there are alternative methods of computing this value that are based on the power spectra coefficients. In these methods the probability is computed as

$$p_i = \frac{\psi_i}{\sum_{i=1}^{M} \psi_i} \tag{3.36}$$

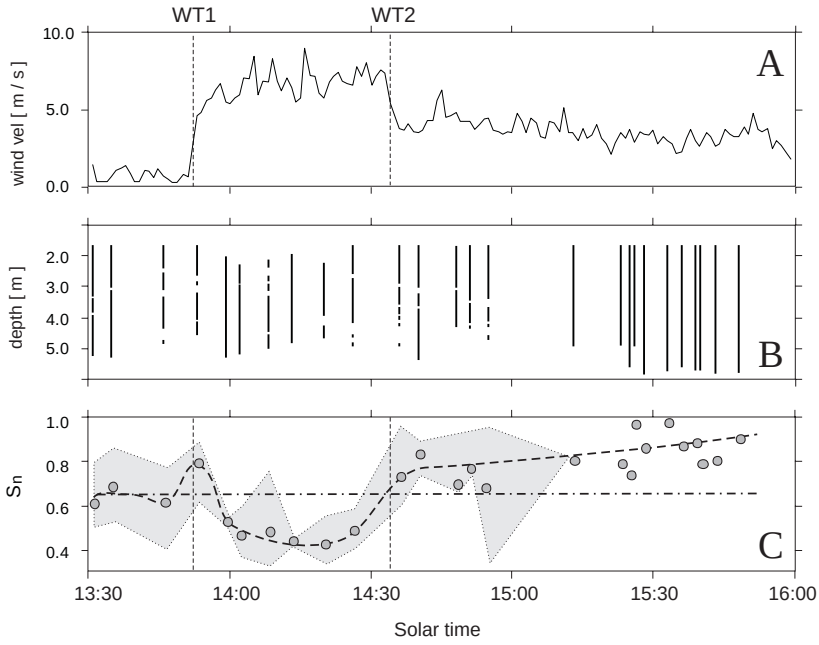


Figure 3.17: *(A) Detail of the wind velocity during the period II with the most significant changes of wind velocity (WT1 and WT2). (B) Turbulent patch detected, represented by a vertical bar. (C) Normalized Shannon $S_n$ entropy computed from the patches detected in each profile.*

where $\psi_i$ is the $i^{th}$ spectral estimate. In this case Shannon entropy characterizes the shape of a spectrum, and the maximum entropy is computed as

$$S_{\max} = \log(M) \tag{3.37}$$

where $M$ corresponds to the total number of spectral estimates. The values of normalized Shannon entropy derived from the probability distributions or the power spectra may be in some cases different, because there are different physical implication on the properties of spectra or probability distributions. The spectrum shape of a turbulent patch having small displacements distributed randomly (resembling white noise) would be flat, and the normalized entropy computed from such spectrum will be large. On the contrary, the probability distribution of displacements will be restricted on a narrow range

of displacements, and the normalized entropy computed from the probability distributions will be small. If the same type of displacements were measured in a patch much larger in vertical size ($L_p$), the value of the normalized entropy derived from the spectrum would be similar to the previous patch, while the normalized entropy derived from probability distribution would decrease significantly.

These differences can be explained by the different implications of entropy changes. Spectra derived entropy increases when increase the maximum frequency of perturbations (displacements). The distribution derived entropy increases when increase the range of potential displacements (i. e. when increase the relative displacements within the patch).

#### $L_p$ and $S_n$ as turbulent descriptors

The results obtained in section 3.4.2shows that the patch size and the relative displacements within the patch were not correlated variables, and then, they can be used as complementary sources of information. The turbulent patches may be characterized by these variables: $L_p$ provides the vertical range in which the turbulence is active and $S_n$ provides information about the intensity of mixing within the patch.

### 3.4.4 The length scales $L_T$ and $L_{Tmax}$

The Thorpe scale $L_T$ and the maximum displacement within the patch, $L_{Tmax}$, are alternative length scales that can be used for characterizing turbulent patches. Dillon (1984) considered that $L_T$ was a better descriptor because the root mean square of the displacements was a more statistically stable representation of the patch properties.

In a previous analysis, it has been shown that $d_T$ distributions are usually characterized by a high values of kurtosis, which it means that major part of the $d_T$ values are small, and only a few percentage of the displacements are large. When computing the rms of a set of $d_T$ corresponding to this type of distributions (i.e. $L_T$) , the final result depends mainly on the largest values (Stansfield *et al.*, 2001). Consequently, it must exist a correlation between $L_{Tmax}$ and $L_T$.

Figure 3.18 shows the high linear correlation between $L_{Tmax}$ and $L_T$ computed from the field data. The ratio $L_{Tmax}/L_T$ is constant and approximately equal to 3. Moum (1996) obtained a similar result computing some length scale statistics in the oceanic thermocline. In this work the author obtained a ratio $L_{Tmax}/L_T \approx 3.3$. Itsweire *et al.* (1993) computing the same ratio from laboratory experiments obtained a final value of $L_{Tmax}/L_T \approx 2.4$. Fi-

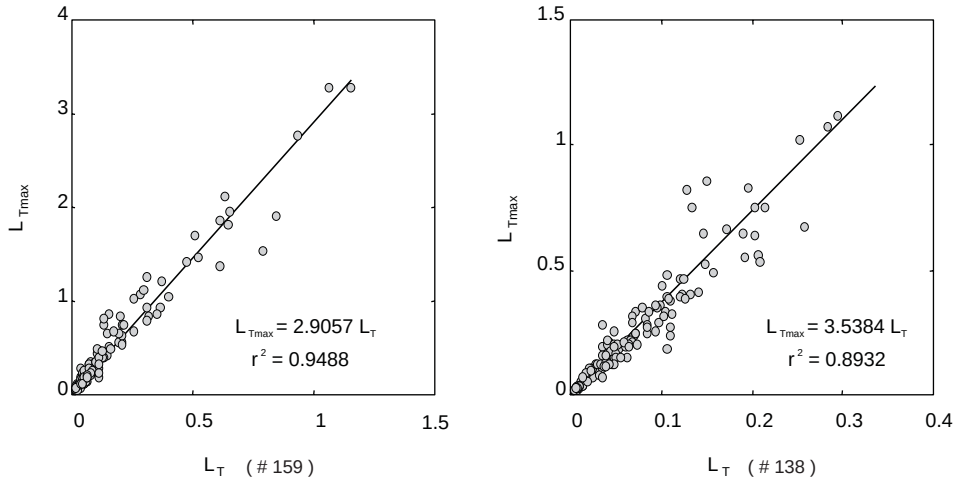


Figure 3.18: *Linear correlation between $L_{Tmax}$ and $L_T$ computed from the field data obtained in Banyoles 99 campaign. (A) Linear correlation considering all the data. (B) The same analysis was done focused in a smaller range of $L_T$, obtaining similar results.*

nally, in the numerical simulations carried out by Smyth and Moum (2000) the central value for the ratio $L_{Tmax}/L_T$ was nearly 3.

This results, obtained in a wide range of field and laboratory situations, seems to indicate that there is a general scaling in the ratio $L_{Tmax}/L_T$. The nearly constant ratio $L_{Tmax}/L_T$ suggests that the shape of $d_T$ distributions do not change significantly. $L_T$ is not a more robust statistical value of $L_{Tmax}$ as it depends mainly of this single value, and then, the relative errors from both scales are approximately equal.

### 3.4.5 The scale ratio $L_{Tmax}/L_p$ and the entropy $S_n$

The ratio $L_{Tmax}/L_p$ can be considered an alternative descriptor of the relative displacements within the patch. In the previous section it was suggested that the shape of distribution $d_T$ distributions do not change significantly, if this assumption was true, the ratio $L_{Tmax}/L_p$ should be highly correlated with $S_n$. Figure 3.19 shows that both parameters provide analog information. The ratio $L_{Tmax}/L_p$ can be then considered an alternative descriptor of the mixing level within the patch.

In this work, it has been considered that $L_{Tmax}/L_p$ is more useful descriptor than $S_n$ as it provides a direct information of the maximum relative

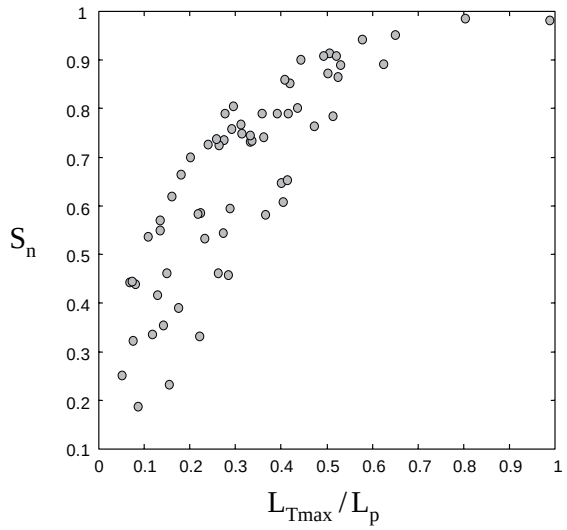


Figure 3.19: *Normalized Shannon entropy $S_n$ plotted versus the ratio $L_{Tmax}/L_p$. The correlation between this variables allows to use the ratio $L_{Tmax}/L_p$ as an indicator of the level of mixing whitin the patches.*

displacement within the patch.

## 3.5 Proposal of new hydrodynamic diagram

From the results obtained in the previous analysis, a new hydrodynamic diagram was proposed. The diagram was constructed in the form of patch size $L_p$ versus the ratio $L_{Tmax}/L_p$ plot.

Patch size $L_{Tmax}/L_p$ provides information about the range depth in which the turbulence has been developed and the ratio $L_{Tmax}/L_p$ is an estimator of the mixing level within the patch.

The data corresponding to the period II was used for illustrating how the different stages of turbulent activity are plotted in the diagram. The data was grouped in four different intervals associated to different stages of turbulent activity. For each interval, turbulent patches were plotted in a diagram of $L_p$ versus $L_{Tmax}/L_p$. Additionally, $S_n$ was coded for each patch in order to have extra information of the mixing level.

Figure 3.20 shows the four different plots in which it is possible to appreciate significant differences between them. The first interval corresponds to the patches detected previously to the wind burst. In this interval, patch size

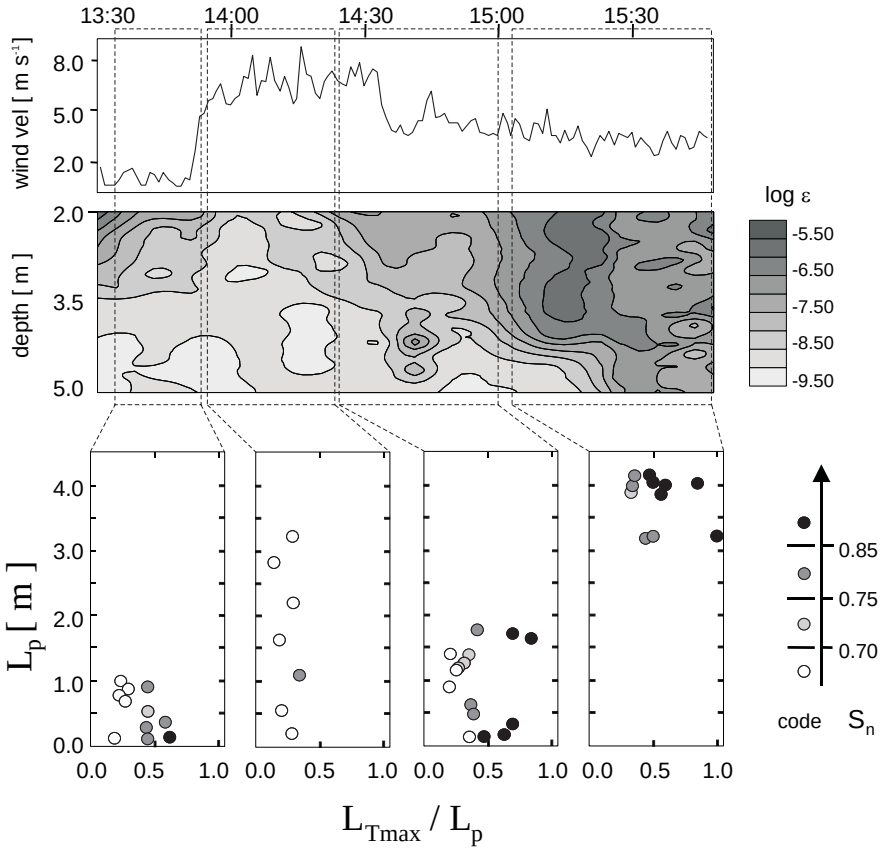


Figure 3.20: *Diagram of Lp versus $L_{Tmax}/L_p$ applied for the four intervals with different turbulent activity during the period II. A color code for $S_n$ was added in order to have extra information of the mixing level. It is possible to appreciate the significant differences of the dot distribution within the plots (details in the text).*

was relatively small (below 1 m) and different mixing level were observed. The second interval corresponds to the low mixing activity just after the WT1 transition. The patch size range was much wider and patches as big as 3.5 m were recorded. However, in all the cases the mixing level was minimum, as it can be observed by the low values of the ratio $L_{Tmax}/L_p$ and the $S_n$ codes. Big patches with low level of mixing are according with the idea of strong but very short mixing event. The third interval shows the transition to high mixing levels with a general trend of increasing $L_{Tmax}/L_p$ ratios. The fourth interval corresponds to the highest turbulent activity, which was reflected in the diagram by the maximum values of $L_p$ and $L_{Tmax}/L_p$ ratios.

### 3.5.1 Comparison between diagrams

The results obtained with the proposed diagram were compared with the results obtained with the diagrams proposed by Gibson (1980-85) and Imberger and collaborators (1986-91). Figure 3.21 shows the four plots associated to the three different hydrodynamic diagrams. In all three cases, it is possible to observe differences between the different stages of turbulent activity.

In Gibson's diagram, it seems that the temporal evolution is going "backwards" to the arrow of time proposed by the author (figure 3.3). This apparent contradiction could reflect the restrictions of this diagram. The strongest assumption in Gibson theory is that turbulence decreasing depends only on the damping external forces (buoyancy in the vertical). However, the temporal variability of the inertial forces can be an important factor of the evolution of the turbulence and the data reported in the present analysis may be an example of the effects from non stationary external forcing.

In Imberger and collaborators diagram it is not assumed any time dependence of the turbulent stage, and the results obtained are in general according to those obtained in the proposed diagram. The series of diagrams indicates a transition from anisotropic turbulence, during the low turbulent activity interval, to isotropic turbulence. However, the differences between stages in that diagram are less conspicuous, and it is difficult to infer the evolution of the mixing process.

The new diagram has shown to be able to detect a transitional phenomenon during the rising period of the wind burst. The results obtained suggest that an intense but very short mixing event generated large vertical turbulent patches, which were only locally mixed. The main advantage of describing turbulent properties from topological measurements is that the structure integrates the different mixing events. The fast processes can be detected from the topological changes on the structure, and it is possible to recover many dynamical properties from this method of description.

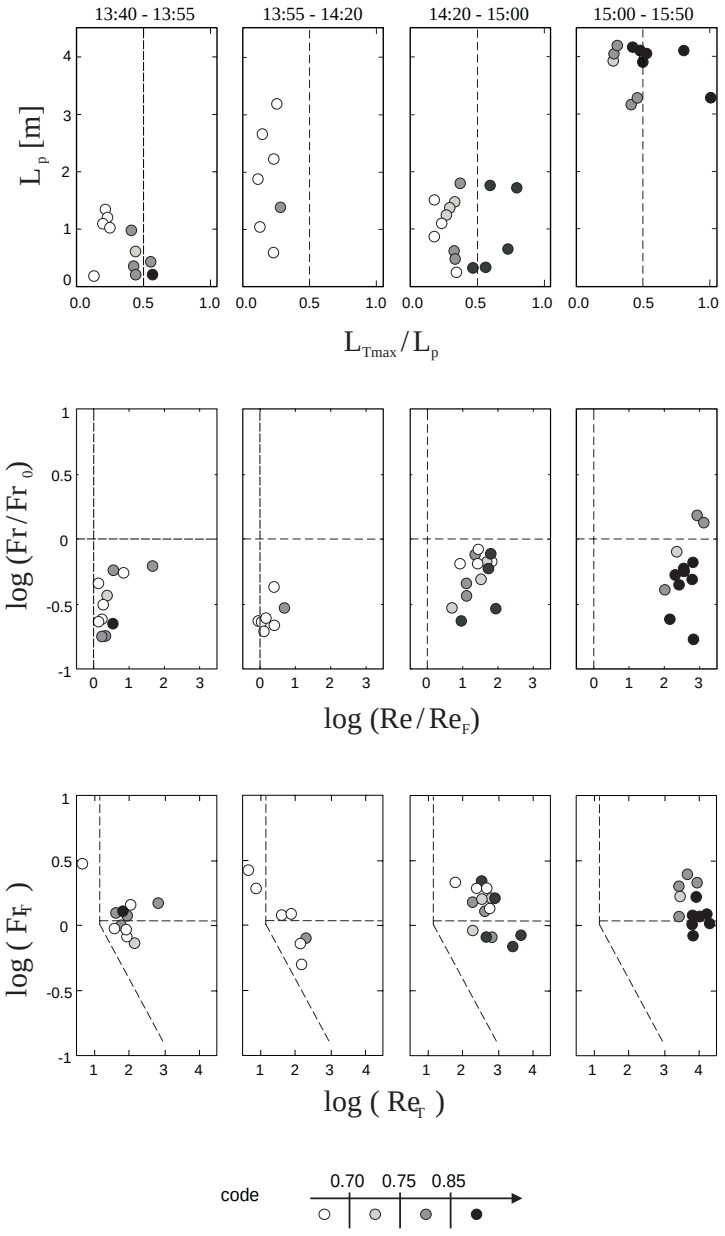


Figure 3.21: *Comparison of the results obtained from the proposed diagram (top) and the diagram proposed by Gibson (1980-85) (middle) and Imberger and collaborators(1986-91) (down). The color code for $S_n$ was mantained as a reference of the mixing level.*

From the results obtained with the new method of description, it seems more reasonable to accept the hypothesis of "fast response dynamics". Additional support for this hypothesis can be shown in fig 3.22.

The figure represents data from the Lago Maggiore and Lake Banyoles campaigns, corresponding to the turbulent dissipation rates measured near the surface. The values of the dissipation rate are presented in a simple form, differentiating values higher or lower than certain threshold ($\varepsilon > 9\,10^{-9}$ $(m^2\,s^{-3})$ and $\varepsilon > 1\,10^{-8.5}$ $(m^2\,s^{-3})$ for the Lago Maggiore data and Lake Banyoles data respectively) . This simplification allows to highlight that, during the intervals corresponding to the rising velocity of the wind events, the values of $\varepsilon$ near the surface decreased below that thresholds. The decrease was very short in time and only happened during these specific intervals, except in during the first interval of the measurements in Lago Maggiore, but in this case the low dissipation rates can be explained because there was no wind. These field observations suggest again that the energy flux in the water column diminished during the first intervals of the wind events, according to the hypothesis of "fast response dynamics".

## 3.6 Inferring time and velocity scales from topological descriptors

The scaling law proposed by Taylor (1935) $\varepsilon \approx u^3/L$, relates the turbulent dissipation rate with the velocity and length scale $L$ of the overturning eddies. This scaling law provides the method to infer velocity and time scales of turbulent patches from microstructure measurements.

$$u = \left(\frac{\varepsilon}{L}\right)^{1/3}; \qquad t = \frac{L}{u} \tag{3.38}$$

where $\varepsilon$ and $L$ would be the turbulent dissipation rate and the characteristic length scale of the turbulent patch. The main question resides in which length scale should be considered as length scale of the turbulent patches to estimate the scales of velocity and time. As it was mentioned previously in the definition of the Thorpe scale, $L_T$ is commonly considered the statistical measure for the vertical size of overturning eddies, and has been widely used as the reference scale.

Traditionally, overturns have been identified from Z-like structures either from $d_T$ or density fluctuations (fig. 3.23 A1) as they resemble to the simpler structure generated by the solid-body overturn model (fig. 3.23 A2). But, the schematic presented in fig. 3.23B-C shows that this type of structure could

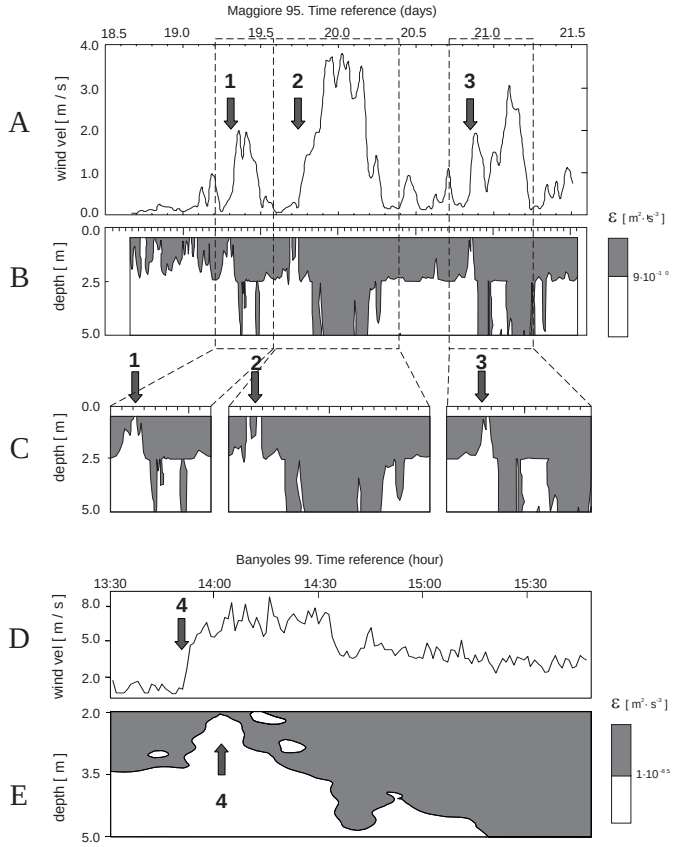


Figure 3.22: *(A-C) Data corresponding to measurements in Lake Maggiore from Stips et al. (1996). The measurements were recorded at December 18 to 21 (1995) . (A) Wind velocity. The raising point associated to each wind event is pointed with an arrow. (B) Kinetic energy dissipation rates $\varepsilon$ measured at 2-5 m depth. Grey regions correspond to depths in which it was recorded $\varepsilon > 9\,10^{-9}$ $(m^2\,s^{-3})$. (C) Detail of the enhanced dissipation rates periods. A significant reduction of dissipation rates can be observed just after the begining of each wind event. (D-E). Data correponding to Lake Banyoles. The fast decreasing of turbulent dissipation rate, just after the rising period of wind is also detetcted.*

be obtained from a mixed layer, although the final structures resemble more to a rhomboidal than a Z-like structure. In fact, the structures obtained in field data are, rhomboidal forms (fig. 3.23D). In a well-mixed turbulent patch with vertical size $L_p$, the maximum displacements may be achieved by the fluid particles situated at the boundaries of the patch. If some particles are displaced along the patch, the maximum value of $d_T$ ($L_{Tmax}$) be similar than $L_p$. The displacement of fluid particles situated in the middle of the patch would be restricted to a maximum displacement of $L_p/2$, but it could be in both directions. In this case, the displacement boundaries are represented by a rhomboidal form as it is shown in fig 3.23E (dotted line). If the turbulent patch is only partially mixed, the maximum displacements are smaller and the rhomboidal form is stretched (fig. 3.23E solid line). The maximum displacements provide information about the relative mixing within the patch. Therefore, $L_{Tmax}$ (and hence, $L_T$) should be considered the characteristic mixing scales for the turbulent patches.

What is not clear, however, is that mixing and overturn scales could be considered analog concepts.

Figure 3.24 shows the $d_T$ profiles from two of the big patches detected in the field data. The first big patch (fig 3.24A) corresponds to the low turbulent activity period. Different structures can be observed in the $d_T$ profile that could be explained as a consequence of different mixing events (fig 3.24C). The second example (fig 3.24B) corresponds to the high turbulent activity period. The pattern of $d_T$ profile in this case is very different from the first example, showing a big dominant rhomboidal structure. This structure can be generated from different mixing mechanisms. The schematics of fig 3.24D-F examples of the different overturn dynamics that could generate with the final structure.

In this case, the mixing scales could be associated to a wide range of overturn scales, with very different velocity and time scales. It is not possible to deduce the particular dynamical process from topological descriptors, and then, it is not possible to determine the velocity and the time scale characteristic of these dynamics.

In some cases it could be possible to set a reference of time $t_0$, at the beginning of the mixing process.. In these cases, it could be computed a characteristic mixing velocity $u_m$ as

$$u_m = \frac{L_{Tmax}}{\Delta t} \tag{3.39}$$

considering $L_{Tmax}$ the characteristic mixing scale, and $\Delta t = t - t_0$. However, this is a particular case and, in general, it must be necessary to obtain additional information for inferring the velocity and the time scales characteristic

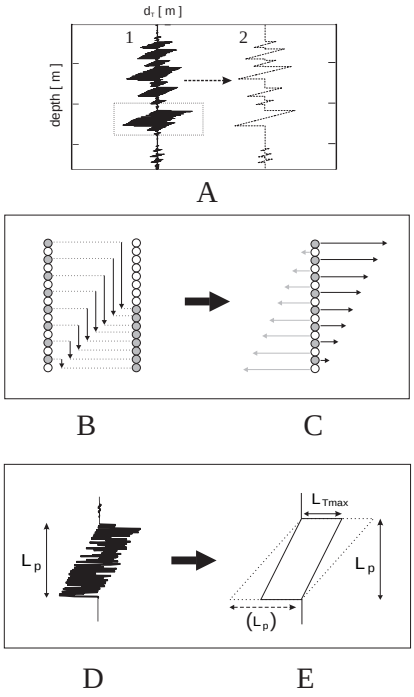


Figure 3.23: *(A) Example of $d_T$ profile (A1) in which several turbulent events can be observed as Z-like structures. These type of structures resemble to the simpler structure generated by the solid-body overturn (A2). (B) Schematic showing an example of computed displacement values obtained in a mixed layer. (C) This example would yield in a similar structure observed in A1.*

of the turbulent patches.

## 3.7 Summary and conclusions

The main objective in this chapter has been to propose a method for describing the most relevant properties of mixing, based on the length scale analysis of the turbulent patches.

In the reviewed literature, it has been shown that there is a controversy on the interpretation of the results obtained with this type of analysis, mainly derived from the different views of how the turbulence evolves. In order to interpret the field data results, it has been required the observation in which the evolution of turbulent processes were well established.

There are few geophysical observations in which consecutive temporal stages are well defined. An example of such processes has been proposed.

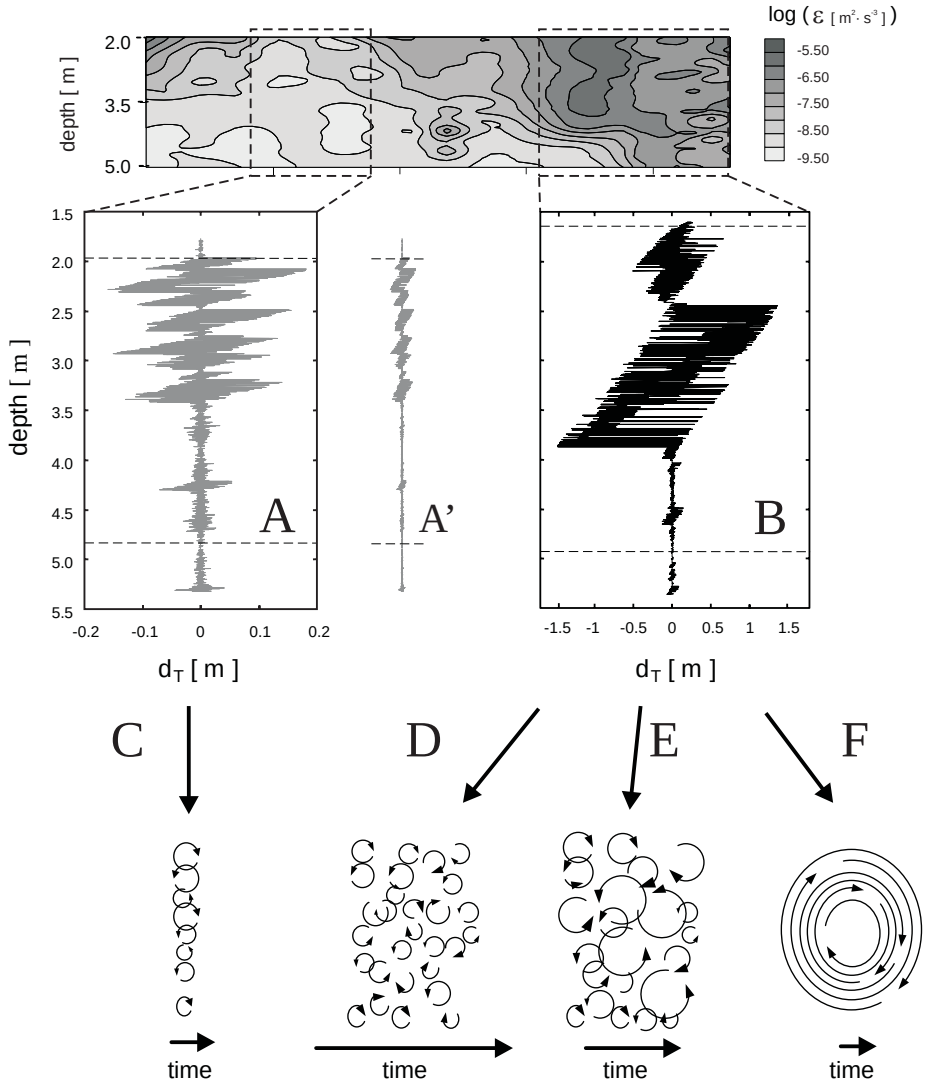


Figure 3.24: *$d_T$ profiles from two of the big patches detected in during the period II. (A) Profile corresponding to the low turbulent activity period. (B) Profile corresponding to the high activity period (A' for comparison, low turbulent activity profile plotted at the same scale as B profile). (C-D-E) examples of the overturn processes that could be associated with the final structure in each profile.*

It occurs at the near surface layer during the initial stages of a wind burst. This is a very complex phenomenon from dynamical point of view, and a complete description was beyond the scope of the present analysis. From the qualitative point of view, however, two different mechanisms have been proposed to explain the initial field observations. The contrast of these hypotheses has been used as a framework to determine the relevant descriptors of the turbulent patches.

Data from Banyoles 99 campaign, corresponding to the evolution of mixing after a wind burst has been analyzed using different methods. The final results yielded in a new hydrodynamic diagram, based on the turbulent patch size $L_p$, and the ratio $L_{Tmax}/L_p$. The parameter $L_p$ determines the range depth in which there is some turbulent activity, and the ratio $L_{Tmax}/L_p$ has been considered an indicator of the relative mixing within the patch.

From the ecological point of view, this type of diagram can be very useful as the related descriptors provide an integrated description of the evolution of the turbulent regime. These descriptors can be compared with different ecological field data in order to relate the changes of the turbulent regimes with ecological response to these changes.

From the physical point of view the proposed descriptive method, rather than alternative, should be considered a complementary diagram. The method cannot provide information about details of the dynamical scales of velocity or time, but gives additional topological information. The topological information integrate the changes on the structure and provides information about turbulent events that are very difficult to detect from direct measurements.

# Chapter 4

# Integrating field measurements in mixing ecological models

Biological populations are composed of individuals whose movements are usually limited in space. Consequently, ecological systems show heterogeneity and patchiness at a broad range of temporal and spatial scales. In recent years, ecologists have become increasingly aware of the influence of spatial heterogeneity on the dynamics of populations (Wilson and Keeling, 2000).

In aquatic ecosystems mixing plays an important roll on the dynamics of spatial patterns. The mixing effectiveness can be a control parameter on the complex dynamics of chemical reactions and ecological interactions (Epstein, 1995). For this reason, there is a strong need to understand and quantify the dynamics and patterns of mixing.

A common approach for integrating the turbulent mixing effects in ecological processes is through the development of numerical models. In general, numerical models are not able to simulate directly the effects of turbulence due to the limits on temporal and spatial resolution, and mixing must be described in terms of empirical or modeled parameters. Different approaches of turbulent mixing parameterization have been developed during the last decades. In this chapter a new method of turbulent mixing parameterization, based on data obtained from microstructe profiles, is presented.

The chapter is divided in four sections. In the first section the different types of turbulent mixing models are reviewed, comparing the advantatges and disvantatges of the two major grups of models, local and non-local mixing models. The second section introduces the nonlocal transilient turbulent theory, which has been used as the basis for the proposed parameterization method. The method is explained in the third section and, in the last section, field data examples are presented in order to evaluate the results obtained with this new methodology.

## 4.1 Turbulent mixing models

The turbulent mixing models considered in this chapter are one-dimensional. This is a general approach and it does not imply that lateral gradients are unimportant but that changes produced by horizontal advection are assumed to be much slower than those produced by vertical fluxes.

### 4.1.1 Physical framework. The transport equation

The mixing models are based on turbulent transport equations. The transport equation for a parameter of interest $\theta$, can be derived from the law of mass conservation (Imboden, 1981)

$$\frac{\partial \theta}{\partial t} = \underbrace{D_\theta \left( \frac{\partial \theta^2}{\partial^2 x} + \frac{\partial \theta^2}{\partial^2 y} + \frac{\partial \theta^2}{\partial^2 z} \right)}_{Diffusion} - \underbrace{\frac{\partial}{\partial x}(u\,\theta) - \frac{\partial}{\partial y}(v\,\theta) - \frac{\partial}{\partial z}(w\,\theta)}_{Advection} + \underbrace{J(\theta)}_{Local} \tag{4.1}$$

which in vector notation is

$$\frac{\partial \theta}{\partial t} = D_\theta (\Delta\,\theta) - \nabla (\mathbf{v}\,\theta) + J \tag{4.2}$$

$D_\theta$ is the molecular diffusion coefficient of the scalar $\theta$, $\mathbf{v} = (u, v, w)$ is the advection velocity and $J(\theta)$ represents the local function associated to the sources and sinks. In ecological models, $J(\theta)$ will be associated to births and deaths, if $\theta$ represent the number of organism, or production-consumption if $S$ denotes the concentration of any chemical compound.

Applying the Reynolds decomposition (eq.1.17) to $\theta$ and $\mathbf{v}$ the mean of eq 4.2 becomes (Imboden, 1981)

$$\frac{\partial \overline{\theta}}{\partial t} = D_\theta \left(\Delta\,\overline{\theta}\right) - \nabla \left( \overline{\mathbf{v}}\,\overline{\theta} + \overline{\mathbf{v}'\,\theta'} \right) + J \tag{4.3}$$

Thus, the advective mass flux $\mathbf{v}\,S$ is decomposed into mean flux $\overline{\mathbf{v}}\,\overline{\theta}$ and turbulent flux $\overline{\mathbf{v}'\,\theta'}$.

The turbulent mixing models needs to estimate the turbulent flux $\overline{\mathbf{v}'\,\theta'}$. Two main categories of turbulent mixing models can be considered based on the method for evaluating the turbulent flux: the local models and non local models.

### 4.1.2 Local or diffusive models

Local models assumes that turbulent fluxes can be considered analogous to molecular diffusion. In this case, the term $\overline{\mathbf{v}'\,\theta'}$ is assumed to be proportional

to the local gradient, and then, can be estimated by appliying a Fickian law

$$\overline{\mathbf{v}'\,\theta'} = -\mathbf{K}\,\nabla\overline{\theta} \tag{4.4}$$

where the parameter $\mathbf{K}$ is the tensor of eddy diffusivity. In general $\mathbf{K}$ is not diagonal but can be transformed into diagonal form by choosing a suitable coordinate system. Considering only the vertical component for the unidimensional models, vertical turbulent fluxes can be estimated as

$$\overline{w'\,\theta'} = -K_z\frac{\partial\overline{\theta}}{\partial z} \tag{4.5}$$

**Local closure parameterization**

Functional forms of $K_z$ can be parametrized from dimensional arguments and empirical data. Several models have been developed for computing the vertical eddy diffusivities from microstructure measurements (for a detailed review see Gregg, 1987).

Osborn and Cox (1972) proposed a model for $K_z$ based on temperature fluctuations $T'$. Considering that the rate of production of temperature variance (fluctuations) by turbulence is in balance with the rate of diffusive smoothing, $K_z$ can be expressed as

$$K_z = 3D_T\frac{\left\langle(\partial T'/\partial z)^2\right\rangle}{\left\langle(\partial T/\partial z)^2\right\rangle} = D_T\,C \tag{4.6}$$

where is $D_T$ the molecular diffusivity of temperature and $C$ is the Cox number (eq. 3.12).

An alternative model for $K_z$ was proposed by Osborn (1980), based on the temporal changes of the turbulent kinetic energy ($TKE$). Assuming an steady state of the $TKE$ balance, and considering that a fraction $\gamma_{mix}$ of the turbulent kinetic is transformed in potential energy, $K_z$ is obtained as:

$$K_z = \gamma_{mix}\,\frac{\varepsilon}{N^2} \tag{4.7}$$

In the cases in which it is possible to assume the equivalence between the Thorpe scale and the Ozmidov scale ($L_O \approx L_T$), eq 4.7 can be expressed as (Dillon, 1982; Peters et al., 1988)

$$K_z = \gamma_{mix}\;L_T^2\,N \tag{4.8}$$

The methods mentioned above have some methodological restrictions. The parameterization of $K_z$ from microstructure measurements is based on

the assumption of steady homogeneous turbulence, while kinematic models of turbulence predict that mixing occurs as short-lived overturns generated by instability phenomena. In a reference to this inconsistency Gregg (1987) commented "Those of us who examine oceanic data have long recognized this incongruity, hoping that it all works out in the averaging. This however, has yet to demonstrated".

Additionally, eq 4.7 and 4.8 depends on $\gamma_{mix}$, a factor that can be a source of uncertainty. Osborn (1980) set an upper limit value for $\gamma_{mix}$ of 0.2 based on atmospheric boundary layer studies. Several field observations and laboratory measurements (Oakey,1982; Gregg et al., 1986; Moum et al.,1989; Ivey and Imberger, 1991) encompasses the idea to use a "canonical" value of $\gamma_{mix} \approx 0.2$. However, Oakey (1982) reported a wide range of variability of $\gamma_{mix}$ (from 0.05 to 10) in double diffusivity environments. Smyth et al. (2001), using direct simulations, obtained changes of $\gamma_{mix}$ by an order of magnitude over the life of a turbulent overturn, suggesting that the use of a constant value for $\gamma_{mix}$ is an oversimplification.

The last constraint only affects eq. 4.8, which assumes the equivalence between $L_O$ and $L_T$. It has been shown in the previous chapter that this equivalence could be restricted only to some particular mixing scenarios.

### 4.1.3 Nonlocal models

The problems of methodological constraints for the local clousure parameterizacion could be minimized by improved estimation of the eddy diffusivity. However, the main problem of the local models resides in the concept that the local gradient determines the turbulent flux. The constraints of this assumption are apparent in many situations where turbulent flux does not occur in the direction of the local negative gradient (Imboden and Wüest, 1995). Panofsky and Duton (1984) (in Kundu, 1990) show an example of this limitation based on the atmospheric concentration profile of carbon monoxide $[CO]$ (fig. 4.1).

Following the local formulation, the turbulent flux of $CO$ is computed as

$$\overline{w' c'} = -K_z \frac{\partial \overline{c}}{\partial z} \tag{4.9}$$

where $c$ is the concentration of $CO$ (kilograms of $CO$ per kilogram of air). A positive $K_z$ requires that the flux of $CO$ at the level $P$ be downward. However, if the thermal convection is strong enough, the large eddies so generated can carry large amounts of $CO$ from the ground to the point $P$, resulting in a upward flux at this level. The direction of the flux at $P$ in this case is not determined by the local gradient at $P$, but by the concentration

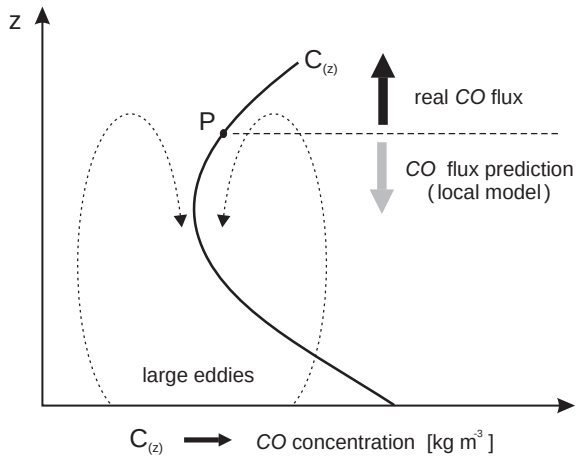


Figure 4.1: *An example of breakdown of eddy difussivity type relation. The large eddies forces an upward flux at point P, while local formulation predicts a downward flux.*

difference between the surface level and point $P$. The only way to estimate the correct flux in this case, using local formulation, is by considering $K_z$ negative, which is not very meaningful.

Trying to solve this limitation, the nonlocal models consider that turbulent transport are produced by a spectrum of eddies, some of which may carry fluid and conservative properties over considerable distances (fig 4.2).

The non local models take into account that turbulent flux $\overline{\mathbf{v}'\,\theta'}$ is derived as the turbulent component of the advective mass flux $\mathbf{v}\,\theta$ (eq. 4.3). From this view, turbulent transport is assumed, rather than diffusive, an advective phenomena (Stull, 1991). Many investigators have independently reached the conclusion that nonlocal mixing is important (eg. Imboden 1981; Jenkins, 1985; Boudreau and Imboden, 1987). In particular, Imboden (1981) introduced the exchange model, analog to the transilient turbulent theory proposed by Stull (1984). Transilient turbulent theory, named after Latin word "transilire" (which translates into "fly over" or "leap across") provides a framework for considering the ensemble-averaged effect of eddies of different sizes on the net nonlocal mixing in the vertical. One of the advantages of this theory is that it can be described in a discrete or matrix form (the transilient matrix), which are well suited for numerical ecological modeling.

Nonlocal transport models offer a way to overcome some of the problems of the local formulation. In nonlocal models it is not strictly necessary to

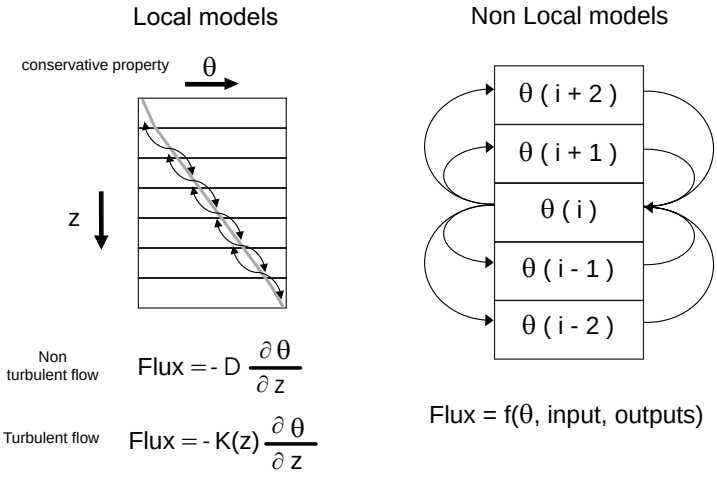


Figure 4.2: *Different views for describing the turbulent flux. In local models turbulent flux is described as diffusive process, depending on the local gradient. In non-local mixing models, the turbulent flux is described as advective process and the max flux is computed from cell to cell.*

assume stationarity nor isotropy of the mixing process. Furthermore, they include not only the small-eddies effects of the local theories but also the medium and large advective-like effects, generated by coherent structures, that local theories misses (Stull, 1991).

However, there is a low number of nonlocal mixing applications from field data reported in the literature. A few examples can be found in the study of mixing within the sediments (Bodreau and Imboden, 1987), mixing in the upper ocean (Stull and Kraus, 1987), or mixing in the atmospheric boundary layer (Stull, 1988). The low number of references can be explained because nonlocal theories are more complex than local theories, and require a considerable quantity of field data for their application (Imboden and Wüest, 1995).

Microstructure profiles provides a significant amount of high resolution data, which can be used as input on the nonlocal models. As it will shown below, and particularizing on the transilient theory, a new method is proposed for determining the transilient matrix from microstructure measurements.

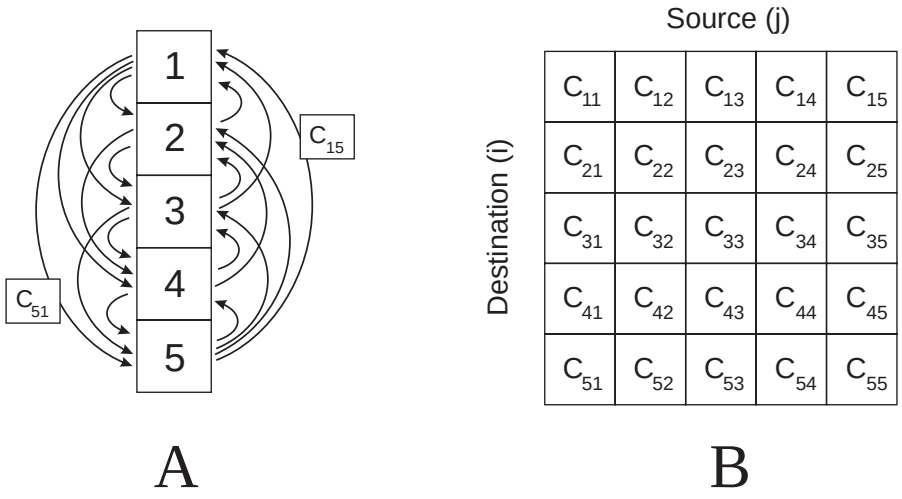


Figure 4.3: *(A) The discrete version of the transilient theory describes the turbulent field as the mixing between pairs of N cells. In the example, the fraction of fluid exchange between layer 1 and 5 is highlighted, labeling both fluxes (B) The superposition of all possible pairs yields in the NxN transilient matrix .*

## 4.2 Transilient turbulent model

In this section the theoretical basis of the transilient turbulent model are introduced. Most of the theory presented below has been compiled from Stull (1991) and (Ebert et al. 1989).

The basis of the transilient mixing resides on the discretization of the column of water in $N$ cells or boxes that are stacked on top of each other. The state of the fluid within each box is characterized by the specific concentration of some property $\theta$.

Turbulent eddies of different sizes transport fluid mass between these boxes. As a result, the concentration of $\theta_i$ in a particular box $i$ at time $t + \Delta t$ becomes a function of the concentration in the other boxes at an earlier time $t$. In a first approach, it is not considered any kind of internal source or sink. In this case

$$\theta_i(t + \Delta t) = c_{i1}\theta_1(t) + c_{i2}\theta_2(t) + ... + c_{iN}\theta_N(t) = \sum_j c_{ij}\theta_j(t) \qquad (4.10)$$

The dimensionless transilient coefficients $c_{ij}$ represent the portion of fluid,

which is mixed into box $i$ from box $j$ during the time interval $\Delta t$. The eq. 4.10 can be generalized to represent the simultaneous turbulent exchange between all boxes. In matrix notation

$$[\theta(t+\Delta t)] = [C][\theta(t)] \tag{4.11}$$

where $[\theta]$ is a $N$-dimensional vector that describes the distribution of $\theta$, and $[C]$ is the transilient matrix corresponding to the $N^2$ transilient coefficients $c_{ij}$.

The local changes can be expressed in eq. 4.11 as an adding function $J([S(t)])$

$$[\theta(t+\Delta t)] = [C][\theta(t)] + J([\theta(t)]) \tag{4.12}$$

### 4.2.1 Physical constraints

To satisfy conservation of fluid mass and state, in the absence of internal sources or sinks, each row and each column of a transilient matrix for uniform grid spacing must sum 1 (Stull, 1984)

$$\sum_{j=1}^{N} c_{ij} = 1, \qquad \sum_{i=1}^{N} c_{ij} = 1 \tag{4.13}$$

The total amount of water at each destination must have come from somewhere and, consequently, each row must sum to 1. For similar reasons, each column must sum to 1 because the total amount of water initially within each cell must go somewhere.

Although it is mathematically possible to have some negative elements and yet satisfy eq. 4.13, the resulting matrix is not physically realistic. Turbulence increases entropy, so each matrix element must be non-negative. Matrix with negative elements would cause unmixing.

Each element must be less or equal to 1.0. Taking into account that each element represents the fraction of the water parcel arriving at a destination from some source, it is impossible that more than 100% of the destination water is arriving from anywhere. Thus

$$0 \leqslant c_{ij} \leqslant 1 \tag{4.14}$$

### 4.2.2 Interpretation of transilient matrices

In order to highlight the underlying physics, transilient matrices are often displayed as a contour plot of element values (Ebert et al. 1989). The mag-

nitudes of matrix elements tell how much water is potentially interchanged between water parcels and the contour plot shows the relative locations where the coefficients reach the highest values.(fig. 4.4A-B)

Figure 4.4C shows an schematic of the relative locations of high coefficient values related to the type of the mixing process. Let's consider, as an example, the elements of the lower left corner of the matrix. These elements are associated to the shallow-parcel sources and deep-parcel destinations. During the time interval $\Delta t$ specified for the matrix, a certain level of water transfer occurs between these sources and destinations. High values of these elements are interpreted as rapid downward mixing. Elements closer to the main diagonal are transported to relative shorter distance during the same time interval, and indicate the intensity of slower mixing processes.

Both the physics and the time step selected determine the magnitudes of elements in a transilient matrix. For a very short time steps, turbulence has no time for mixing water parcels from their starting points, leading to a diagonally-dominated matrix with zeros in the upper and lower triangles. For very long time steps, turbulence can cause a significant mixing across large distances and, in the case of isotropic turbulence, is associated with a full matrix of nearly equal elements.

The coefficients of a matrix representing no mixing are equal to 0 except in the main diagonal where the coefficients are 1. In the case of turbulent patchiness there are some turbulent and nonturbulent subdomains. The matrix range associated to nonturbulent subdomains has ones along the main diagonal. The magnitudes of the submatrix coefficients associated to the turbulent patch will be a function of the mixing level within the patch.

### 4.2.3 Parameterization of the transilient coefficients

In contrast to the preceding general account of transilient theory, the choice of specific formulas or values for the transilient coefficients involves a measure of arbitrariness (Stull, 1987). It has to be justified to some extent by its ability to simulate actual developments realistically.

In general the transilient matrixes have been "measured" with large-eddy simulations, or parameterized from dimensional arguments and empirical data.

#### Large-eddy simulation techniques

Large eddy simulations (LES) make use of Reynold's averaged primitive equations of transport (eq 4.3). The fluctuations cannot be treated with the numerical model because the grid and the time steps are larger than the scales

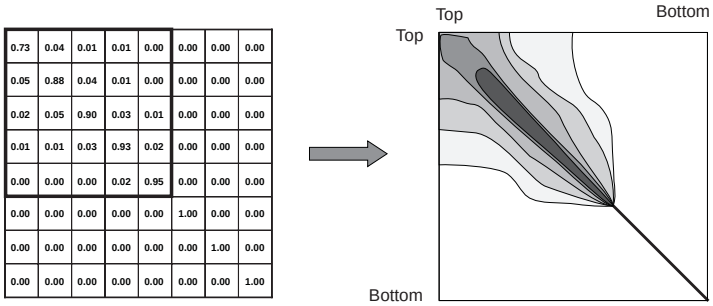


A B

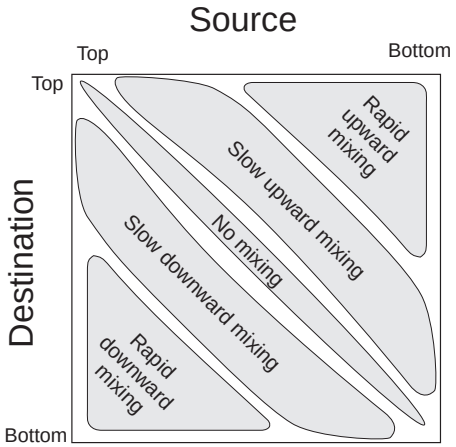


C

Figure 4.4: *(A) Example of the transilient matrix in a numerical format. (B) The sametransilient matrix can be represented as a contour plot. (C) The different type of mixing process can be identified from the relative locations of high coefficient values (Adapted from Ebert et al.1989)*

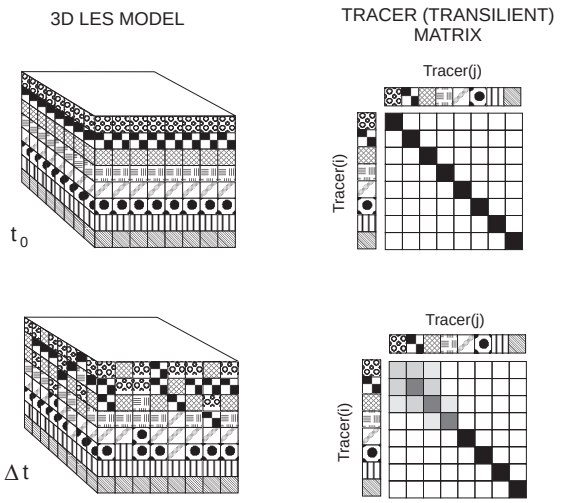


Figure 4.5: *Method used to estimate transilient matrix in large eddy simulations (LES). Once the simulation reaches a quasi-steady stage (t0) each layer is labeled with a different tracer. From this reference time, the tracers are redistributed due to the turbulent flow. The relative fractions of each level is a direct measure of the transilient matrix (Adapted from Ebert et al.1989)*

on which these fluctuations are acting. That is, they resolve the large eddies effect only.

Transilient matrix parameterization by LES techniques requires prognostic equations for the state variables in addition to prognostic equations for N different tracers, where N is the number of the layers in the model.

In this method the transilient matrix is estimated by running two consecutive LES. In the first simulation, the LES is run with zero tracer concentration, allowing the simulated turbulence to reach a quasi-steady state. The final step of this initial simulation is referenced as the initial time $t_0$. The simulation is paused at $t_0$ for "injecting" the tracers into the model (fig 4.5).

The tracers are injected as initially uniform layers, using different tracers for each layer. A tracer matrix $TR$ is constructed in order to evaluate the dispersion of the tracers. Each coefficient of the tracer matrix $tr_{ij}$ corresponds to the mean fraction of tracer $tr_j$ detected in the layer in which the tracer $tr_i$ was injected . At $t_0$, the tracer matrix has 1's in the main diagonal and 0's at the rest.

The LES continue running during the second simulation and the dispersion of the different tracers are stored in the tracer matrix. Because each

tracer was initially injected at only unique source layer, the tracer matrix is equal to the transilient matrix $C(\Delta t)$ where $\Delta t = t - t_0$.

This is a simple direct method for estimating transilient coefficients. The main constraint is that LES technique should be applicable for the mixing process of interest. There is also a secondary constraint related to the computing capability required to solve the simulations. As an example of the computer requirements, we can estimate the total amount of equations to be solved in a particular case. Ebert et al. (1989) estimated the transilient matrix for the atmospheric convective boundary layer, using a 3D LES model with a grid of $80 \cdot 80 \cdot 24$ points. In this model, a total of 29 prognostic equations were defined: 24 for the tracers and 5 for the state variables (momentum, heat and moisture). That yields a total of 4.454.400 $(29 \cdot 80 \cdot 80 \cdot 24)$ equations to be solved at each time step of simulation. Needles to say that is a power computer consuming method.

### Closure parameterization

Like eddy difussivities in local mixing models, functional forms of transilient matrix can be parameterized from dimensional arguments and empirical data. Just there are many parameterizations of $K$ in local mixing models, there can be alternative parameterizations of $c_{ij}$.

The first parameterizations of the transilient matrix were based on Richardson number (Stull, 1984) but required the solution of a complex matrix equation, which was cumbersome. A reframed Richardson parameterization was proposed by Zang and Stull (1992) that allowed the direct solution of the coefficients of the transilient matrix. Alternatively Stull and Driedonks (1987) used a nonlocal analogy to the turbulent kinetic energy equation to obtain the transilient matrix.

Different parameterizations for transilient matrix introduced different peculiarities. Chrobok (1988) and Zhang and Stull (1992) found that the $TKE$ parameterization leaded to surface layers that were unrealistic thick and well mixed, and mixed layers that were not sufficiently well mixed. This is not an intrinsic problem with nonlocal methods in general, but is an artifact of the particular parameterization (Stull, 1991). For example, Zhang and Stull (1992) found that Richardson number parameterization did not have this problem.

## 4.3 Computing the transilient matrix from microstructure profiles

In this section a new proposed method for estimating the coefficients of the transilient matrix, based on microstructure measurements, is introduced.

### 4.3.1 A new parameterization of transilient coefficients

The parameterizations of $K$ in local mixing models or $c_{ij}$ in the transilient mixing models are usually based on a "responsive" scheme (Stull, 1987; Stull, 1991). The responsive schemes follows LeChatelier's principle: *if some stress is brought to bear upon a system in equilibrium, a change occurs, such that the equilibrium is displaced in a direction which tends to undo the effect of the stress* (Weast, 1968).

This principle applies to the destabilizing mechanisms generated by convection or shear (Sull, 1991). In aquatic systems convection appears when the surface cooling yields in a superadiabatic layer (in which the temperature gradient is positive, z positive downwards). A turbulent circulation develops in response to this static instability moving the cool water downward. Once the cool water has dropped, the system is again in equilibrium, and the turbulent circulation cease.

A similar feedback mechanism occurs when shear increases to a point where the Richardson number drops below its critical value, and the flow becomes dynamically unstable. Turbulence develops to mix the faster and the lower water streams, resulting in a new equilibrium velocity field that is dynamically stable with no turbulence.

In many real situations the external stress is brought to bear over long periods of time. In this case the system is continuously responding and the turbulence is maintained as long the imposed forcing continues.

In numerical simulations this principle is approximated in finite difference form, describing the destabilization and stabilization processes happening in steps (Stull, 1991).

In the present work the parameterization of the transilient matrix is estimated following a responsive scheme in front of the instabilities identified in each microstructure profile. The averaging of the set of responsive coefficients provides statistical robustness for the parameterization of the transilient matrix.

The transilient parameterization is based on the $d_T$ profiles. Based on the Thorpe displacement definition, the computed $d_T$ are viewed as the responsive displacements necessary to obtain the static stable profile.

However, the computed displacements would eliminate only the instabilities associated to the measured profile, which is a snapshot of the dynamic process. The displacement profiles then, only corresponds to a single estimate of the responsive mechanism.

In the previous chapter it has been shown that the Shannon entropy, a synthetic parameter of the displacement distribution, can be considered and indicator of the level of mixing. From this result the responsive mechanism, and the transilient coefficients within the patch, are estimated based on the following assumptions

1. The displacement distribution is the characteristic responsive mechanisms of the turbulent patch.

2. This characteristic responsive mechanism can be applied to the depth range determined by the vertical size of the patch.

### 4.3.2 The transilient matrix from a single profile

The estimation of the transilient matrix from a single profile comprises two steps. In the first step the vertical size of turbulent patches is used for determining the boundaries of the transilient submatrix associated to each turbulent patch. In the second step the $d_T$ distribution is computed from each turbulent patch and it is used as an input for estimating the transilient coefficients within each subdomain.

#### The boundaries of transilient patch submatrix

The transilient subdomains associated to the turbulent patches are, by definition, the regions where there is turbulent exchange. Consequently, each turbulent patch should be represented in the transilient matrix as a submatrix where the coefficients of the main diagonal are smaller than 1 and some of the rest values are bigger than 0.

The turbulent patches are identified following the method proposed in the previous chapter. Once the vertical boundaries associated to each patch are computed, it is relatively simple to define the square submatrix associated to each turbulent patch following the procedure explained graphically in the figure 4.6.

#### The coefficients of transilient patch submatrix

The coefficients within the submatrix are estimated from the probability distribution of $d_T$ within the turbulent patch. The probability distribution of

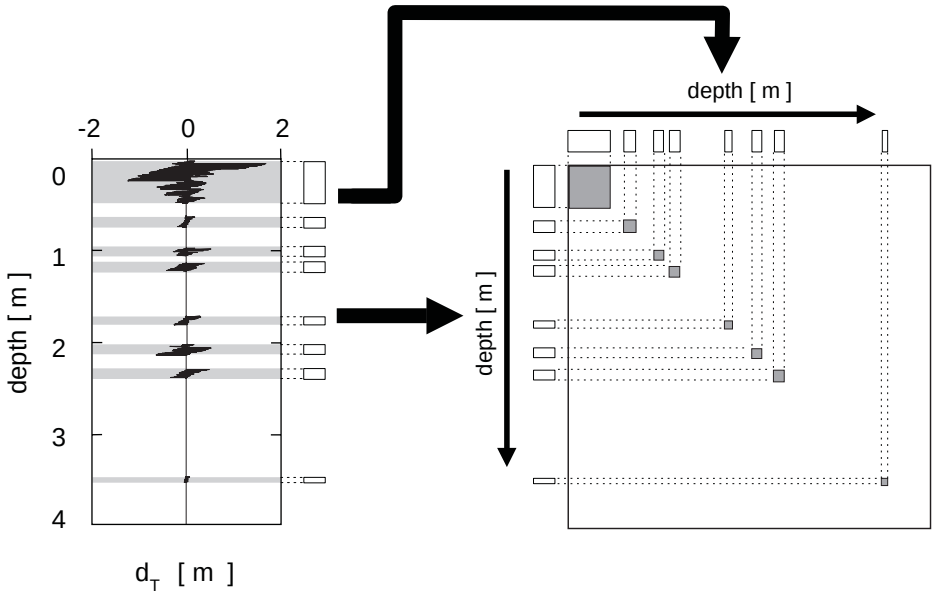


Figure 4.6: *The depth and the vertical size Lp associated to each turbulent patch determines the boundaries of the different turbulent subdomains in the transilient matrix.*

$d_T$ is computed in bins of 1 cm long as it has been explained in the previous chapter. The bin size determines the vertical resolution for the transilient matrix. The choice of 1cm provides then a transilient matrix resolution of $\Delta z = 1\ cm$ which is very high. The probability of each displacement $d_{T_i}$ is interpreted as the fraction of the water parcel at $z_l = l \cdot \Delta z$ that should be turbulent transported to the depth $z_l + d_{T_i}$ for damping the instabilities. This value parameterizes the transilient coefficients for the "source" layers. Assuming that the probability distribution is maintained along the range depth of the turbulent patch, the coefficients are estimated by applying the probability distribution at each column $k$ centering the distribution at transilient coefficient $c_{kk}$, as it is shown schematically in figure 4.7.

The method is only valid when

$$z_{min} < z_0 + d_{T_i} < z_{max} \tag{4.15}$$

where $z_{min}$ and $z_{max}$ correspond to the depth boundaries of the turbulent patches. Near the boundaries it is necessary to recalculate the probability, rejecting the displacements that does not fulfill the condition 4.15.

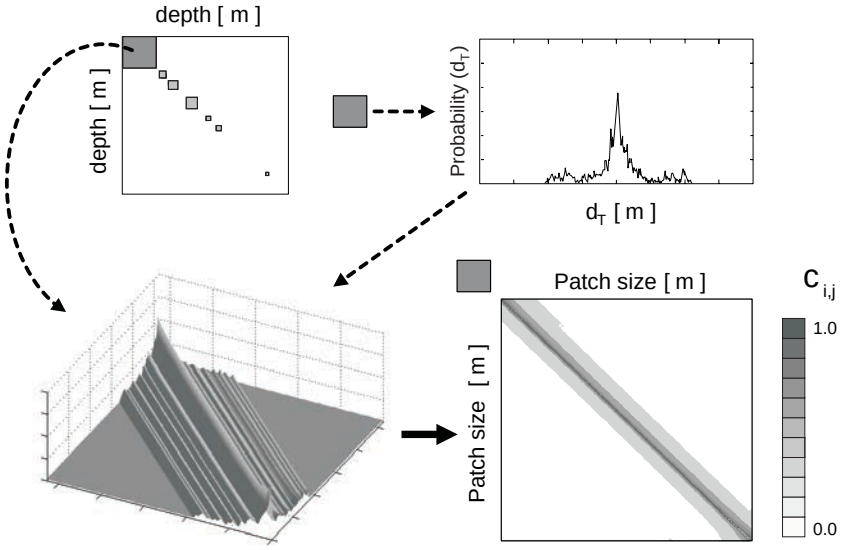


Figure 4.7: *Estimation of the transilient coefficients associated to each turbulent patch. The coefficients are estimated "sliding" the probability distribution of $d_T$ at every column. See text for details.*

The final value of the coefficients should be according to 4.13 for mass conservation. The coefficents are rescaled iteratively applying

$$c_{ij} = \frac{c_{ij}}{\|c_{ij}\|};\ c_{ji} = \frac{c_{ji}}{\|c_{ji}\|} \qquad \|c_{ij}\| = \sum_{i=1}^{N} c_{ij} \tag{4.16}$$

With 500 iterations the final values of the coefficients converge to 4.13 with an error $< 0.5\%$.

### Integration of turbulent submatrix

The final step is to combine the different submatrix to produce the transilient matrix. The computed coefficients for the turbulent patches are assigned to the corresponding subdomain. The coefficients associated to the regions between turbulent patches representing no mixing and then are equal to 0 except in the main diagonal where the coefficients are 1. Figure 4.8 represents a scheme of the final computation.

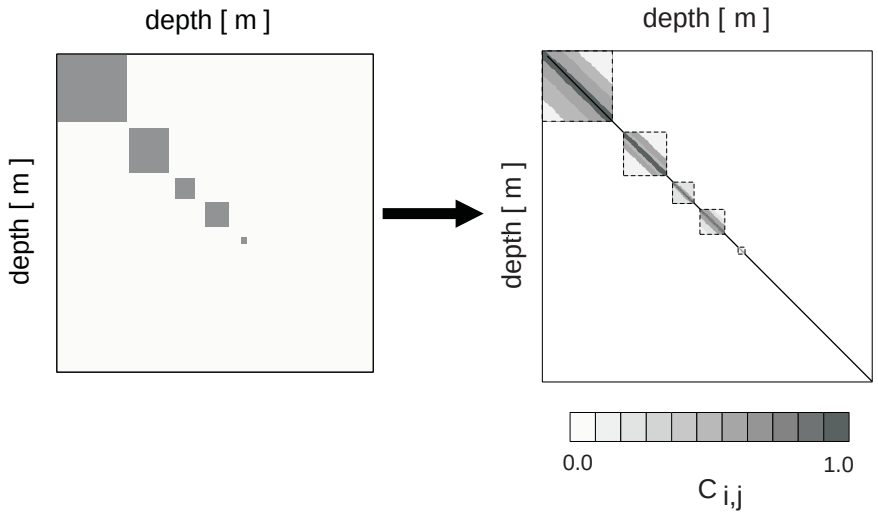


Figure 4.8: *The estimated coefficients for each turbulent patch are positioned at the associated submatrix. The rest of the matrix is assumed to be no turbulent, with 1's in the main diagonal and 0's for the rest of the values*

### 4.3.3 The temporal-averaged transilient matrix

The transilient matrix computed from a single profile is just a "snapshot" of the turbulent state so it is necessary to compute mean coefficients by averaging several matrixes. The mean results are the representative coefficients during the interval $\Delta t = t_{end} - t_{init}$, where $t_{init}$ corresponds to the reference time associated to the first microstructure profile and $t_{end}$ the reference time for the last microstructure profile (fig 4.9).

A minimum number of profiles is needed in order to obtain robust statistical results. There will be then a compromise between the statistical robustness and the temporal resolution $1/\Delta t$.

Stull (1985) proposed a formula for relating matrices associated to different time steps

$$C\left(t, \Delta t_2\right) = \left[C\left(t, \Delta t_1\right)\right]^a, \qquad for \quad \Delta t_2 = a \cdot \Delta t_1 \tag{4.17}$$

which can be used for increasing temporal resolution with $a < 1$. However, eq. 4.17 is only valid for stationary processes. In general, turbulent dynamics is highly intermittent and can not be considered a stationary process. For this reason care should be taken in applying eq 4.17 for increasing temporal resolution, as it will be valid only in some particular cases.

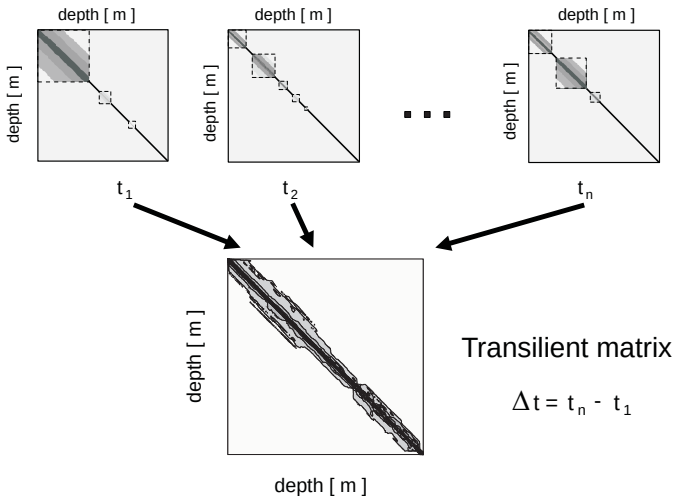


Figure 4.9: *The different transilient matrixes are avegared for computing the final transilient matrix. The $\Delta t$ associated to the final matrix is computed as the interval time from the first to the last microstructuer profile.*

## 4.4 Field data application

The proposed methodology has been applied to measured data from two different campaigns. In these examples the differences on mixing are generated mainly by two different processes.

In the first example the microstructure data was obtained in two consecutive days, in which the mean wind velocity was considerably different, providing two different shear induced scenarios.

The second example corresponds to three different series of microstructure data were the major difference was in the contribution of convective mixing in one case.

### 4.4.1 Shear mixing

The field data was collected at Lake Redo, a high mountain lake situated at the Pyrenees, Spain (42º38'33.5"N, 0º46'12.7"E). The lake with a volume of 77.5 $10^6$ $L$ and a maximum depth of 73 m is situated above the tree line at 2240 m. The lake freezes over in winter and there is a spring and fall overturn. The catchment area (155 ha) mainly consist of exposed granite and alpine grasses and the lake has extreme low conductivity ($\sim$ 16 $\mu S/cm$).

A full description is provided in Catalan (1988).

The microstructure profiles were provided by Jörg Imberger from the Centre of Water Research (CWR) at the University of Western Australia.

### Meteorological conditions and thermal structure

The data was measured during two consecutive days in sumer, the August 6th and 7th of 1991 (corresponding to the julian days 218 and 219, respectively), when the lake was strongly temperature stratified.

Table 4.1 summarizes the meteorological conditions for the two sampling intervals.

The mean values for wind shows that there were two different mixing scenarios for the sampling intervals. During the first sampling interval the wind velocity was relatively calm and the mean value was much lower than the mean value for the second interval. The two sampling intervals scenarios were labeled as low-wind and high-wind for comparison.

The thermal structure for the two sampling periods is shown is fig 4.10.

The series of temperature profiles indicate that there was a well defined seasonal thermocline at 9 m depth approximately. This thermocline was observed in all the measured profiles. Near the surface, the thermal structure was more variable, depending on the time and the changes of the wind speed. In some cases it was possible to appreciate a diurnal thermocline, but with a some variability in the depth in which it was formed. The changes of the thermal structure near the surface are more conspicuous for the second sampling period, when the wind stress was stronger. However, it was possible to observe a general trend in both periods. In the firs interval the a diurnal thermocline appeared at the depth of 4 $m$ approximately (fig 4.10 A), while in the second period it could be observed a deepening of the diurnal layer at the end of the interval sampling reaching the depth of $\sim 7$ $m$ (fig 4.10 B).

### The transilient matrix

Figure 4.11 shows the estimated transilient matrix for the two sampling periods.

| **Day (Interval time)** | **Wind m s$^{-1}$** | **Temperature °C** |
|---|---|---|
| 218 (12:00 -16:55) | 2.01 [ 0.17 - 3.36 ] | 28.71 [ 24.29 - 32.41 ] |
| 219 (8:50 -19:13) | 3.41 [ 2.22 - 4.83 ] | 25.62 [ 21.66 - 29.64 ] |

Table 4.1: Meteorological data corresponding to the sampling days 218 and 219 of the campaing Redo91

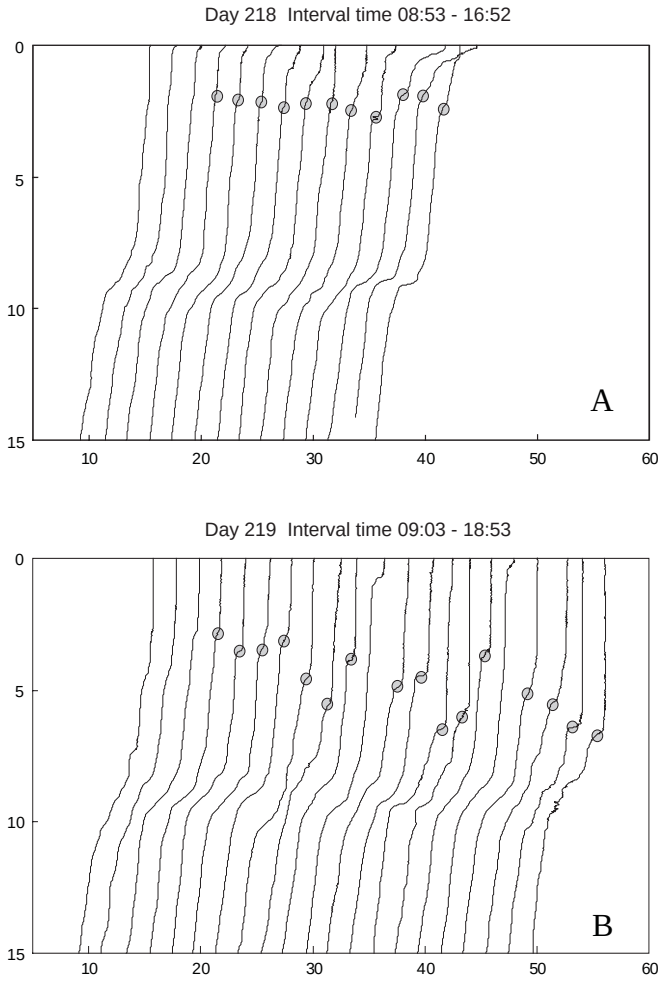


Figure 4.10: *Series of temperature profiles measured during the julian days 218 (A) and 219 (B). An offset of* $\Delta T = 2\,^{o}C$ *has been added to the consecutive profiles in order to show the evolution of the thermal structure during the sampling periods. The dots indicates the depth of the diurnal thermocline.*

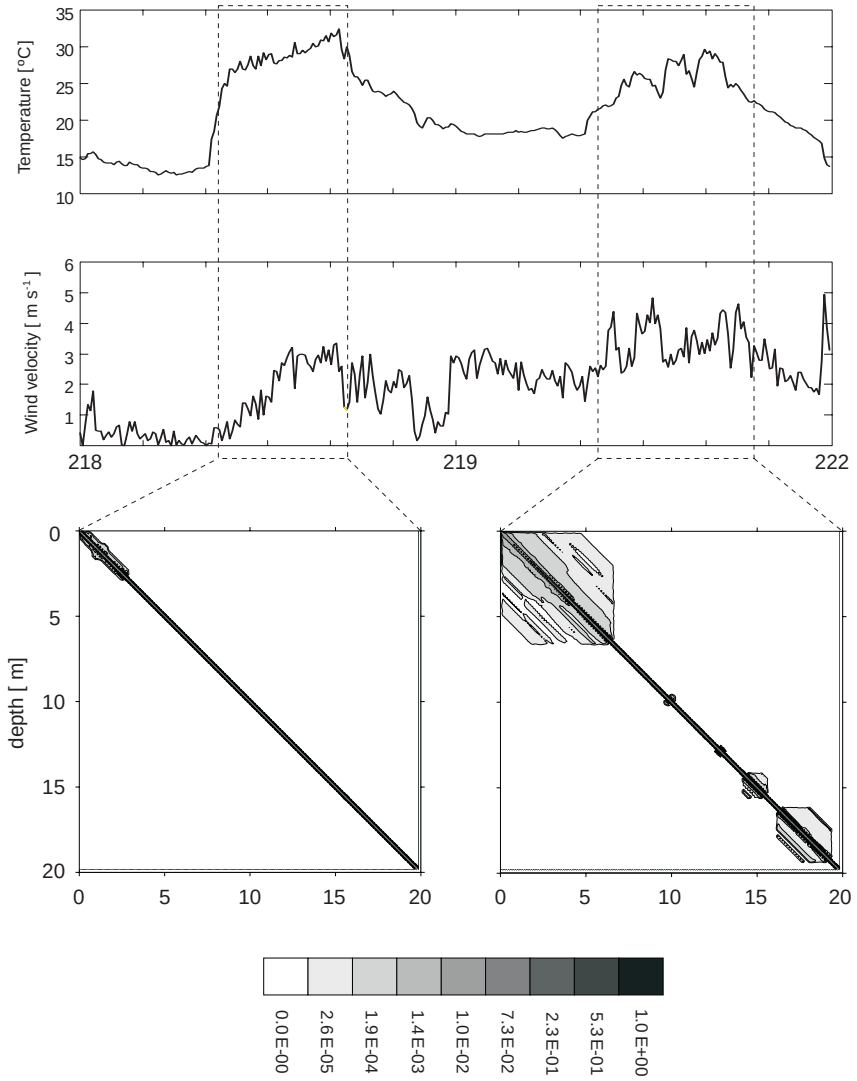


Figure 4.11: *Transilient matrix corresponding to the two sampling periods for the campaing Redo91. Meteorological time series are added on the top for showing the different background conditions.*

The time series corresponding to the air temperature and the wind velocity are also included for providing a detailed framework of the meteorological forcing. During the first interval the wind was initially very low, but was monotonically increasing until the end of the period. The wind velocity measured during second interval was much higher and it was also high during the previous period of the interval sampling.

The following results are obtained comparing both matrices:

1. Matrices were nearly symmetric. Although the patterns were very different, in both cases the matrices had a symmetric pattern.

2. The non zero values for the low-wind transilient matrix were located around the main diagonal. By contrast, in the high-wind transilient matrix, non zero elements were found at large distances from the main diagonal. This result demonstrates a higher mixing activity during the second sampling period.

3. The elements along the main diagonal were at least one order of magnitude larger than the other elements, indicating that the major part of water fraction remains at the same depth.

4. The low-wind transilient matrix had the largest off-diagonal elements near the upper left corner, monotonically decreasing away from that corner. This expected result indicates that surface layer had a higher mixing activity.

5. A similar pattern was found in the high-wind transilient matrix, but the area of surface mixing activity was much larger. Additionally, there were secondary regions of mixing activity at deeper layers, specially between 15 and 20 m depth. This mixing structures can be explained by the seiching activity as the secondary lake response to prolonged wind forcing.

### Transilient statistics

Different statistics can be computed from the coefficients of the transilient matrix. In the following subsections several non-local statistics are presented, based on the analysis proposed by Ebert et al.(1989) and Stull (191). The different calculus provides information that allows to characterize the mixing process from different points of view. The relative locations of high coefficient values within the matrix can provide information about the type of the mixing process and, as it will shown later, some specific properties of the

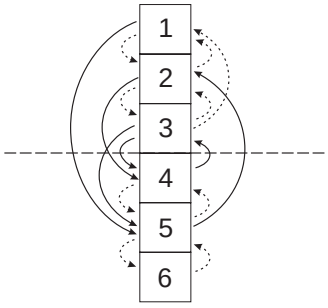


Figure 4.12: *Schematic example of the mixing intensity at* $z_3 = 3\ \Delta z$. *The turbulent transport that crosses level 3 contribute to the mixing intensity at that depth. The rest of the water exchanges (represented as dotted arrows) do not contribute and are not taken into account when computing the value.*

mixing process can be highlighted by decomposing the transilient matrix in different subdomains and computing some statistics from this decomposition.

### Mixing intensity

The nonlocal mixing intensity at depth $z_k = k\ \Delta z$ is defined as (Stull, 1991)

$$P_{z_k}(t, \Delta t) = \sum_{i=1}^{k} \sum_{j=k+1}^{k} \left[ c_{ij}(t, \Delta t) + c_{ji}(t, \Delta t) \right] \tag{4.18}$$

The mixing intensity is the total fraction of water that flows across the layer at depth $z_k$ (fig 4.12)

This parameter provides information about the amount of mixing and can be used as an indicator of the turbulent activity.

Figure 4.13 shows the mixing intensity profiles for the two sampling periods.

The differences between both periods are clear. The maximum mixing intensity value for the second day was one order of magnitude greater than the same value for the first period, showing the differences on mixing activity. The mixed layer can be defined as the depth range in which the mixing activity is greater than zero. In both cases the mixed layer depth coincided with the final depth of the diurnal thermocline, $\sim 4\ m$ for the first and $\sim 7\ m$ for the second sampling intervals.

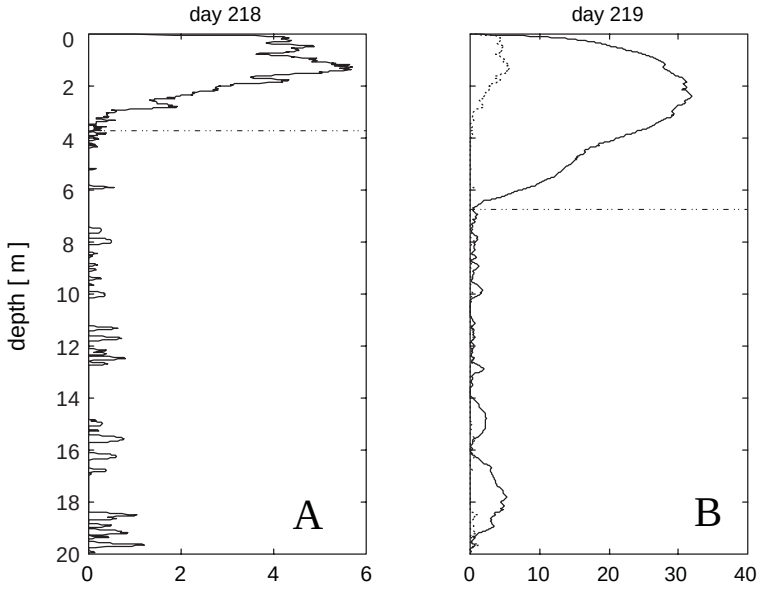


Figure 4.13: *Computed mixing intensity for low-wind interval (A) and high-wind interval (B). For comparison, low-wind mixing intensity profile is also plotted in (B) as dotted line. In both cases the dash-dot line indicates the depth of the mixing layer (see text).*

### Process spectrum

The process spectrum, introduced by Stull (1988), spectrally decomposes the total mixing intensity at a depth $z_k = k\,\Delta z$ into contributions of different-size mixing processes, originated from different locations. Such decomposition can be expressed as

$$P_{z_k}(t,\Delta t) = \sum_{m=1}^{N-1} P_{z_k|L_m}(t,\Delta t) \tag{4.19}$$

The spectral component $P_{z_k|L_m}(t,\Delta t)$ represent the different length scales $L_m = m\,\Delta z$ that contribute to the turbulent flow across the layer at depth $z_k$ (fig 4.14). This parameter can be computed as

$$P_{z_k|L_m}(t,\Delta t) = \sum_{i=1}^{k}\sum_{j=k+1}^{k} \delta_{m,|i-j|}\cdot\left[c_{ij}(t,\Delta t) + c_{ji}(t,\Delta t)\right] \tag{4.20}$$

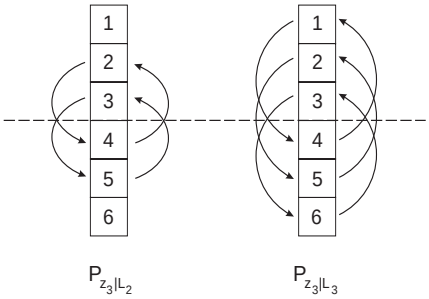


Figure 4.14: *Schematic example of two different components of the process spectrum at* $z_3 = 3\ \Delta z$. $P_{z_3}L_2$ *corresponds to the source-destination pairs of separation distance* $L_2 = 2\ \Delta z$ *that crosses level 3, and* $P_{z_3}L_3$ *corresponds to the source-destination pairs of separation distance* $L_3 = 3\ \Delta z$ *that crosses the same depth level. Each turbulent transport contribute to just one spectral component of the transport spectrum.*

where $\delta_{x,y}$ is the Kronecker delta

$$\delta_{x,y} = \begin{cases} 1 & x = y \\ 0 & x \neq y \end{cases} \tag{4.21}$$

The three most important features of each process spectra are: the integral of the spectrum, that is equivalent to the mixing intensity (eq 4.19); the shape, that indicates the predominant turbulent scales; and the bandwidth, that reflects the largest scales involved on the turbulent flow.

Fig 4.15 shows the computed spectrum process for $z = 0.5$, 2.5 and 5.0 m.

Although with different bandwidth, in all the spectra there is a range of scales contributing to the mixing intensity. The process spectrum associated to the high-wind interval has a wider bandwidth indicating that there was larger turbulent scales involved in the turbulent flow. In all the spectra, the shape indicates that small scale exchanges were predominant, specially at 0.5 m. Near the surface the predominance of small scales could be explained, at least partially, due to the effect of the boundary surface (although there was enough energy to exchange water at larger scales, the surface limited the length of the potential interchange). This effect also explained the deeper the spectra the flatter the shape.

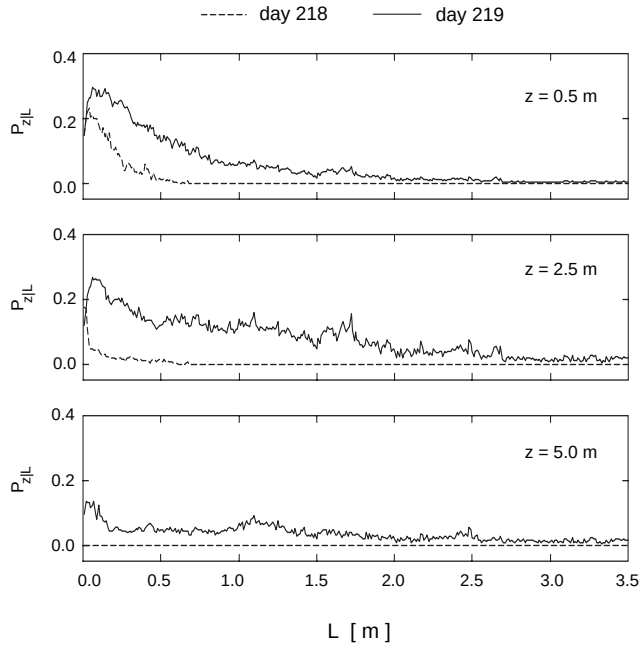


Figure 4.15: *Computed spectrum process corresponding to the low-wind sampling interval (day 218, in dotted line) and the high-wind sampling interval (day 219, solid line). The spectrum has been computed at 3 different depths:* $z = 0.5$, $2.5$ *and* $5.0$ *m. respectively.*

### Mixing length

The concept of a mixing length can be used to describe the vertical distance a parcel moves during the mixing process. The mixing length depends on the relative amount of water transported across various vertical distances and is, therefore, a function of depth. The mixing length at depth $z_k = k\ \Delta z$ can be computed as the mean distance that water parcels move, from or toward the depth $z_k$, weighted by the respective amount of water involved:

$$l_{z_k} = \Delta z \sum_{i=1}^{N} \frac{1}{2}\ \left[c_{ik}\left(t, \Delta t\right) + c_{ki}\left(t, \Delta t\right)\right] \cdot |i - k| \tag{4.22}$$

Figure 4.16 shows the computed mixing length. As it could be deduced from the spectrum process, the mixing lengths are maximum in the boundary surface layers and much larger for the high-wind period. During the second period, the mixing length was also relatively high at the depth range

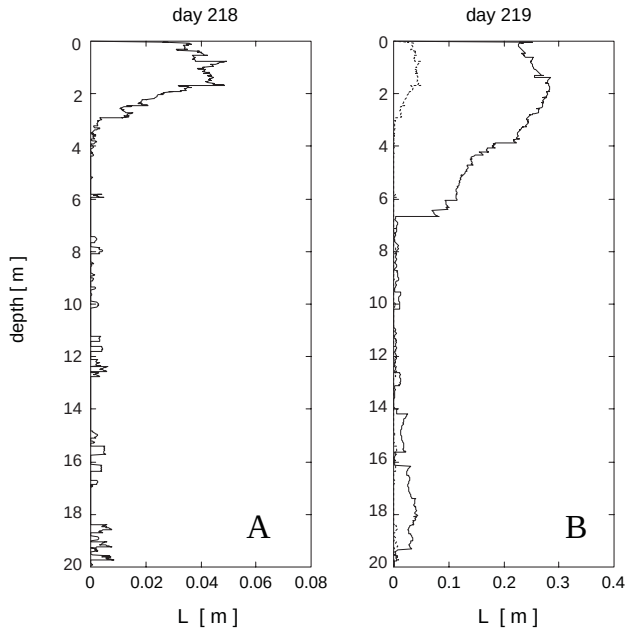


Figure 4.16: *Computed mixing length for low-wind interval (A) and high-wind interval (B). For comparison, low-wind mixing intensity profile is also plotted in (B) as dotted line.*

associated to seiching mixing activity.

### Anisotropy processes

Anisotropy in one dimension is a concept that can be addressed with transilient turbulence theory. The fraction of water mixing upward from one depth can be different than that mixing down from the same depth. In order to reveal the anisotropy, the different fractions of water exchanges can be segregated by considering the direction (upward and downward mixing) and the origin (sources or destinations).

The upward and downward fraction of water from source level $j$ can be computed by segregating the components of the column $j$ of the transilient matrix as

$$f_{z_j}^{\uparrow} = \sum_{i=1}^{j} c_{ij}\,(t, \Delta t) \tag{4.23}$$

$$f_{z_j}^{\downarrow} = \sum_{i=j}^{N} c_{ij}\,(t, \Delta t) \tag{4.24}$$

Using the same reasoning, the upward and downward fraction of water to destination level $i$ can computed by segregating the components of the row $i$ of the transilient matrix as

$$f_{z_i}^{\uparrow} = \sum_{j=1}^{N} c_{ij}\,(t, \Delta t) \tag{4.25}$$

$$f_{z_i}^{\downarrow} = \sum_{j=1}^{i} c_{ij}\,(t, \Delta t) \tag{4.26}$$

An alternative anisotropy parameters can be evaluated by segregating the mixing length with the same criteria. In this case, the upward and downward mixing length from source level $j$ are computed as

$$l_{z_j}^{\uparrow} = \frac{\Delta z \sum_{i=1}^{j} c_{ij}\,(t, \Delta t) \cdot |i - j|}{\sum_{i=1}^{j} c_{ij}\,(t, \Delta t)} \tag{4.27}$$

$$l_{z_j}^{\downarrow} = \frac{\Delta z \sum_{i=j}^{N} c_{ij}\,(t, \Delta t) \cdot |i - j|}{\sum_{i=j}^{N} c_{ij}\,(t, \Delta t)} \tag{4.28}$$

And the upward and downward mixing length to destination level $i$ are computed as

$$l_{z_i}^{\uparrow} = \frac{\Delta z \sum_{j=1}^{N} c_{ij}\,(t, \Delta t) \cdot |i - j|}{\sum_{i=j}^{N} c_{ij}\,(t, \Delta t)} \tag{4.29}$$

$$l_{z_i}^{\downarrow} = \frac{\Delta z \sum_{j=1}^{i} c_{ij}\,(t, \Delta t) \cdot |i - j|}{\sum_{i=1}^{j} c_{ij}\,(t, \Delta t)} \tag{4.30}$$

Figure 4.17 shows the profiles corresponding to the upward-downward mixing lengths and upward-downward fraction of water from source level, computed from the high-wind transilient matrix.

The differences observed in both cases indicates the different mixing intentsiy and the different anisotropy at certain depth levels.

### 4.4.2 Convective mixing

The profiles for the second campaign were taken at the Gossenköllesee, an alpine lake located at the tyrolian region of Kühtai, Austria (47° 13' N, 11° 01' E). The lake is situated above the tree line at 2417 m and it has an area of 1.7 ha and a maximum depth of 9.9 m . The ice cover commonly lasts from November through mid-July. The catchment area is composed of siliceous rocks and approximately 10 % is covered with a poor soil layer.

#### Meteorological conditions and thermal structure

The data was measured during three days in sumer, the August $6^{th}$, $7^{th}$ and $10^{th}$ of 1995 (corresponding to the julian days 218, 219 and 222, respectively). At this time o the year the lake was strongly temperature stratified.

Table 4.2 summarizes the meteorological conditions for the sampling intervals.

The wind velocity was relatively low during the three periods of sampling, although as it will be commented further, it was possible to distinguish some trends in each case. The temperature of the air was not recorded due to some malfunctioning of the sensor but, the mean values for the total radiation indicate a very low radiation (and then lower temperatures) during the second interval of sampling.

The thermal structure is shown in fig 4.18.

Comparing the series of temperature profiles, there is a clear difference between the day 219 (with the lowest radiation and wind velocity) and the days 218 and 222. The series of temperature profiles corresponding to the

| Day (Interval time) | Wind $\mathrm{m\,s^{-1}}$ | Radiation $\mathrm{W\,m^{-2}}$ |
|---|---|---|
| 218 (12:00 -16:55) | 2.42 [ 1.10 - 4.05 ] | 814.31 [ 199.26 - 964.89 ] |
| 219 (8:50 -19:13) | 1.51 [ 0.16 - 2.90 ] | 175.05 [ 18.48 - 304.92 ] |
| 222 (10:24 -20:46) | 1.90 [ 0.47 - 3.35 ] | 626.05 [ 2.68 - 963.63 ] |

Table 4.2: Meteorological data corresponding to the sampling days 218, 219 and 222 of the campaing GKS95

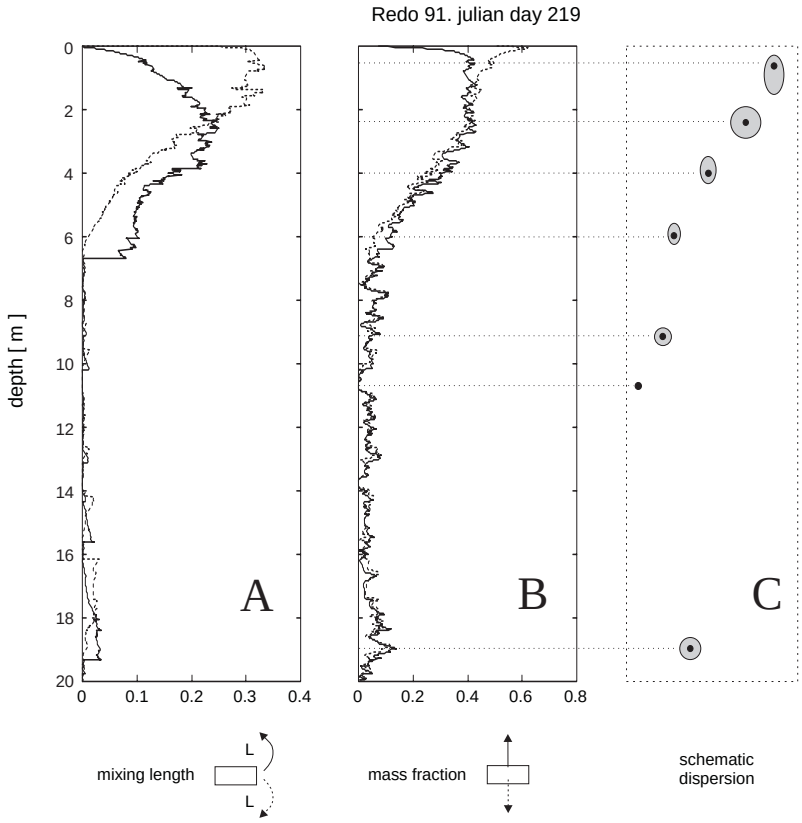


Figure 4.17: *Upward and downward mixing length (A) and fraction of water (B) from source level corresponding to the high wind sampling period. (C) Schematics of the vertical dispersion expected from the results obtained in A and B. The gray figures represents the hypothetical dispersion of some particles situated originally at the depth indicated by the black spot.*

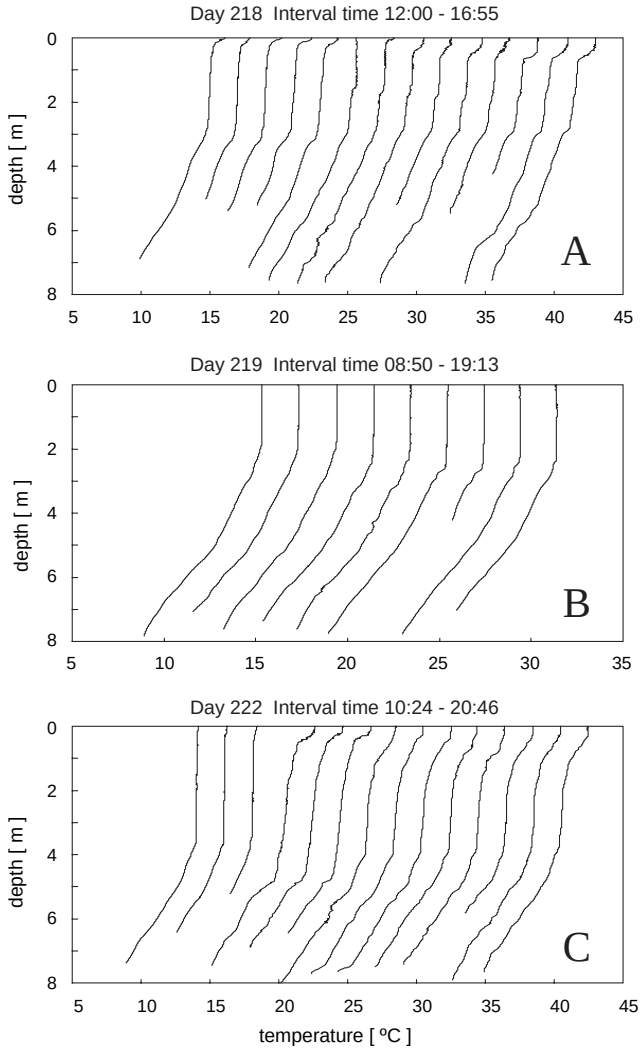


Figure 4.18: *Series of temperature profiles measured during the julian days 218 (A), 219 (B) and 222 (C). An offset of* $\Delta T = 2\,^{o}C$ *has been added to the consecutive profiles in order to show the evolution of the thermal structure during the sampling periods.*

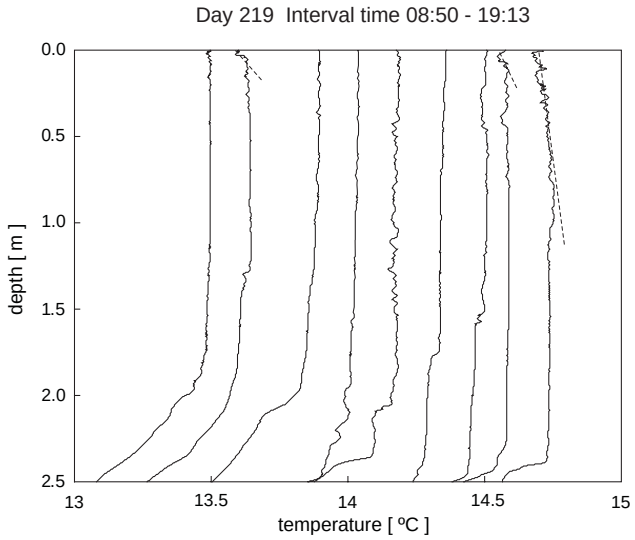


Figure 4.19: *Detailed series of temperature profiles measured during the julian day 219, showing the convective regime. In the casse the offset of* $\Delta T = 0.2\ ^oC$ *has been selected to illustrate the evolution of the thermal structure during the sampling period and the formation of a superadiabatic layer in some profiles (indicated by a doted line).*

low-radiation period present a very homogeneous surface mixed layer. Looking at some detail the thermal structure of the surface at this period (fig 4.19) it is possible to explain why the mixing was stronger during the lowest wind velocity period. The detailed temperature profiles show that in some cases there was a superadiabatic layer on the water surface, indicating that convection contributed to the total mixing.

### The transilient matrix

Figure 4.20 shows the estimated transilient matrix for the three sampling periods.

As in the previous example, time series corresponding to meteorological variables (solar radiation and wind velocity in this case) have been included for providing a detailed framework of the external forcing. The profiles of the first interval were obtained at midday, when the solar radiation was very high. During the first interval the wind was initially very low but at the end of the interval it increased considerably, reaching the 4 $m\,s^{-1}$. The second interval measurements were carried out during a cloudy day, and

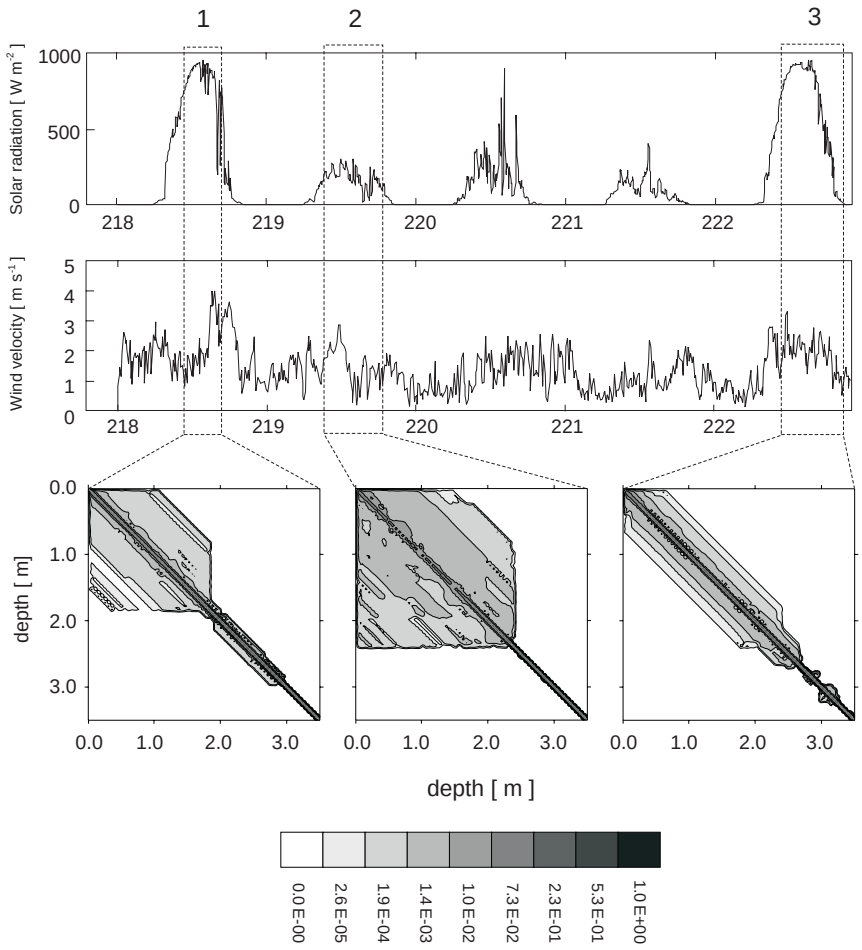


Figure 4.20: *Transilient matrix corresponding to the three sampling periods for the campaing GKS95. Meteorological time series of temperature and solar radiation are added on the top for showing the different background conditions of external forcing.*

the solar radiation recorded during this period was very low. The wind velocity measurements show that there was a short period relatively high, but in general the measurements of wind velocity indicate also low-wind regime. The meteorological conditions for the third sampling interval were similar than the first one. However, the wind velocity was more constant and relatively higher during the first part, and drecreased at the end of the interval.

One of the most important results obtained from the transilient matrix associated to the second interval is that it has certain asymmetry from the main diagonal. Measurements obtained by Ebert et al. (1989) from the LES model, show that the transilient matrix was asymmetric in convective situations. The parameterization proposed by Stull and Driedonks (1987) based on a non local approximation of the turbulence kinetic energy (TKE) equation, required turbulent exchange, which implied a symmetric matrix of transilient coefficients. This constraint was one of the main limitation for this type of parameterization.

The results obtained from the proposed parameterization based on field measurements allows the asymmetry for the transilient matrix, which is, at least from the qualitatively point of view, according with the results obtained by Ebert et al. (1989).

### Transilient statistics

The mixing associated to the convective turbulence is clearly non-local phenomena as the mixing of water, into or out of a region, is related to processes occurring outside of the immediate vicinity of that region, in addition to the local processes. Following the analysis of the first example, the same statistical results have been computed from the transilient matrixes obtained in these three sampling periods, trying to emphasize the differences obtained when mixing is induced by convection.

### Mixing intensity

The mixing intensity pattern (fig 4.21) is analogous to the pattern presented in the previous example. The mixing intensity was much higher during the second interval (by a factor of 5 more or less, fig 4.21B), than those computed for the first and the third interval. The difference on mixing intensity is according with the different background processes, as it is expected a higher mixing activity during the convective regime.

Between the low mixing periods (fig 4.21A,C), it is possible to appreciate some differences, which are according to the background external forcing dur-

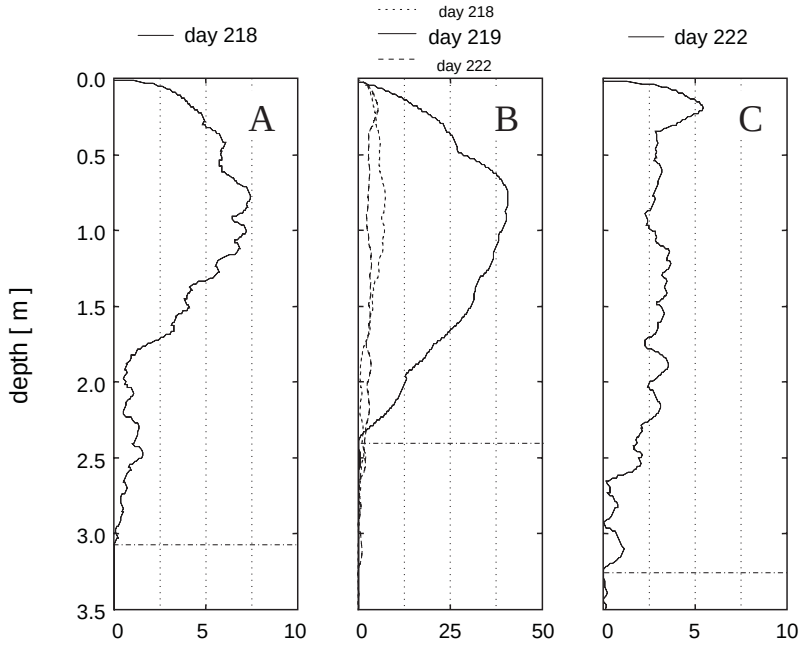


Figure 4.21: *Computed mixing intensity for the measured intervals, corresponding to the julian day 218 (A), 219 (B) and 222 (C). For comparison, low-mixing intensity profiles are also plotted in (B) as dotted line and dashed line. In all cases the dash-dot line indicates the depth of the mixing layer (see text).*

ing the interval measurements. The maximum mixing intensity was higher for the first interval. This difference could be explained by to the strong wind recorded at the end of this mixing period. By contrast, the mixing depth for the last period was larger, which can be explained by the fact that the interval measurements in this period was longer than the first. Some profiles of the third interval were taken at the end of the day, when the radiation was decreased strongly and the restratification forces diminished considerably. In this situation, even a low wind could induce mixing at greater depths.

### Process spectrum

Fig 4.22 shows the computed spectrum process for three selected depths: $z = 0.2$, 0.8 and 2.0 m. Some differences can be observed in the process spectrum pattern during the convective regime when comparing with the

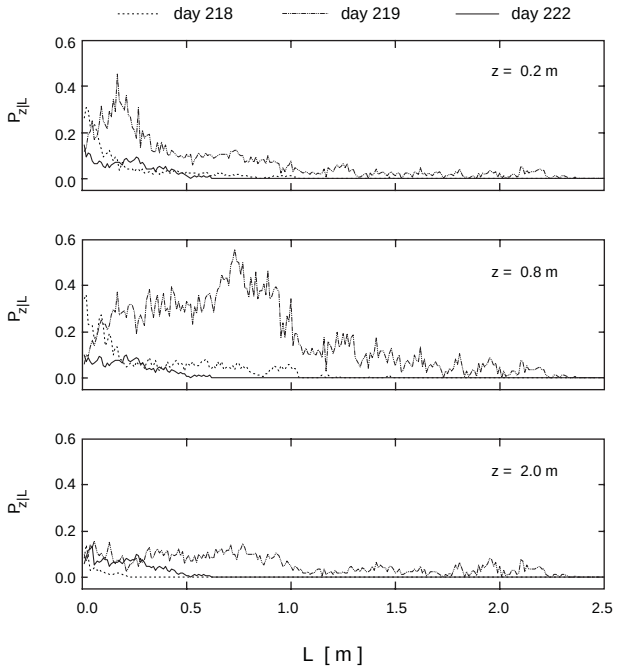


Figure 4.22: *Computed spectrum process corresponding to the three sampling interval day 218 (dotted line), day 219 (dashed line) and day 222 (solid line). The spectrum has been computed at 3 different depths:* $z = 0.2$, $0.8$ *and* $2.0$ *m. respectively.*

previous example.

The main differences are in the high-mixing periods. In the first case, where mixing was generated by wind induced shear, the differences between low-mixing and high-mixing were reflected mainly on the increase of bandwidth when the mixing activity was higher. In the present case, the high mixing activity spectra not only have increased the bandwidth but also have changed significatively its shape. The profile spectrum for the convective mixing at the depth of 0.8 m reflects that medium-size scales have the most vigor, resulting a conspicuous peak at this range of scales. Ebert et al. (1989) obtained similar results with LES measurements for a well-developed convective atmospheric boundary layer.

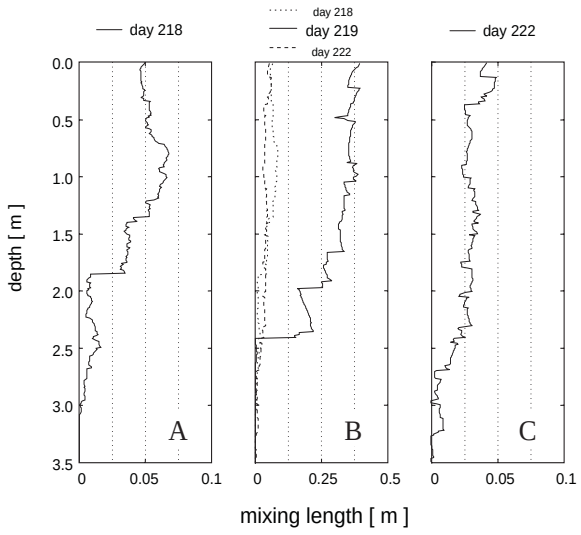


Figure 4.23: *Computed mixing length for low-wind interval (A,C) and convective-mixing interval (B). For comparison, low-wind mixing intensity profiles are also plotted in (B) as dotted and dash-dotted lines.*

### Mixing length

The computed mixing length (figure 4.23) is according with the mixing activity, yielding a much grater values for the convective-mixing interval. As it will show in the following subsection, a more informative characterization is obtained when mixing lengths are segregated for computing the parameters related with anisotropy.

### Anisotropy processes

Different anisotropy parameters have been computed in order to reveal the differences when mixing is induced by convection.

Figure 4.24 shows the profiles corresponding to the upward-downward mixing lengths and upward-downward fraction of water from source level (eq 4.27, 4.28, 4.23 and 4.24) computed from the three transilient matrix.

From the obtained results it is clear that during the convective regime, mixing was not only much stronger but also presented the highest asymmetries associated to anisotropy.

Another measurement to highlight the asymmetries derived from convection is by comparing the differences between the mixing lengths considering the depth level as a sink (eq 4.25, 4.26) or as a source (eq 4.23, 4.24).

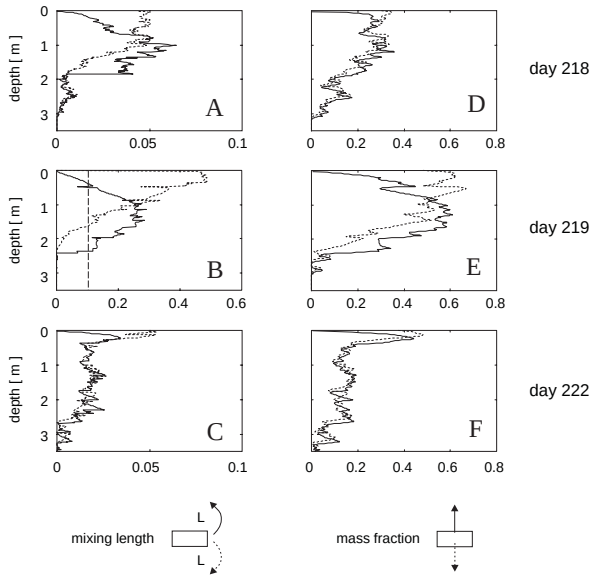


Figure 4.24: *Upward and downward mixing length (A,B,C) and fraction of water (D,E,F) from source level corresponding to the three sampling periods. For comparison, the vertical dashed line in (B) indicates the scale range in (A) and (C).*

Figure (4.25) shows the different result obtained. The main differences can be observed again on the profiles obtained from the convective transilient matrix.

### Comparison with LES simulation

The previous analysis indicate that the results obtained with the proposed parameterization seems to be according, at least from the qualitative point of view, with those expected from the measured meteorological conditions and the temperature profiles.

In order to verify up to which point the numerical results are valid, alternative analysis should be developed for comparison.

As it has been mentioned in the previous chapter, the surface boundary layer of a water body could be considered an upside-down atmospheric boundary layer, especially when the wind velocity is low. For this reason, and as a first approach, the results obtained from LES simulation by Ebert et al. (1989) can be used to compare the results obtained from the transilient

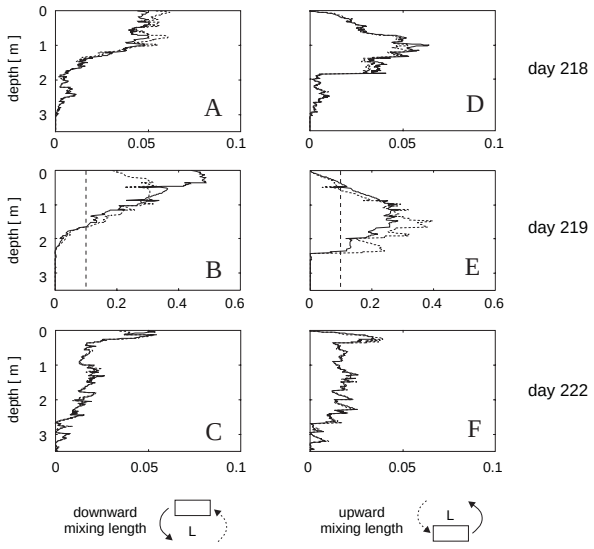


Figure 4.25: *Downward mixing length (A,B,C) and upward mixing legnths (D,E,F) segregating whend the depth parcel is considered a source (solid line) or a sink (dotted line). As mixing lengths corresponding to the convective regime (B,E) are much greater, a vertical dashed line in (B,E) are plotted as the reference scale for the other sampling periods.*

matrix associated to the convective mixing. Although Ebert et al. (1989) simulated an idealized convective atmospheric boundary layer, it is reasonable to expect some similarities when comparing adimensional measurements due to the dynamic similarity of both processes.

Figure 4.26 shows the mixing lengths computed from the empirical proposed parameterization and the LES transilient matrix. For comparison, the profiles obtained in the LES simulation has plotted with the height axis positive downwards.

Some extra consideration should be taking into account in this comparison. The LES simulation allows computing the transilient matrix at different time references, obtaining the evolution of the convective mixing process. The transilient matrix obtained empirically with microstructure measurements is an statistical average of the transilient coefficients, which can be modified significatively during the sampling period, due to the non-stationarity of the mixing process. In order to compare the simulation with the experimental parameterization, it has been considered that convection was fully developed

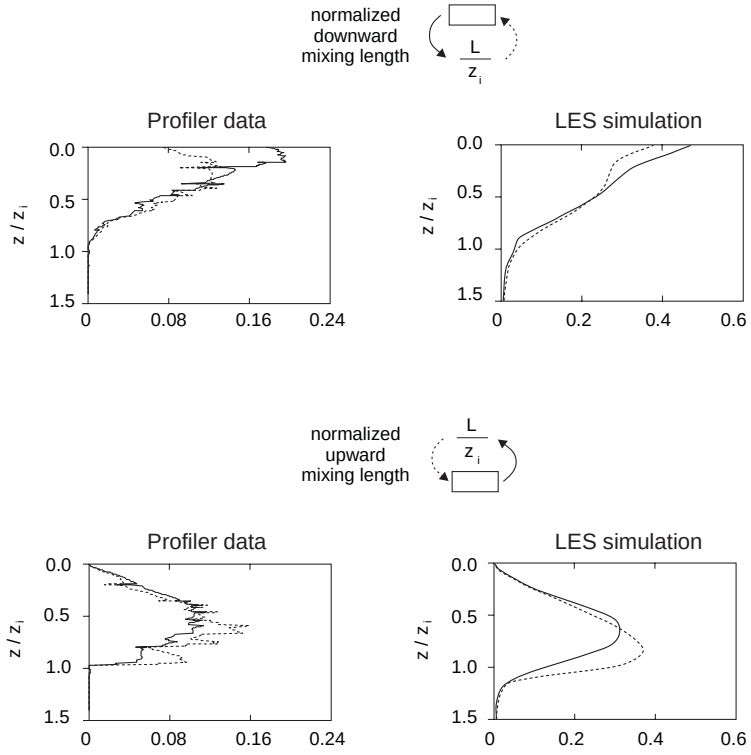


Figure 4.26: *Normalized upward mixing length (A,B) and downward mixing legnths (C,D) computed from the proposed parameterization of the transsilent matrix, and those obtained from the LES model computed from Ebert et al. (1989).*

during the sampling period, and the LES transilient matrix simulated at the characteristic convective time (t*) has been chosen as the reference for testing the computed results. The mixing lengths have been normalized using the mixing depth layer for the microstructre measurements (2.4 m) and the inversion height (1600 m) for the LES values. Comparing the profiles it is possible to observe that the final structures in both cases are very similar.

This result seems to indicate that it is possible to obtain reliable transilient coefficients from the proposed empirical parameterization.

### 4.4.3 Summary and conclusions

In this chapter a new parameterization of non-local mixing model is proposed. The main advantage on using non-local mixing models is the capability of describing all the potential mixing phenomena, which it is not possible with the local mixing models. However, non-local mixing models have not been widely used because their higher complexity and the difficulty for obtaining reliable parameterization.

The new proposed parameterization is based on empirical data obtained from microstructure profilers. This parameterization allows estimating the coefficients for the transilient matrix, the discrete descriptor used in the non-local mixing model.

The proposed method has been applied to two different field campaigns. The final results seems to indicate that the estimated transilient coefficients, and the different mixing parameters obtained from them, are in accordance with those expected from the background external forcing and observed thermal structure in each case.

The transilient matrix is a powerful descriptor that allows integrating the effects of mixing into ecological models. It is possible to forecast the effects of dispersion derived from turbulent mixing from the estimated transilient matrix.

The new parameterization provides a new approach to contrast the results obtained in theoretical models with empirical data obtained from field measurements.

# Chapter 5

# Synthesis and outlook

## 5.1 Synthesis

As synthetic conclusions, the three questions proposed at the beginning of this thesis are answered:

*How can we detect the turbulent patches from the microstructure measurements?*

The proposed method of wavelet-denoising and data classification based on local gradient has shown to be globally applicable and very robust for the identification of turbulent patches.

*Which are the most relevant properties of the turbulent patches?*

The vertical size of the patches ($L_p$) and the distribution properties of the Thorpe displacement within the patch - normalized Shannon entropy ($S_n$) and maximum displacement ($L_{Tmax}$) - has been considered the most relevant information for turbulent patch characterization. A new hydrodynamic diagram based on $L_p$ and the ratio $L_{Tmax}/L_p$ (which provide analog information to $S_n$) has proposed. This hydrodynamic diagram has been used for characterizing the response to a wind burst. This process has proposed as a new geophysical example for discussing the evolution of the turbulent processes. The results obtained have shown that the new hydrodynamic diagram provide detailed information about the evolution of this process.

*What kind of synoptic parameters could reflect the occurrence and properties of the turbulent patches?*

The transilient matrix has been considered the synoptic parameter that reflects the occurrence and properties of the turbulent patches in a selected interval of time. The transilient matrix represents the discrete version of the non-local mixing theory, which has been used as a theoretical framework. The coefficients of the transilient matrix have been parameterized from the topological properties of the turbulent patches (the vertical size Lp and the distribution of the Thorpe displacement within the patch).

Contrary to the approach followed by most of the works revised, the final method for describing the synoptic properties of the turbulent process does not take into account the estimated values of the turbulent dissipation rate.

Since the theoretical results reported by Kolmogorov (1941), the turbulent dissipation rate has been considered one of the key parameters to characterize the turbulence. Instrumental and methodological improvements for increasing the accuracy on eps estimates is still one of the main goals in the research on environmental turbulence.

However, there are some methodological restrictions that are especially important when field measurements are carried out with microstructure profilers. Field observations have shown the high spatial (Imberger, 1986 ) and temporal ( Agrawal et al., 1995) variability of the turbulent dissipation rate. Describing the dynamics of the turbulence based on this parameter requires then measurements with high resolution both in time and space. Microstructure profilers have been designed for high spatial resolution measurements, but there is an inherent limitation for obtaining profiles at very short intervals of time. Statistical inference is the only method that can be used for the final description of the process, but it is necessary to assume some physical and statistical properties which have been one of the main issues of debate during last years.

The debate is open and the questions related to it seem that will not be completely answered soon. May be future new technologies (as high resolution acoustic tomography, underwater sonic or light detection and ranging systems, high resolution laser doppler velocimeters ... who knows what else? ) would be able to measure the turbulent dissipation rates with enough spatial and temporal resolution for accurate description of the turbulence dynamics in the field.

With the present methodological restrictions in mind, it has been considered that topological measurements, which integrate the different events

of the dynamical process, can provide better synoptic descriptions. As integrating parameters, the temporal scales associated to structural properties are much larger than those associated to dynamical properties. Therefore, the frequency sampling requirements are not so restrictive for the topological approach.

However, there are some limitations when describing the process from topological measurements: we loose some details of the dynamics behind the structure. Although it can be an important restriction for some fields of research, many studies related to biology will not be seriously affected by this limitation, as organisms also responds as elements of integration.

## 5.2 Future perspectives

A wide range of potential applications can be derived from this type of description. The transilient matrix estimates the probability of mass exchange between different layers, information that can be directly applied in one-dimensional discrete mixing models.

Numerical models can take benefit from this type of descriptor that can provide more realistic transport estimates than those based only on local mixing. It is known that diffusion can be key parameter in some models of spatial patterns. Theoretical approaches of modeling spatial dynamics can obtain information from this method that can be used to contrast their theoretical results.

The transilient matrix may provide a more realistic descriptor of the environmental mixing. It can be used as a framework reference to understand some particular observation of environmental measurements: the presence or absence of some particular planktonic species, the increasing or decreasing of some population of interest, or the spatial distribution and the temporal changes of plankton communities.

This approach opens new perspectives to understand how turbulence may affect some ecological processes. The quantification of vertical mixing anisotropy (that it is possible with this new method) may help in understanding the changes of the light field in aquatic environments. Underwater light do not change linearly in depth so, even relative small differences between downward and upward mixing may be significant from the physiological point of view. This may have strong implications in dynamical models of photochemistry and photobiology like photosynthetic production or UV photodamage.

Furthermore, the parameters derived from the transilient matrix can be used as synoptic descriptors of the turbulence in some standard ecological

analyses. Maybe in the future it is accepted that the mixing intensity profile can be used as alternative environmental factor, and it used in statistical analysis like other environmental variables as, for example, temperature, alkalinity or underwater irradiance.

Physical applications can take benefit also from this complementary approach. It has been shown in chapter 4 that some of the final descriptors could be directly compared with the output of numerical mixing models. That allows verifying some results obtained from the numerical models directly with those obtained experimentally in the field. The transilient matrix may provide alternative estimators of diapycnal fluxes that can be used on different transport models.

Hopefully, improvements of this new method and the applications derived from them will arise in the future. There are still, some questions to be answered. The final transilient matrix is estimated as the average of transilient matrixes computed from single $d_T$ profiles. Which is the proper time scale for averaging? Which is the minimum number of profiles for computing a robust transilient matrix? In which cases this type of approximation is not valid? Probably the answer of these questions will be a function of the particular application and the particular process to be characterized. In any case, it is expected that this new method will become a useful tool for the research of physical and biological interactions at small scales.

# Appendix A

# Thermodynamic parameters

Microstructure analysis requires to compute some thermodynamic properties of the water. In this work it has been developed a Matlab toolbox, which contain a set of routines for computing some thermodynamic properties of freshwater.

Some functions are based on the SEAWATER Library (V 1.2d, Phillip P. Morgan, CSIRO). SEAWATER is a toolbox of Matlab routines for calculating the thermodynamic properties of sea water. Freshwater adaptation has been done following Chen and Millero (1986) and Wüest et al. (1996).

## A.1 Salinity

Salinity of fresh water $S_F$ has been computed as (Chen and Millero, 1986)

$$S_F = 1.00488\ S_W \tag{A.1}$$

where $S_W$ is the practical salinity for sea water, computed as (UNESCO, 1981):

$$\begin{aligned} S_W &= a(R_t) + \Delta S && \text{(A.2)} \\ a(R_t) &= a_0 + a_1\ R_t^{1/2} + a_2\ R_t + a_3\ R_t^{3/2} + a_4\ R_t^2 + a_5\ R_t^{5/2} && \text{(A.3)} \end{aligned}$$

where

$$\begin{aligned} \Delta S &= \frac{(T-15)}{1 + k_1\ (T-15)}\ b(R_t); && \text{(A.4)} \\ b(R_t) &= b_0 + b_1\ R_t^{1/2} + b_2\ R_t + b_3\ R_t^{3/2} + b_4\ R_t^2 + b_5\ R_t^{5/2} && \text{(A.5)} \end{aligned}$$

and the constant values:

$$
\begin{array}{lll}
a_0 = 0.0080 & b_0 = 0.0005 & k_1 = 0.0162 \\
a_1 = -0.1692 & b_1 = -0.0056 & \\
a_2 = 25.3851 & b_2 = -0.0066 & \\
a_3 = 14.0941 & b_3 = -0.0375 & \\
a_4 = -7.0261 & b_4 = 0.0636 & \\
a_5 = 2.7081 & b_5 = -0.0144 &
\end{array}
$$

$R_t$ is the ratio between conductivity at *in situ* temperature $T$, and conductivity at the same temperature and practical salinity of 35 (in both case $p = 1$ atm.). The ratio $R_t$ is computed as:

$$R_t = \frac{C_{(S,T,p)}}{K_S \; r_t \; R_p} \tag{A.6}$$

where $K_S = 4.29140 \; S/m$, is the conductivity of standard marine water at $S = 35$, $T = 15 \; ^oC$ and $p = 0$ ( $p$ is the pressure in bar over standard atmosphere), and

$$R_P = 1 + \frac{p \; (e_1 + e_2 \; p + e_3 \; p^2)}{1 + d_1 \; T + d_2 \; T^2 + (d_3 + d_4 \; T) \frac{C}{K_S}} \tag{A.7}$$

$$
\begin{array}{ll}
e_1 = 2.070 \; 10^{-4} & d_1 = 3.426 \; 10^{-2} \\
e_2 = -6.370 \; 10^{-8} & d_2 = 4.464 \; 10^{-4} \\
e_3 = 3.989 \; 10^{-12} & d_3 = 4.215 \; 10^{-1} \\
 & d_4 = -3.107 \; 10^{-3}
\end{array}
$$

$$r_t = c_0 + c_1 \; T + c_2 \; T^2 + c_3 \; T^3 + c_4 \; T^4 \tag{A.8}$$

$$
\begin{array}{ll}
c_0 = 0.6766097 & c_3 = -6.9698 \; 10^{-7} \\
c_1 = 2.00564 \; 10^{-2} & c_4 = 1.0031 \; 10^{-9} \\
c_2 = 1.104259 \; 10^{-4} &
\end{array}
$$

### A.1.1 Partial derivatives of salinity

As freshwater salinity has been computed as a proportional value of seawater salinity(eq. A.1), partial derivatives can be computed as:

$$
\begin{aligned}
\frac{\partial S_F}{\partial T} &= 1.00488 \; \frac{\partial S_W}{\partial T} \\
\frac{\partial S_F}{\partial C} &= 1.00488 \; \frac{\partial S_W}{\partial C} \\
\frac{\partial S_F}{\partial p} &= 1.00488 \; \frac{\partial S_W}{\partial p}
\end{aligned} \tag{A.9}
$$

Seawater partial derivatives are computed from eq. A.2 to eq. A.8.

**Respect temperature**

$$\frac{\partial S_W}{\partial T} = \frac{\partial \Delta S}{\partial T} + \frac{\partial a\,(R_t)}{\partial R_t}\frac{\partial R_t}{\partial T} \tag{A.10}$$

$$\frac{\partial a\,(R_t)}{\partial R_t} = \frac{1}{2}a_1\ R_t^{-1/2} + a_2 + \frac{3}{2}a_3\ R_t^{1/2} + 2a_4\ R_t + \frac{5}{2}a_5\ R_t^{3/2} \tag{A.11}$$

$$\frac{\partial R_t}{\partial T} = -\frac{C}{K_S}\left(\frac{1}{r_t}\frac{\partial r_t}{\partial T} + \frac{1}{R_p}\frac{\partial R_p}{\partial T}\right) \tag{A.12}$$

$$\frac{\partial r_t}{\partial T} = c_1 + 2\ c_2\ T + 3\ c_3\ T^2 + 3\ c_4\ T^3 \tag{A.13}$$

$$\frac{\partial R_p}{\partial T} = -\frac{p\ \ (e_1 + e_2\ p + e_3\ p^2)\ \ \left(d_1 + 2\ d_2\ T^2 + d_4\ \frac{C}{K_S}\right)}{\left(1 + d_1\ T + d_2\ T^2 + (d_3 + d_4\ T)\ \frac{C}{K_S}\right)^2} \tag{A.14}$$

$$\frac{\partial \Delta S}{\partial T} = \frac{\partial X}{\partial T}\ b(R_t) + \frac{\partial b(R_t)}{\partial T}\ X \tag{A.15}$$

where

$$X = \frac{(T-15)}{1 + k_1\ \ (T-15)} \tag{A.16}$$

$$\frac{\partial X}{\partial T} = \frac{1}{(1 + k_1\ \ (T-15))^2} \tag{A.17}$$

$$\frac{\partial b(R_t)}{\partial T} = \frac{\partial b(R_t)}{\partial R_t}\frac{\partial R_t}{\partial T} \tag{A.18}$$

$$\frac{\partial b\,(R_t)}{\partial R_t} = \frac{1}{2}b_1\ R_t^{-1/2} + b_2 + \frac{3}{2}b_3\ R_t^{1/2} + 2\ b_4\ R_t + \frac{5}{2}b_5\ R_t^{3/2} \tag{A.19}$$

**Respect conductivity**

$$\frac{\partial S_W}{\partial C} = \frac{\partial \Delta S}{\partial C} + \frac{\partial a\,(R_t)}{\partial R_t}\frac{\partial R_t}{\partial C} \tag{A.20}$$

$$\frac{\partial R_t}{\partial C} = -\frac{C}{K_S\ r_t\ R_p}\left(1 - \frac{C}{R_p}\frac{\partial R_p}{\partial C}\right) \tag{A.21}$$

$$\frac{\partial R_p}{\partial C} = -\frac{p\ \ (e_1 + e_2\ p + e_3\ p^2)\ \ (d_3 + d_4\ T)}{K_S^2\ \ \left(1 + d_1\ T + d_2\ T^2 + (d_3 + d_4\ T)\ \frac{C}{K_S}\right)^2} \tag{A.22}$$

**Respect pressure**

$$\frac{\partial S_W}{\partial p} = \frac{\partial \Delta S}{\partial p} + \frac{\partial a\,(R_t)}{\partial R_t}\frac{\partial R_t}{\partial p} \tag{A.23}$$

$$\frac{\partial R_t}{\partial p} = -\frac{C}{K_S\ r_t\ R_p^2}\frac{\partial R_p}{\partial p} \tag{A.24}$$

$$\frac{\partial R_p}{\partial p} = -\frac{e_1 + 2\ e_2\ p + 3\ e_3\ p^2}{1 + d_1\ T + d_2\ T^2 + (d_3 + d_4\ T)\ \frac{C}{K_S}} \tag{A.25}$$

$$\frac{\partial \Delta S}{\partial p} = X\ \frac{\partial a\,(R_t)}{\partial R_t}\frac{\partial R_t}{\partial p} \tag{A.26}$$

## A.2 Density

Following Chen and Millero (1986) density $\rho_p\ [kg\ m^{-3}]$ is computed as:

$$\rho_p = \frac{\rho_0}{1 - \frac{p}{K}} \tag{A.27}$$

where $\rho_0$ is the density at the surface water (hydrostatic pressure =0), computed as:

$$\begin{aligned} \rho_0 \;=\; & a_0 + a_1\ T + a_2\ T^2 + a_3\ T^3 + a_4\ T^4 + a_5\ T^5 \\ & + a_6\ T^6 + \left(b_0 + b_1\ T + b_2\ T^2\right)\ S_F \end{aligned} \tag{A.28}$$

and the constant values:

$$\begin{array}{ll} a_0 = 0.999835 & b_0 = 8.181\ 10^{-4} \\ a_1 = 6.7914\ 10^{-5} & b_1 = -3.85\ 10^{-6} \\ a_2 = -9.0894\ 10^{-6} & b_2 = 4.98\ 10^{-8} \\ a_3 = 1.0171\ 10^{-7} & \\ a_4 = -1.2846\ 10^{-9} & \\ a_5 = 1.1592\ 10^{-11} & \\ a_6 = -5.0125\ 10^{-14} & \end{array}$$

$$K(bar) = K_w + A_F\ p + B_F\ S_F \tag{A.29}$$

$$K_w = c_0 + c_1\ T + c_2\ T^2 + c_3\ T^3 + c_4\ T^4 \tag{A.30}$$

$$A_F = d_0 + d_1\ T + d_2\ T^2 \tag{A.31}$$

$$B_F = e_0 + e_1\ T + e_2\ p \tag{A.32}$$

$c_0 = 19652.17$ $d_0 = 3.2726$ $e_0 = 53.238$
$c_1 = 148.113$ $d_1 = -2.147\ 10^{-4}$ $e_1 = -0.313$
$c_2 = -2.293$ $d_2 = 1.128\ 10^{-4}$ $e_2 = 5.728\ 10^{-3}$
$c_3 = 1.256\ 10^{-2}$
$c_4 = -4.18\ 10^{-5}$

### A.2.1 Partial derivatives of density

Density partial derivatives have been computed from eq. A.27 to eq. A.32

**Respect temperature**

$$\frac{\partial \rho_p}{\partial T} = C_1 \frac{\partial \rho_0}{\partial T} - C_2 \frac{\partial K}{\partial T} \tag{A.33}$$

where $C_1$ and $C_2$ are:

$$C_1 = \frac{1}{1 - \frac{p}{K}} \tag{A.34}$$

$$C_2 = \frac{{C_1}^2 \rho_0 p}{K^2} \tag{A.35}$$

$$\begin{aligned} \frac{\partial \rho_0}{\partial T} &= a_1 + 2\ a_2\ T + 3\ a_3\ T^2 + 4\ a_4\ T^3 + 5\ a_5\ T^4 \\ &\quad +6\ a_6\ T^5 + (b_1 + 2\ b_2\ T)\ S_F \end{aligned} \tag{A.36}$$

$$\frac{\partial K}{\partial T} = \frac{\partial Kw}{\partial T} + \frac{\partial A_F}{\partial T}\ p + \frac{\partial B_F}{\partial T}\ S_F \tag{A.37}$$

$$\frac{\partial Kw}{\partial T} = c_1 + 2\ c_2\ T + 3\ c_3\ T^2 + 4\ c_4\ T^3 \tag{A.38}$$

$$\frac{\partial A_F}{\partial T} = d_1 + 2\ d_2\ T \tag{A.39}$$

$$\frac{\partial B_F}{\partial T} = e_1 \tag{A.40}$$

**Respect salinity**

$$\frac{\partial \rho_p}{\partial S} = C_1 \, \frac{\partial \rho_0}{\partial S} - C_2 \, \frac{\partial K}{\partial S} \tag{A.41}$$

$$\frac{\partial \rho_0}{\partial S} = b_0 + b_1 \, T + b_2 \, T^2 \tag{A.42}$$

$$\frac{\partial K}{\partial S} = B_F \tag{A.43}$$

**Respect pressure**

$$\frac{\partial \rho_p}{\partial p} = C_2 \, \left( \frac{K}{p} - \frac{\partial K}{\partial p} \right) \tag{A.44}$$

$$\frac{\partial K}{\partial p} = A_F + \frac{\partial B_F}{\partial p} \, S_F \tag{A.45}$$

$$\frac{\partial B_F}{\partial p} = e_2 \tag{A.46}$$

## A.3 Specific heat

The of specific heat value at constant pressure $c_p$ $[J \; g^{-1} \; {}^oC^{-1}]$ is computed as:

$$\begin{aligned} c_p \;\; = \;\; & a_0 + a_1 \, T + a_2 \, T^2 + a_3 \, T^3 + a_4 \, T^4 + \\ & + \left( b_0 + b_1 \, T + b_2 \, T^2 \right) \, S_F + \\ & + \left( c_0 + c_1 \, T + c_2 \, T^2 + \, d_0 \, S_F \right) p + e_0 \, p^2 \end{aligned} \tag{A.47}$$

and the constant values:

| | | |
|---|---|---|
| $a_0 = 4.2174$ | $b_0 = -6.616 \; 10^{-5}$ | $c_0 = -4.917 \; 10^{-4}$ |
| $a_1 = -3.6608 \; 10^{-3}$ | $b_1 = 9.28 \; 10^{-6}$ | $c_1 = 1.335 \; 10^{-5}$ |
| $a_2 = 1.3129 \; 10^{-4}$ | $b_2 = -2.39 \; 10^{-8}$ | $c_2 = -2.177 \; 10^{-7}$ |
| $a_3 = -2.21 \; 10^{-6}$ | | $d_0 = 3.441 \; 10^{-6}$ |
| $a_4 = 1.508 \; 10^{-8}$ | | $e_0 = 1.5 \; 10^{-7}$ |

## A.4 Thermal expansibility

The thermal expansibility $\alpha$ [ $^oC^{-1}$] is computed as:

$$\begin{aligned} 10^6\ \alpha \;\; = \;\; & a_0 + a_1\ T + a_2\ T^2 + a_3\ T^3 + a_4\ T^4 + a_5\ T^5 \\ & + \left(b_0 + b_1\ T + b_2\ T^2\right)\ S_F + \\ & + \left(c_0 + c_1\ T + c_2\ T^2 + \ d_0\ S_F\right) p \end{aligned} \qquad \text{(A.48)}$$

and the constant values:

$a_0 = -68.0$ $\quad b_0 = -4.599$ $\quad d_0 = -4.613\ 10^{-2}$
$a_1 = 18.2091$ $\quad b_1 = -0.1999$
$a_2 = -0.30866$ $\quad b_2 = 2.79\ 10^{-3}$
$a_3 = 5.3445\ 10^{-3}$ $\quad c_0 = 0.3682$
$a_4 = -6.0721\ 10^{-5}$ $\quad c_1 = -1.52\ 10^{-2}$
$a_5 = 3.1441\ 10^{-7}$ $\quad c_2 = 1.91\ 10^{-4}$

# Appendix B

# Density fluctuation error

Density fluctuation error $E_{\rho'}$ has been computed considering that density error $E_\rho$ and monotonic density error $E_{\rho_m}$ follows a normal distribution:

$$\begin{aligned} E_\rho &\sim N(\mu_{\rho e}, \sigma_{\rho e}) \\ E_{\rho_m} &\sim N(\mu_{\rho_m e}, \sigma_{\rho_m e}) \end{aligned} \tag{B.1}$$

As $E_{\rho'}$ is computed as the difference between density and monotonic profiles, the associated error will follow a normal distribution $E_{\rho'} \sim N(\mu_{\rho' e}, \sigma_{\rho' e})$. Following Sokal (1995) the mean and the variance of the distribution can be computed as

$$\begin{aligned} \mu_{\rho' e} &= \mu_{\rho e} - \mu_{\rho_m e} \\ \sigma^2_{\rho' e} &= \sigma^2_{\rho e} + \sigma^2_{\rho_m e} - 2\ r\ \sigma_{\rho e}\ \sigma_{\rho_m e} \end{aligned} \tag{B.2}$$

Mean values $\mu_{\rho e}$ and $\mu_{\rho_m e}$ depends on systematic errors of density measurements. Considering that systematic error in both measurements is equal

$$\mu_{\rho e} \approx \mu_{\rho_m e} \Rightarrow \mu_{\rho' e} = 0 \tag{B.3}$$

On computing variance, it should be necessary estimating $r$, the parametric correlation coefficient between $E_{\rho'}$ i $E_\rho$ but it can be neglected because the correlation between both parameters, if exist, must be very small. It is also reasonable to consider $\sigma^2_{\rho e} \gg \sigma^2_{\rho_m e}$ as, it was mentioned before, the first parameter is computed from a single value, while the second is computed from a set of values and its error must be much lower. The final distribution for density fluctuation error can be then assumed as:

$$E_{\rho'} \sim N(0, \sigma_{\rho e}) \tag{B.4}$$

In this case it is only necessary to estimate the variance on density error $\sigma_{\rho e}$ for characterizing $E_{\rho'}$.

Density is not a direct field measurement. The density values are estimated from a specific state equation that relates density with temperature, pressure and salinity (or conductivity). Gregg (1979) estimated the variance of the error in density $\sigma^2_{\rho e}$, due to electronic and quantification error, as

$$\begin{aligned}
\sigma^2_{\rho e} &= \sigma^2_T \left(\frac{\partial \rho}{\partial T}\right)^2 + \sigma^2_P \left(\frac{\partial \rho}{\partial P}\right)^2 + \sigma^2_S \left(\frac{\partial \rho}{\partial S}\right)^2 = \qquad \text{(B.5)} \\
&= \sigma^2_T \left[\left(\frac{\partial \rho}{\partial T}\right)^2 + \left(\frac{\partial S}{\partial T}\right)^2 \left(\frac{\partial \rho}{\partial S}\right)^2\right] + \\
&\quad + \sigma^2_P \left[\left(\frac{\partial \rho}{\partial P}\right)^2 + \left(\frac{\partial S}{\partial P}\right)^2 \left(\frac{\partial \rho}{\partial S}\right)^2\right] + \\
&\quad + \sigma^2_C \left(\frac{\partial S}{\partial C}\right)^2 \left(\frac{\partial \rho}{\partial S}\right)^2
\end{aligned}$$

where $\rho$ is density, $S$ salinity, $T$ is temperature, $C$ is conductivity and $\sigma^2_S$, $\sigma^2_T$, $\sigma^2_C$, $\sigma^2_P$ are the noise variance of salinity, temperature conductivity and pressure respectively.

Noise variance can be estimated from experimental test with the microstructure equipment and the different partial derivatives in B.5 depend of the state equation used the density computation. It is necessary then to specify the state equation of density and determine the instrumental features of the microstructure profiler.

## B.1 Instrumental error

Some of the laboratory tests developed at the Centre of Water Research (in Luketina, 1986) have been used as the error reference for estimating the noise variance of the field measurements.

Luketina (1986) reported that temperature, conductivity and pressure measurements were limited by quantification, which implied that the noise contribution for the electronics and the sensors were lower than the error derived from the conversion of analog to digital data. Following Otnes and Enochson (1972) the noise variance is given by:

$$\sigma^2_N = \frac{(E\ 2^{-n})^2}{12} \qquad \text{(B.6)}$$

where $E$ is the full scale range and $n$ the number of the bits used in the analog-digital conversion

Microstructure signals are usually digitized with 16 bit converters.. Substituting on eq. B.6 the values of $n = 16$, full temperature scale range $E_T = 25\ ^oC$ full pressure scale range $E_p = 10\ bar$, we obtain a temperature variance error of $\sigma_T^2 = 4.23\ 10^{-9}\ ^oC^2$ and pressure variance error of $\sigma_p^2 = 1.94\ 10^{-9}\ bar^2$.

Estimating conductivity variance error is a more complex as the range scale is highly variable. The value of $\sigma_C^2$ was estimated from laboratory test, developed by Geoff Carter at the CWR (Luketina, 1986), obtaining a final value of $\sigma_C^2 = 4.9\ 10^{-9}\ S^2\ m^{-2}$.

## B.2 Error estimating from numerical simulation

Partial derivatives of $\partial\rho/\partial T$, $\partial\rho/\partial S$ and $\partial\rho/\partial p$, required to compute B.5, depend on environmental conditions. A set of theoretical backgrounds were simulated, with different values of temperature (ranging from 5 to 25 $^oC$), conductivity (from $2\ 10^{-4}$ to $8\ 10^{-3}\ \ S\ m^{-1}$) and pressure ( from 0 to 5 $bar$). The potential range of $\sigma_{\rho e}^2$ was estimated from the variance errors $\sigma_C^2$, $\sigma_T^2$, $\sigma_P^2$ and different values for the partial derivatives $\partial\rho/\partial T$, $\partial\rho/\partial S$, $\partial\rho/\partial p$.

Finally, the error of density fluctuations $E_{\rho'}$ was computed as $1.65\,\sigma_{\rho e}$. This value corresponds to the percentile 95 of the distribution $N(0, \sigma_{\rho e})$(i.e. 95% of the potential error values are smaller than $E_{\rho'}$).

Different numerical test were developed, concluding that nominal values of pressure and conductivity do not change significantly the final estimation of $E_{\rho'}$. The most sensitive parameters corresponded to $\sigma_T^2$ , $\sigma_C^2$ and changes on nominal temperature $T$.

Figure B.1 shows the final simulation for estimating $E_{\rho'}$. The error was plotted varying $\sigma_T^2$ and $\sigma_C^2$.

Vertical dotted line indicates the final value considered for $\sigma_T^2$ , which corresponds to the quantification error for 16 bits A/D conversion. Point $A$ represents the estimated value:

$$E_{\rho'} = 2.5\ 10^{-4}\ kg\ m^{-3} \tag{B.7}$$

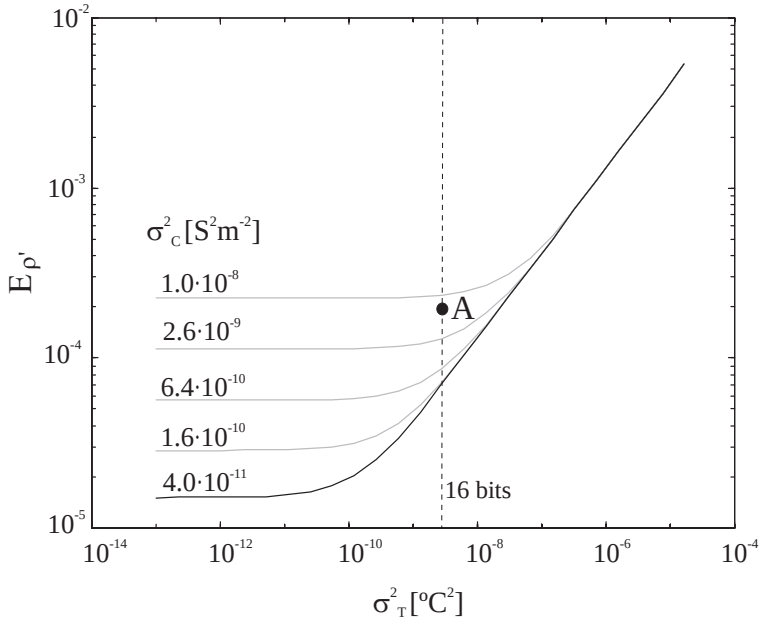


Figure B.1: *Density fluctuation error. The lines correspond to density errors associated to diferent conductivity errors. Vertical dotted line indicates the quantification error associated to 16 bits. The point (A) corresponds to the error assumed for MP microprofiler measurements.*

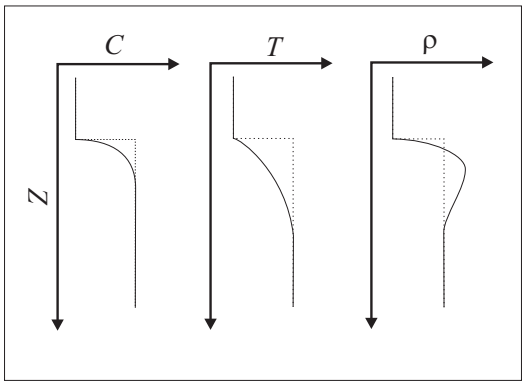


Figure B.2: *Example showing the effect of spiking density generated by the mismatch of time response from different sensors. The first two profiles represents an hypotetic case of two layer system. In this case there is a sharp gradient of temperature and conductivity (doted line). In this example the time response of the temperature sensor is much slower.*

## B.3 Error on density estimation. Final considerations

Additional factors may increase the uncertainty, and then, the value of $E_{\rho'}$. The static calibration and the dynamic response of the different errors are two examples of potential sources of error that should be taken into account.

**Sensor calibration** Static calibration is the routine for obtaining the transfer function for raw data to physical units conversion. There is always an inherent error in the calibration function that can increase the value of $E_{\rho'}$. In this work, however, it has been considered that this type of error corresponds to systematic errors and affects the exactitude of the measurement, but do not affect significantly the resolution, and the contribution to $E_{\rho'}$ have been neglected.

**Dynamical response of sensors** Dynamical response represents an additional factor of inacuracy, mainly derived from the slow instrument response time, and spurious peaks in the data (known as spiking) due to a mismatch in the response characteristic of the sensors (fig B.2). An exhaustive review of this phenomenon, well kowkn in oceanographic research, was done by Horne and Toole (1980).

Several techniques of signal processing has been developed in order to

reduce the effect of dynamic response. Fofonoff *et al.* (1974) design specific filters for the temperature and conductivity signals in order to eliminate the spikes on computed density and salinity. Caldwell and Dillon (1981) improved a thermistor response by correcting its spectrum. Gregg and Hess (1985) used Legendre polynomials to accurately approximate the transfer function of a sensor in frequency space.

Fozdar *et al.* (1985) used a technique of recursive filter in the time domain, sharpening and matching response time for temperature and conductivity. The method allows direct calculation of salinity and density, an thus offers a significant advantage over other methods. However, Vollmer (1991) applied the method proposed by Fozdar *et al.* (1985) and found that the response time varied widely for different individual sensors of the same model, and therefore the filtering had to be adapted. Vollmer (1991) concluded that the estimation of the response time constant should become a routine calibration procedure for every individual sensor, which is not a trivial task.

Taking into account the potential uncertainties on $E_{\rho'}$ a factor of 50% and 100% of increased values had considered in noise sensitivity tests (sections 2.4.1and 2.5.1)

# Bibliography


Agrawal, Y. C.; Terray, E. A.; Donelan, M. A.; *et al.* (1992). *Enhanced dissipation of kinetic energy beneath surface waves.* Nature. 359: 219-233.

Allen, H.J.; Perkins, E.W. (1952). *A study of effects of flow over slender inclined bodies of revolution.* Report No. 1048, U.S. National Advisory Committee for Aeronautics.

Anis, A.; Moum,J. N. (1992). *The superadiabatic surface layer of the ocean during convection.* J. Phys. Oceanogr. 22: 1221-1227.

Anis, A.; Moum,J. N. (1995). *Surface wave-turbulence interactions: scaling epsilon near the sea surface.* J. Phys. Oceanogr. 25: 2025-2045.

Batchelor, G. K. (1959). *Small-scale variation of convected quantities like temperature in turbulent fluid.* J. Fluid Mech. 5: 113-139.

Baumert, H.; Peters, H. (2000). *Second-moment closures and length scales for weakly stratified turbulent shear flows.* J. Geophys. Res. 105: 6453-6468.

Boudreau, B.P.; Imboden, D.M. (1987) *Mathematics of tracer mixing in sediments: III. The theory of nonlocal mixing within sediments.* Am. Jour. Sci. 287: 693-719.

Bourassa, M.A. (2000). *Shear stress model for the aqueous boundary layer near the air-sea interface.* J. Geophys. Res. Vol 105 C1 : 1167-1176.

Brainerd, K. E.; Gregg, M. C. (1993). *Diurnal restratification and turbulence in the oceanic mixed layer: 1. Observation.* J. Geophys.Res. 98: 22645-22656.

Caldwell, D. R. ( 1983). *Oceanic turbulence: big bangs or continuous creation.* J. Geophys. Res., 88: 7543-7550.

Caldwell, D. R.; Dillon, T. M.; Brubaker, J. M.; Newberger, P. A.; Paulson, C. A. (1980). *The scaling of vertical temperature gradient spectra.* J. Geophys. Res. Vol 85 C4 : 1917-1924.

Caldwell, D. R.; Chriss, T. M.; Newberger, P. A.; Dillon, T.M. (1981). *The thinness of oceanic temperature gradients.* J. Geophys. Res. 86, 4265-4268.

Carter, G.D.; Imberger, J. (1986) *Vertically rising microstructure profiler. J. Atmos. Oceanic Technol.* 3(3): 462-471.

Catalan, J. (1999). *Small-scales hydrodynamics as a framework for plankton evolution.* Jap. J. Limnol. 60: 469-490.

Cohen, A.; Daubechies, I.; Jawerth, B. ; Vial, P. (1993). *Multiresolution analysis, wavelets and fast wavelet transform on an interval.* Comptes Rendus Acad. Sci. Paris (A), 316: 417-421.

Corrsin, S. (1958). *Local isotropy in turbulent shear flow.* N.A.C.A. RM58B11.

Cullen,J.J.; Lewis,M.R. (1988). *The kinetics of algal photoadaptation in the context of vertical mixing.* J. Plankton Res. 10 (5):1039-1063.

Chen, C.T.; Millero, F.J. (1986). *Precise thermodynamic properties for natural waters covering only the limnological range.* Limnol. Oceanogr. 31 (3): 657 -662

Cowles, T.J.; Desiderio, R.A.; Neuer, S. (1993). *In situ characterization of phytoplankton from vertical profiles of fluorescence emission spectra.* Mar. Biol. 115:217-222.

Craig, P.D.; Banner, M.L. (1994). *Modeling wave-enhanced turbulence in the ocean surface layer.* J. Phys. Oceanogr. 24:2546-2558.

Crawford, W.R. (1986). *A Comparison of Length Scales and Decay Times of Turbulence in Stably Stratified Flows.* J. Phys. Oceanogr. 16: 1847-1854.

Crawford, W.R.; Dewey, R.K. (1990). *Confidence limits for friction velocities determined from turbulence profiles in coastal waters.* J. Atmos. Oceanic. Technol. 7:50-57.

Csanady, G.T. (1983). *The free surface turbulent shear layer.* J. Phys. Oceanogr. 14: 402-420.

Churchill, J.H.; Csanady, G.T. (1983). Near-surface measurements of quasi-Lagrangian velocities in open water. J. Phys. Oceanogr. 13: 1669-1680.

Daubechies, I. (1992) *Ten Lectures on Wavelets. CBMS-NSF Regional conference series in applied mathematics*, Vol. 61, S.I.A.M., 357 pp.

Davis, C.S.; Flierl, G.R.; Wiebe, P.H.; Franks, P.J.S. (1991). *Micropatchiness, turbulence and recruitment in plankton.* J. Mar. Res. 49:109-151.

Desiderio, R. A.; Cowles, T. J.; Moum, J. N.; Myrick, M. (1993). *Microstructure profiles of laser-induced chlorophyll fluorescence spectra.* J. Atmos. Oceanic Technol. 10: 209-224.

Denman,K.L.; Gargett, A.E. (1995). *Biological-Physical interactions in the upper ocean: The role of vertical and small scale transport processes.* Ann. Rev. Fluid Mech. Vol 27: 225-255.

Dewey, R.K.; Crawford, W.R. (1988). *Bottom stress estimates from vertical dissipation rate profiles on the continental shelf.* J. Phys. Oceanogr. 18: 1167-1177.

DeSilva, I.; Fernando, H.; Eaton, F. ; Hebert, D. (1996). *Evolution of Kelvin-Helmholtz billows in nature and laboratory.* Earth Planetary Sci. Lett. 143: 217-231.

Dillon, T. M. (1982). *Vertical Overturns: A Comparison of Thorpe and Ozmidov Length Scales.* J. Geophys. Res. Vol 87 C12 : 9601-9613.

Dillon, T. M. (1984). *The energetics of overturning structures: implications for the theory of fossil turbulence.* J. Phys. Oceanogr. 12: 541-549.

Dillon, T. M.; Richman, J. G.; Hansen, C. G.; Pearson, M. D. (1981). *Near-surface turbulence measurements in a lake.* Nature. 290: 390-392.

Dillon, T. M.; Caldwell, D. R. (1980). *The Batchelor spectrum and dissipation in the upper ocean.* J. Geophys. Res. 85: 1910-1916.

Donoho, D. L. (1995) *De-Noising by soft-thresholding.* IEEE Trans. On Inf. Theory, Vol 41(3): 613-627.

Donoho, D.L.; I.M. Johnstone (1994) *Ideal spatial adaptation by wavelet shrinkage.* Biometrika. 81: 425-455.

Donoho, D. L.; Johnstone, I.M. (1995). *Adapting to unknown smoothness via wavelet shrinkage.* J. Am. Stat. Assoc. 90 (432): 1200-1224.

Drennan, W. M.; Donelan, M. A.; Terray, E. A.; Katsaros, K. B. (1996). *Oceanic turbulence dissipation measurements in SWADE.* J. Phys. Oceanogr. 26: 808-815.

Ebert, E. E.; Schumann, U.; Stull, R. B. (1989) *Nonlocal Turbulent Mixing in the Convective Boundary Layer Evaluated from Large-Eddy Simulation.* J. Atmos. Sci. Vol 46: 2178-2207.

Ellison, T. H. (1957). *Turbulent transport of heat and momentum from an infinite rough plane.* J. Fluid. Mech. Vol 2: 456-466.

Etemad Shahidi, A.; Imberger, J. (2001). *Anatomy of turbulence in thermally startified lakes* Limnol. Ocenagr. 42(5): 1158-1170.

Ferris, J.M.; Christian, R. (1991). *Aquatic primary production in relation to microalgal responses to changing light: a review.*Aquat. Sci. 53:1015-1621.

Fofonoff, N. P.; Hayes, S. P.; Millard, R.C., Jr. (1974 *W.H.O.I./Brown CTD microprofiler: Methods of calibration and data handling.* WHOI Tech. Rep.WHOI-74-89; 65 pag.

Foufula-Georgiou, E.; Kumar, P. (Editors) - 1994). *Wavelets in geophysics.* Wavelet analysis and its applications (Vol 4). Charles K. Chui, Series Editor. Academic Press. 372 pag.

Fozdar, F. M.; Parker, G. J.; Imberger, J. (1985). *Matching temperature and conductivity sensor response characteristics.* J. Phys. Oceanogr. Vol 15: 1557-1569.

Galbraith, P.S. and D.E. Kelley. (1996). *Identifying overturns in CTD profiles.* J. Atmos. Oceanic Technol. 13: 688-702.

Gargett, A. E. (1997). *"Theories" and techniques for observing turbulence in the ocean euphotic zone. Lectures on Plankton and Turbulence.* C. Marrasé, E. Saiz and J.M. Redondo (eds.). Sci. Mar. 61 (Supl. 1): 25-45.

Gargett, A. E. (1989). *Ocean turbulence.* Ann. Rev. Fluid Mech. 21: 419-452.

Gargett, A. E.; Osborn, T. R.; Naysmyth, P. W. (1984). *Local isotropy and the decay of turbulence in a stratified fluid.* J. Fluid Mech. 144: 231-280.

Garrett, C. (1989). *A mixing length interpretation of fluctuations in passive scalar concentrations in homogenous turbulence.* J. Geophys.Res. 94: 9710-9712.

Gibson, C.H. (1968a). *Fine Structure of Scalar Fields Mixed by Turbulence: I. Zero-Gradient Points and Minimal Gradient Surfaces.* Phys. Fluids 11: 2305-2315.

Gibson, C.H. (1968b). *Fine Structure of Scalar Fields Mixed by Turbulence: II. Spectral Theory.* Phys. Fluids 11: 2316-2327.

Gibson, C.H. (1980). *Fossil temperature, salinity and vorticity in the Ocean.* In *Marine Turbulence* Nihoul, J.C.J. Ed., Elsevier. pp: 221-257.

Gibson, C.H. (1982). *On the scaling of vertical temperature gradient spectra.* J Geophys. Res. 87: 8031-8038.

Gibson, C.H. (1982). *Alternative interpretations for microstructure patches in the thermocline.* J. Phys. Oceanogr. 12: 374-383.

Gibson, C.H. (1987). *Fossil turbulence and intermittency in sampling oceanic mixing processes.* J. Geophys. Res., 92, 5383-5404.

Gibson, C.H. (1991). *Kolmogorov similarity hypotheses for escalar fields: sampling intermittent turbulent mixing in the ocean and galaxy.* Proc. Roy. Soc. Lon. A 434:149-164.

Gibson, C.H. (1996). *Turbulence in the ocean, atmosphere, galaxy, and universe.* Appl. Mech. Rev. (5) 49: 299-315.

Gibson, C.H. (1998). *Intermittency of internal wave shear and turbulence dissipation.* Phys. Proc. in Lakes and Oceans, Coastal and Estuarine Studies 54: 363-376.

Gibson, C.H. (1999). *Fossil turbulence revisited.* J. Mar. Sys. 21(1-4): 147-167.

Gibson, C. H.; Schwarz, W. H. (1963.). *The universal equilibrium spectra of turbulent velocity and scalar fields.* J. Fluid Mech. 16: 365-384.

Gloor, E. U. (1995). *Methode der temperaturmikrostruktur un deren anwendung auf bodengrenzschicht in geschichteten wasserkörpern.* PhD Dissertation. Eidgenössische Technische Hochschule, Zurich.

Grant,H.L.; Stewart,R.W.; Moilliet,A. (1962). *Turbulence spectra from a tidal channel.* J. Fluid. Mech. 12: 241-268.

Gregg, M.C. (1977a). *Variations in the Intensity of Small-Scale Mixing in the Main Thermocline.* J. Phys. Oceanogr. 7: 436-454.

Gregg, M.C. (1977b). *Variations in intensity of small-scale mixing in the main thermocline.* J. Phys. Oceanogr. 7: 436-454.

Gregg, M.C.; T.B. Meagher; A.M. Pederson; Aagaard, E. (1978). *Low Noise Temperature Microstructure Measurements with Thermistors.* Deep Sea Res. 25: 843-856.

Gregg, M.C. (1979). *The effects of bias error and system noise on parameters computed from C, T, P, and V profiles.* J. Phys. Oceanogr. 9: 199-217.

Gregg, M.C. (1980). *Zero crossings of temperature microstructure.* Marine turbulence, J.C.J. Nihoul Ed., Elsevier, pp: 135-142.

Gregg, M. C. (1987). *Diapycnal mixing in the thermocline: a review.* J. Geophys. Res. Vol 92: 5249-5286.

Gregg, M. C. (1991). *The study of mixing in the ocean: A brief history.* Oceanography. 4: 39-45.

Gregg, M. C.; Cox, C. S. (1971). *Measurements of the oceanic microstructure of temperature and electrical conductivity.* Deep Sea Res. 18: 925-934.

Gregg, M. C.; Hess, W. C. (1985). *Dynamic response calibration of Sea-Bird temperature and conductivity probes.* J. Atmos. Oceanic Technol. 2: 304-313.

Gregg, M. C.; D'Asaro, E. A.; Shay, T. J.; Larson, N. (1986). *Observations of persistent mixing and near-inertial internal waves.* J. Phys. Oceanogr. 16: 856-885.

Gregg, M. C.; Winkel, D. P.; Sanford, T. B. (1993). *Varieties of fully resolved spectra of vertical shear.* J. Phys. Oceanogr. 23: 124-141.

Haury, L.R.; Yamazaky, H.; E.C. Itsweire (1990). *Effects of turbulent shear flow on zooplankton distribution.* Deep sea Res. 37(3): 447-461.

Head, M. J. (1983). *The use of miniature four-electrode conductiviti probes for high-resolution measurements of turbulent density or temperature variations in salt-stratified flows.* PhD Dissertation. Universitat de Califòrnia. 221 p.

Horne, E. P. W.; Toole, J. M. (1980). *Sensor response mismatches and lag correction techniques for temperature-salinity profilers.* J. Phys. Oceanogr. Vol 16: 1997-2012.

Imberger, J. (1985). *The diurnal mixed layer.* Limnol. Oceanogr. 30: 737-770.

Imberger, J.; Boashash, B. (1986). *Application of the Wigner-Ville distribution to temperature gradient microstructure: A new technique to study small-scale variations.* J. Phys. Oceanogr. Vol 10: 1122-1130.

Imberger, J.; Ivey, G.N. (1991). *On the nature of turbulence in a stratified fluid. Part II: Application to Lakes.* J. Phys. Oceanogr. Vol 21: 659-680

Imboden, D.M. (1981). *Tracers and mixing in the aquatic environment.* Habilitation Thesis. Swis. Fed. Inst. Technology, Zurich, Switzerland, 137 p.

Imboden, D. M.; Wüest, A. (1995). *Mixing mechanisms in lakes.* In Physics and Chemistry of Lakes. ed. by A. Lerman, D. M. Imboden, and J. R. Gat, Springer, 83-138.

Ivey, G.N.; Nokes, R.I. (1989). *Vertical mixing due to the breaking of critical internal waves on sloping boundaries.* J. Fluid Mech. 204: 479-500.

Ivey, G.N.; Imberger, J. (1991). *On the nature of turbulence in a stratified fluid. Part I: The energetics of mixing.* J. Phys. Oceanogr. Vol 21: 650-658

ISW; SST (1999). *MSTB. Microstructure Data Evaluation Toolbox. Handbook.* Version 1.4: 51 pp.

Itsweire, E.C. (1984). *Measurements of vertical overturns in a stably stratified turbulent flow.* Phys. Fluids 27: 764-787

Itsweire, E.C.; Helland, K.N.; Van Atta C.W. (1986). *The evolution of grid-generated turbulence in a stably stratified fluid.* J. Fluid Mech. Vol 162: 299-338.

Itsweire, E.C., J.R. Kossef, D.A. Briggs, and J.H. Ferziger. (1993). *Turbulence in stratified shear flows: Implications for interpreting shear-induced mixing in the ocean.* J. Phys. Oceanogr. 23:1508-1522.

Jones, I. S. F. (1985). *Some statistics of the temperature profile through the base of the ocean mixed layer.* Deep-Sea Res. 32: 1255-1272.

Kitaigorodskii,S. A.; Donelan, M. A.; Lumley, J. L.; Terray, E. A. (1983). *Wave-turbulence interactions in the upper ocean. part II: Statistical characteristics of wave and turbulent components in the random velocity fields in the marine surface.* J. Phys. Oceanogr. 13:1988-1999.

Kundu, P. (1990). *Fluid Mechanincs.* Academic Press, Inc.

Lienhard, J.H. and C.W. Van Atta. 1990). *The decay of turbulence in thermally stratified flow.* J. Fluid Mech. 210:57-112.

Lombardo, C. P.; Gregg, M. C. (1989). *Similarity scaling of viscous and thermal dissipation in a convecting surface boundary layer.* J. Geophys. Res. 94: 6273-6284.

Luketina, D.A. (1986). *Frontogenesis of freshwater overflows.* PhD Dissertation. Centre of Water Research. Austràlia.

Luketina, D.A., Imberger, J. (1989). *Turbulence and entraintment in a buoyant surface plume.* J.Geophy. Res. 94:12619-12636.

Luketina, D.A., Imberger, J. (1999). *Determining kinetic energy dissipation from Batchelor curve fitting.* Enviat a J. Atmos. Ocean. Tech.

Kolmogorov, A.N. (1941). *The local structure of turbulence in an incompressible viscous fluid for very large Reynolds number.* C.R. Acad. Sci., USSR, 30 :853-860.

Mac Intyre, S. ; Alldredge A.L.; Gotschalk-C.C. (1995). *Accumulation of marine snow at density discontinuities in the water column.* Limnol. Oceanogr. 40 (3): 449-468.

Mallat, S. (1989) *A theory for multiresolution signal decomposition: the wavelet representation.* IEEE Pattern Anal. And Machine Intell. 11(7): 674-693.

Marrasé, C.; Saiz, E.; Redondo, J.M. (1997). *Lectures on Plankton and Turbulence.* Sci. Mar. 61 (Supl. 1).

Margalef, R. (1983). *Limnología*. Ediciones Omega, Barcelona. 1010 pp.

Massel, S.R. (1999). *Fluid mechanics for marine ecologists*. Heidelberg: Springer-Verlag. 566 pp.

Mellor, G.L.; Yamada,T. (1982). *Development of a Turbulence Closure Model for Geophysical Fluid Problems*. Rev. Geophys. Space Phys. 20: 851-875.

Misiti, M., Misiti, Y., Oppenheim, G.; J.M. Poggi (1996) *Matlab Wavelet Toolbox User's Guide*. The MathWorks, Inc., 626 pp.

Monin, A.S.; Yaglom, A.M. (1975). *Statistical hydrodynamics, Vols. 1 and 2*. MIT Press, Cambridge, Ma.

Moum, J.N. (1990). *Profiler measurements of vertical velocity fluctuations in the ocean*. J. Atmos. Oceanic. Technol. 7:323-333.

Moum, J.N. (1996). *Efficiency of mixing in the main thermocline*. J.Geophy. Res. 101:12057-12069.

Moum, J.N. (1996). *Energy-containing scales of turbulence in the ocean thermocline*. J. Geophys. Res. Vol 14: 95-109.

Moum, J.N.; Caldwell, D. R.; Paulson, C. A. (1989). *Mixing in the equatorial surface layer and thermocline*. J. Geophys. Res. 94: 2005-2022.

Moreno-Amich, R.; Garcia Berthou, E. (1989). *A new bathimetric map based on echosounding and morphometrical characterization of the Lake of Banyoles*. Hydrobiol. 185: 83-90.

Nason, G. P. (1994). *Wavelet Regression by Cross-Validation*. Technical Report 447.

Neumann, T.; Prandke, H. (1992). *Entwicklung eines Sensors zur Turbulenzmessung im Meer*. University Rostock, Proceedings of the 7. Symposium Maritime Elektronik, Arbeitskreis Messelektronik. pp: 81-84.

Oakey, N. (1982). *Determination of the rate of dissipation of turbulent energy from simultaneous temperature and velocity shear microstructure measurements*. J. Phys. Oceanogr. Vol 12: 256-271.

Oakey, N. S.; Elliott, J. A. (1982). *Dissipation within the surface mixed layer*. J. Phys. Oceanogr, 12: 171-185.

Oldham, C. (1993). *A portable microprofiler with fast response oxygen sensor.* Internal report ED-693-CO. Centre for Water Research. University of Western Australia.

Osborn, T. R. (1974). *Vertical profiling of velocity microstructure.* J. Phys. Oceanogr. 4: 109-115.

Osborn, T. R. (1980). *Estimates of the local rate of vertical diffusion from dissipation measurements.* J. Phys. Oceanogr. 10: 83-89.

Osborn, T. R.; Cox, C. S. (1972). *Oceanic fine structure.* Geophys. Fluid Dyn. 3: 321-345

Osborn, T. R.; Crawford,W. R. (1980). *Turbulent velocity measurements with an airfoil probe*, Instruments and methods of Air-Sea. Interaction, ed. L. Hasse, F. Dobson and R. Davis, Plenum Press.

Osborn, T. R.; Farmer, D. M.; Vagle, S; Thorpe, S. A.; Cure, M. (1992). *Measurements of bubble plumes and turbulence from a submarine.* Atmosphere-Ocean. 30: 419-440.

Otnes, R. K.; Enochson, L. (1972). *Digital time series analysis.* Wiley Press. 467 pp.

Ozmidov, R.V. (1965). *On the turbulent exchange in a stably stratified ocean.* Izv. Acad. Sci., USSR, Atmos. Oceanic Phys. Series 1:853-860.

Panofsky H.A.; Dutton J.A. (1984). *Atmospheric turbulence, models and method for engineering applications.* ed. John Wiley and Sons.

Pen, U.L. (1999). *Application of wavelets to filtering of noisy data.* Phil. Trans. R. Soc. Lond. A, 357, 2561-2571.

Peters, H.; Gregg, M.C.; Toole, J. M. (1988). *On the parameterization of equatorial turbulence.* J.Geophy. Res. 93:1199-1218.

Peters, H.; Gregg, M.C.; Sandford, T.B. (1994). *The diurnal cycle of the upper equatorial ocean: Turbulence, fine scale shear and mean shear.* J.Geophy. Res. 99:7707-7723.

Peters, H.; Gregg, M.C.; Sandford, T.B. (1995). *On the parameterization of equatorial turbulence: Effect of fine-scale variations below the range of the diurnal cicle.* J.Geophy. Res. 93:1199-1218.

PME. (2001). Precision Measurement Engineering. http://www.pme.com/

Pond, S.; Pickard, G. L. (1983). *Introductory dynamical oceanography.* $2^{nd}$ Edition. Pergamon Press. 329 p.

Prandke, H.; Stips, A. (1992): *A model of Baltic thermocline turbulence patches, deduced from experimental investigations.* Continental Shelf Research.12 (5-6): 643-659.

Prandke, H.; Stips, A. (1996). *Investigation of microstructure and turbulence in marine and limnic waters using the MST profiler.* Technical note n$^o$ I.96.87. Join Research Center of the European Commission. Space Applications Institute (Ispra-Italia).

Prandke, H.; Stips, A. (1998). *Test measurements with an operational microstructure-turbulence profiler: Detection limit of dissipation rates.* Aquat. Sci. 60:191-209.

Press,W.H.; Teukolsky, S.A.; Vetterling, W.T.; Flannery, B.P. (1994). *Numerical recipes in C. The art of scientific computing.* Cambridge University Press $2^{nd}$ Edition. 999 pag.

Quing, Z.; Stull, R.B. (1992). *Alternative nonlocal descriptions of boundary-layer evolution.* J. Atmos. Sci. 49: 2267 - 2281.

Reynolds, O. (1894). *On the dynamical theory of incompressible viscous fluids and the determination of the criterion.* Phil. Trans. Roy. Soc., London A186, 123.

Reynolds, C.S. (1989). *Physical determinants of seasonal change in the species composition of phytoplankton*, Phytoplankton Ecology: succession in plankton communities. ed. U.Sommer. pp 9-56. Springer Verlag, New York.

Rohr, J. J.; Itsweire, E. C.;. Helland, K. N; Van Atta, C. W. (1988). *Growth and decay of turbulence in a stably stratified shear flow.* J. Fluid Mech. 195: 77-111.

Ruddick, B.; Anis, A.; Thompson, K. (1999). *Maximum likelihood spectral fitting: the Batchelor spectrum.* (In press) J. Atmos. Ocean. Tech.

Saddoughi, S.G.; Veeravali,S.V. (1994). *Local isotropy in turbulent boundary layers at high Reynolds numbers.* J. Fluid. Mech. 268: 333-372.

Shannon, CE (1948). *A mathematical theory of communication.* Bell System Tech. J. 27: 379-423, 623-656.

Shay, T.J.; Gregg, M.C. (1986). *Convectively driven turbulent mixing in the upper ocean.* J. Phys. Oceanogr. 16:1777-1798.

Siedler, G.; Peters, H. (1989). *Properties of sea water: viscosity*, Ozeanographie (Vol. 3). ed. Landolt-Börnstein. Springer-Verlag, Berlin, pp: 258-260.

Simon, A. (1997). *Turbulent mixing in the surface boundary layer of lakes.* PhD Dissertation. Diss. ETH. 12272.

Skilling, J.; Gull, S. F. (1985). *Algorithms and applications*, Maximum-entropy and bayesian methods in inverse problems. ed. Smyth, C. R.; Grandy,W. T. Jr. D. Reidel Publishing Company. Boston. pp: 83-131.

Smyth, W.D.; P.O. Zavialov; Moum, J.N. (1997). *Decay of turbulence in the upper ocean following sudden isolation from surface forcing.* J. Phys. Oceanogr. 27: 164-176.

Smyth, W.D.; Moum, J. N. (2000). *Length scales of turbulence in stably stratified mixing layers.* Phys. Fluids. 12: 1327-1342.

Smyth, W.D.; Moum, J. N.; Caldwell, D.R. (2001). *The efficiency of mixing in turbulent patches: inferences from direct simulations and microstructure observations.* J. Phys. Oceanogr. 31: 1969-1992.

Sokal, R.R.; Rohlf,F.J. (1995). *Biometry: the principles and practise of statistics in biological research.* W.H. Freeman and Company $3^{rd}$ Edition. 887 pag.

Soloviev, A. V.; Vershinsky, N. V.; Bezverchnii, V. A. (1988). *Small-scale turbulence measurements in the thin surface layer of the ocean.* Deep-Sea Res. 35: 1859-1874.

Soloviev, A.V.; Lukas , R.; Hacker, P.; Schoeberlein, H.; Baker, M.; Arjannikov, A. (1999). *A near-surface microstructure sensor system used during TOGA COARE. Part II: Turbulence Measurements.* J. Atmos. and Oceanic Techn. 16: 1598-1618.

Sreenivasan, K. R. (1991). *Fractals and multifractals in fluid turbulence.* Annu. Rev. Fluid Mech. 23: 539–600.

Stansfield, K.; Garret, C.; Dewey, R. (2001). *The probability distribution of the Thorpe displacements within overturns in Juan de Fuca Strait.* (in press). J. Phys. Oceanogr.

Stewart, R. W.; Grant, H. L. (1962). *Determination of the rate of dissipation of turbulent energy near the sea surface in the presence of waves.* J. Geophys. Res. 67: 3177-3180.

Stillinger, D. C.; Helland, K. N.; Van Atta, C. W. (1983). *Experiments on the transition of homogeneous turbulence to internal waves in a stratified fluid.* J. Fluid Mech. 131: 91-122.

Stips, A.; Rasmussen, B.; Prandke, H. (1996). *Measurements of wind induced near surface turbulence in Lake Maggiore.* Internal report.

Stull, R. B (1984). *Transilient Turbulence Theory. Part I: The Concept of Eddy Mixing Across Finite Distances.* J. Atmos. Sci. 41: 3351-3367.

Stull, R. B (1985). Predictability and scales of motion. Bull. Amer. Met. Soc. 66: 432-436.

Stull, R. B (1988). *An Introduction to Boundary-Layer Meteorology.* Dordrecht, Kluwer Academic Publishers. 665 pp.

Stull, R. B (1991). *A Comparison of Parameterized vs. Measured Transilient Mixing Coefficients for a Convective Mixing Layer* Bound.-Layer Meteor. 55: 67-90.

Stull, R. B (1993). *Review of Nonlocal Mixing in Turbulent Atmospheres: Transilient Turbulence Theory* Bound.-Layer Meteor. 62: 21-96.

Stull, R. B. and Hasawaga, T. (1984) *Transilient Turbulence Theory. Part II: Turbulent Adjustment.* J.Atmos. Sci. 41, 3368-3379.

Stull, R. B.; Driedonks, A. G. M (1987). *Applications of the Transilient Turbulence Parameterization to Atmospheric Boundary-Layer Simulations*, Bound.-Layer Meteor. 40: 209-239.

Stull, R.B.; Kraus, E.B. (1987). *A transilient model of the upper ocean.* J. Geophys. Res. 92: 10745-10755.

Taylor, G. I. (1935). *Statistical Theory of Turbulence.* Proc. Roy. Soc. 151: 421

Terray, E.A.; Donelan, M.A.; Agrawal, Y.C.; Drennan, W.M.; Kahma, K.K.; Williams III, A.J.; Hwang, P.A.; Kitaigorodskii, S.A. (1996). *Estimates of kinetic energy dissipation under breaking waves.* J. Phys. Oceanogr. 26:792-807.

Tennekes, H.; Lumley, J.L. (1972). *A first Course in Turbulence.* MIT Press, 300 pp.

Thorpe, S.A. (1977). *Turbulence and mixing in a Scottish Loch.* Philos. Trans. R. Soc. London Ser. A, 286: 125-181.

Thorpe, S.A. (1992). *Bubbles clouds and the dynamics of upper ocean.* Q.J.R. Meteorol. Soc. 118: 1-22.

Thorpe, S. A. (1993). *Energy loss by breaking waves.* J. Phys. Oceanogr. 23: 2498-2502.

Thorpe, S.A.; Jiang, R. (1998). *Estimating internal waves and diapycnal mixing from conventional mooring data in a lake.* Limnol. Oceanogr. 43 (5): 963-945.

UNESCO (1981). *The practical salinity scale 1978, and the international equation of state 1980).* Tenth Report of the Joint Panel on Oceanographic Tables and Standards. UNESCO Technical paper in Marine Sciences. 36: 13-21.

Vollmer, M. K. (1991). *Sharpening and matching response signals for finescale sensors.* CWR Reference WP-630 MV. 73 pp.

Wesson, J. C.; Gregg, M. C. (1994). *Mixing at Camarinal Sill in the Strait of Gibraltar.* J. Geophys. Res. Vol 99 (C5): 9847-9878.

Wijesekera, H.W.; Dillon, T.M.; Padman, L. (1993). *Some statistical and dynamical properties of turbulence in the oceanic pycnocline.* J. Geophys. Res. Vol 98: 22.665-22.679.

Wijesekera, H.W. (1996). *Fractal dimension as an indicator for turbulent mixing in the thermocline.* J. Geophys. Res. Vol 101 (C7): 16.703-16.709.

Wijesekera, H.W.; Dillon,T. (1997). *Shannon entropy as an indicator of age for turbulent overturns in the oceanic thermocline.* J. Geophys. Res. Vol 102 (C2): 3279-3291.

Wilson, H.B.; Keeling, M.J.(2000) *Spatial scales and low-dimensional deterministic dynamics.*The geometry of ecological interactions. Dieckmann, U.; Law, R. and J.A.J. Metz, Eds. Cambridge University Press. 565 pp.

Wüest, A.; van Senden, D.C.; Imberger, J.; Piepke, G.; Gloor, M. (1996). *Comparison of diapycnal diffusivity measured by tracer and microstructure techniques.* Dyn. Atm. Ocean., 23:1-3.

Wüest, A., Piepke, G.; Halfman, J. D. (1996) *Combined effects of dissolved solids and temperature on the density stratification of Lake Malawi.* The Limnology, Climatology and Paleoclimatology of the East African Lakes, T.C. Johnson and E.O. Oada, Eds., Gordon and Breach Scientific Publishers. 183-202.

Wüest,A.; Piepke, G.; van Senden,D.C. (2000). *Turbulent kinetic energy balance as a tool for estimating vertical diffusivity in wind-forced stratified waters.* Limnol. Oceanogr. 45 (6): 1388-1400.

Wyngaard, J.C.; Cote, O.R. (1971). *The budget of turbulent kinetic energy and temperature variance in the atmosphere surface layer.* J. Atm. Sci. 28:190-210.

Yamazaki, H.; Lueck, R.; Osborn, T.R. (1990). *A comparasion of turbulence data from a submarine and vertical profiler.* J. Phys. Oceanogr. 20:1778-1786.

Yamazaki, H.; Osborn, T.R. (1990). *Dissipation estimates for stratified turbulence.* J. Geophys. Res. Vol 95 (C6): 9739-9744.

Wesson, J.; Saunders, K.D.; Bricker, B.; Perkins, H. (1998). A miniature fluorometer for oceanographic applications. J. Atmos. Ocean. Tech. 16: 1630-1634.